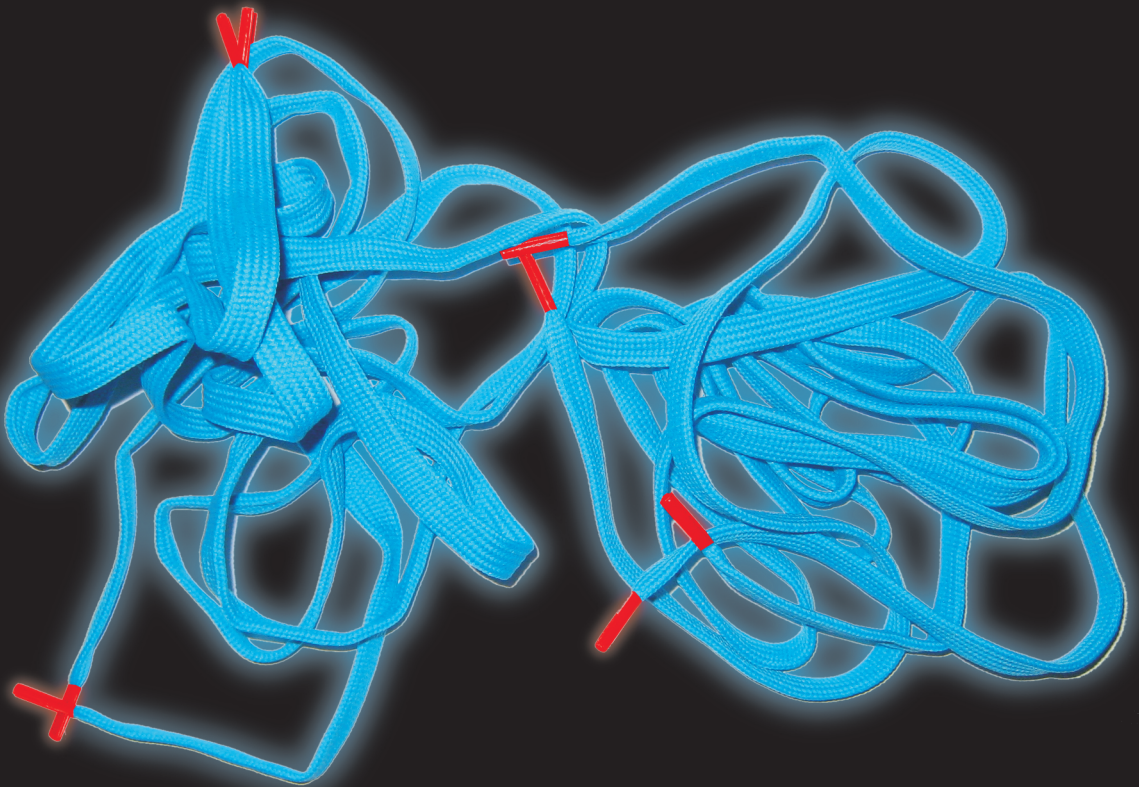


Nuclear Architecture: Image Processing and Analyses



Bart Vermolen

Propositions

belonging to the thesis

Nuclear Architecture: Image Processing and Analyses

Bart Vermolen
Februari 13, 2009

1. Results produced by computer programs, designed by humans, are subjective (chapter 1).
2. The cost for breaking Abbe's diffraction limit is always time (chapter2).
3. The 3D Gaussian profile is a good approximation of a deconvolved 3D image of a point source (chapter 3).
4. The use of an open internet source, like Wikipedia, is only justified when it is not used to strengthen an argument.
5. The fact that people are more fanatic when playing a game, like poker, for money instead of honor, shows that money is more important than honor.
6. Modern medicine is an extension of evolution.
7. The world is smaller when one is farther away.
8. To keep capitalism working, every 30 years a financial crisis, like the credit crisis, is needed.
9. When a proposition is not decisive, one should keep it to oneself.
10. Taking acting lessons improves giving lectures.

These propositions are considered opposable and defensible and as such have been approved by the supervisors, Prof. Dr. I.T. Young and Prof. Dr. Y. Garini.

Stellingen

behorende bij het proefschrift

Nuclear Architecture: Image Processing and Analyses

Bart Vermolen
13 februari 2009

1. Resultaten verkregen van computer programma's, door mensen ontworpen, zijn subjectief (hoofdstuk 1).
2. Het verbreken van Abbe's diffractie limiet gaat altijd ten koste van tijd (hoofdstuk 2).
3. Het 3D Gaussische profiel is een goede benadering van een gedeconvolveerd 3D beeld van een puntbron (hoofdstuk 3).
4. Alleen wanneer inhoud van een open internet bron, zoals Wikipedia, niet wordt gebruikt als argument om een stelling te bekrachtigen, is het gebruik hiervan gerechtvaardigd.
5. Het feit dat mensen fanatieker zijn in het spelen van een spelletje, zoals poker, wanneer om geld in plaats van eer wordt gespeeld laat zien dat geld belangrijker is dan eer.
6. De moderne geneeskunde is een extensie van de evolutie.
7. Hoe verder je weg bent, hoe kleiner de wereld wordt.
8. Een financiële crisis, zoals de kredietcrisis, is ongeveer elke 30 jaar nodig om het kapitalisme werkend te houden.
9. Wanneer een stelling niet resoluut is, moet men haar voor zich houden.
10. Het volgen van toneellessen verbetert het geven van college.

Deze stellingen worden opponeerbaar en verdedigbaar geacht en zijn als zodanig goedgekeurd door de promotoren, prof. dr. I.T. Young en prof. dr. Y. Garini.

Nuclear Architecture: Image Processing and Analyses

Proefschrift

ter verkrijging van de graad van doctor
aan de Technische Universiteit Delft,
op gezag van de Rector Magnificus prof. dr. ir. J.T. Fokkema,
voorzitter van het College voor Promoties,
in het openbaar te verdedigen op vrijdag 13 februari 2009 om 10.00 uur
door

Bartholomeus Johannes VERMOLEN

natuurkundig ingenieur
geboren te Rucphen

Dit proefschrift is goedgekeurd door de promotoren:

Prof. dr. I.T. Young

Prof. dr. Y. Garini

Samenstelling promotiecommissie:

Rector Magnificus,

Prof. dr. I.T. Young,

Prof. dr. Y. Garini,

Prof. dr. V. Subramaniam,

Prof. dr. J.H. de Winde,

Prof. dr. S. Mai,

Dr. R.W. Dirks,

Dr. J.-C. Olivo-Marin,

Prof. dr. ir. L.J. van Vliet,

voorzitter

Technische Universiteit Delft, promotor

Bar-Ilan University (Israël), promotor

Universiteit van Twente

Technische Universiteit Delft

University of Manitoba (Canada)

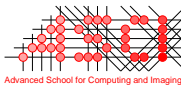
Leiden University Medical Center

Institut Pasteur (Frankrijk)

Technische Universiteit Delft, reservelid



This work was supported by the Cyttron Consortium.



This work was carried out in the ASCI graduate school.
ASCI dissertation series number 172.



<http://www.library.tudelft.nl/dissertations>

ISBN 978-90-8570-268-9

Copyright © 2009, B.J. Vermolen, The Netherlands.

All rights reserved.

Nothing shocks me. I'm a scientist.

— INDIANA JONES AND THE TEMPLE OF DOOM

Contents

Contents	v
List of abbreviations	ix
1 Introduction	1
1.1 Nuclear architecture	1
1.2 Nuclear organization and imaging	4
1.3 Scope	6
2 Fluorescence microscopy	9
2.1 Fluorescence	9
2.1.1 Labeling Techniques	10
2.2 Wide-field microscopy	12
2.3 Confocal microscopy	18
2.4 Microscopy beyond Abbe	21
2.5 Conclusions and discussion	25
3 Image restoration	27
3.1 The inverse problem	27
3.2 Tikhonov-Miller (TM) restoration	28
3.3 3D Restoration with multiple images acquired by a modified conventional microscope	30
3.3.1 Abstract	30
3.3.2 Introduction	30
3.3.3 Materials and methods	31
3.3.4 Results	40
3.3.5 Discussion	48
3.4 Gaussian approximation of deconvolved images acquired by a wide-field microscope	49
3.4.1 Introduction	49

3.4.2	Methods	49
3.4.3	Results	50
3.4.4	Conclusions	51
3.5	Conclusions and discussion	51
4	Three-dimensional organization of telomeres	53
4.1	Introduction	53
4.1.1	Cell Preparation	53
4.1.2	3D Image Acquisition	54
4.1.3	3D Image Processing	54
4.2	Segmentation of telomere signals	55
4.2.1	TopHat segmentation	55
4.2.2	Scale Space segmentation	57
4.2.3	Contrast enhancement of the TopHat and Scale Space method	59
4.3	Characterization of the structure	63
4.4	Correction of ρ_T by model fitting	65
4.5	TeloView	67
4.6	Organization during the cell cycle in mouse lymphocytes	67
4.7	Conclusions and discussion	69
5	Telomere and chromosome remodeling in the interphase nu- cleus	71
5.1	Introduction	71
5.2	Telomere length assessment and aggregates	72
5.2.1	Introduction	72
5.2.2	Methods	73
5.3	Chromosome overlap	79
5.3.1	Introduction	79
5.3.2	Methods	80
5.3.3	Results	83
5.3.4	Conclusions and discussion	83
5.4	Conclusions and discussion	84
6	Analysis of the three-dimensional redistribution of nuclear components in human mesenchymal stem cells	85
6.1	Introduction	86
6.2	Materials and Methods	88
6.2.1	Segmentation	88
6.2.2	Probe distribution	88
6.2.3	Cell preparation and molecular labeling	90
6.2.4	Image acquisition and processing	90
6.2.5	Statistics	91

6.3	Results	92
6.3.1	Probe segmentation	92
6.3.2	Nuclear segmentation	92
6.3.3	Changes in spatial distribution during activation of apoptosis	95
6.4	Discussion	98
6.5	Acknowledgments	99
	Conclusions and summary	101
	Conclusies en samenvatting	103
	References	105
	List of publications	119
	Journal publications	119
	Conference proceedings	121
	Patents	121
	Curriculum Vitae	123
	Acknowledgments	125

List of abbreviations

2D	Two-dimensional
3D	Three-dimensional
ADU	Analog-to-digital unit
BrdU	Bromodeoxyuridine
CC	Chromatin components
CCD	Charged-coupled-device
CDF	Cumulative distribution plot
CT	Chromosomal territory
DNA	Deoxyribonucleic acid
FISH	Fluorescence <i>in situ</i> hybridization
FWHM	Full width at half maximum
GCV	Generalized cross validation
GFP	Green fluorescent protein
hMSC	Human mesenchymal stem cells
LSCM	Laser scanning confocal microscope
MAPPG	Maximum a-posteriori restoration algorithm with Poisson noise and Gaussian priors
MAPPG2	MAPPG with two images
MSE	Mean squared error
NA	Numerical aperture
OTF	Optical transfer function
PML-NB	Promyelocytic leukemia nuclear body
PSF	Point spread function
RNA	Ribonucleic acid
ROI	Region of interest
RSE	Relative squared error
SE	Structural element
SNR	Signal-to-noise ratio
ssDNA	Single stranded DNA
TM filter	Tikhonov-Miller filter
TPE	Telomere position effect

Introduction

*"People who look for the first time through a microscope say **now I see this and then I see that** and even a skilled observer can be fooled. On these observations I have spent more time than many will believe, but I have done them with joy."*

— ANTONI VAN LEEUWENHOEK, 1701

Biology, microscopy and image processing go hand-in-hand starting from the 17th century. In 1665 Robert Hooke published the book *Micrographia*. In this book he is the first to have named the *cell*, after looking at plant cells and, what he found, a striking resemblance to the cells of a monk. It is believed that this book inspired Antoni van Leeuwenhoek to design a microscope of his own. While Hooke's compound microscope could magnify up to 30x, it is said that Van Leeuwenhoek's single lens microscope could magnify up to 500x. In figure 1.1 we see a drawing of both microscopes. Here we also see that to report findings done with the microscope, there was only one option: to draw it yourself. The human eye acts as the camera, the mind acts as the image processor and the drawing hand as the screen or printer.

Although Van Leeuwenhoek was regarded as an 'amateur', he is now known as the father of microbiology.

1.1 Nuclear architecture

In 1970 Francis Crick repostulated his central dogma theory (originally postulated in 1958) in molecular biology stating "The central dogma of molecular biology deals with the detailed residue-by-residue transfer of sequential information. It states that such information cannot be transferred back from protein to either protein or nucleic acid (Crick, 1970)." In other words, gene expression

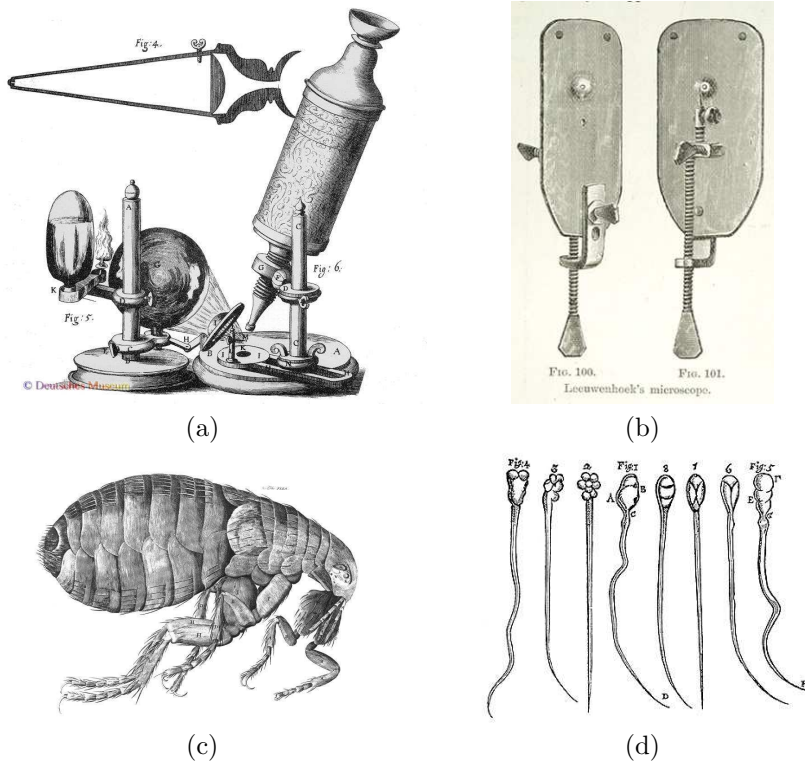


Figure 1.1: (a) Hooke's compound microscope. (b) Van Leeuwenhoek's single lens microscope. (c) Hooke's Drawing of a flea. (d) Van Leeuwenhoek's drawing of sperm cells.

is regulated by the information encoded in the linear sequence of nucleotides in deoxyribonucleic acid (DNA) as seen in figure 1.2. This central dogma has been undermined for quite some time. It is now known that gene expression is regulated by a far more complex system. One of the factors that has become to be known to play a major role is chromatin structure. In 1885, Carl Rabl was one of the first to hypothesize that the organization of chromosomes in the interphase cell is not random (Rabl, 1885). This has been confirmed by many studies in the last two decades. A nice overview about the architecture of the nucleus can be found in several reviews (Parada and Misteli, 2002; Misteli, 2007; Kumaran et al., 2008; Dekker, 2008; Cremer et al., 2004; Cremer and Cremer, 2001).

The transcription of DNA is one of the most important functions of the

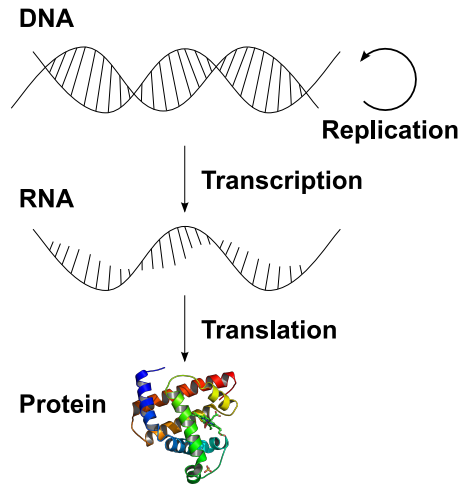


Figure 1.2: Central Dogma of molecular biology. In the top we see the DNA in its double stranded (double helix) form. DNA can replicate or be transcribed into ribonucleic acid (RNA) (middle, single stranded). RNA can be translated into proteins (bottom).

nucleus. To understand why the structure of nuclear components, like chromosomes, and sub-chromosomal components, like telomeres, might be important, one first has to recognize that gene regulation is a structural process. Gene regulating factors have to be at a certain position at a certain time. This process is likely to be more efficient when the nucleus is ordered and stays ordered throughout its lifetime. Evidence for this ordering has been shown; functions like transcription, replication and repair of the DNA are compartmentalized within the nucleus (Misteli, 2005). Also, chromosomes themselves are compartmentalized in what is known as Chromosomal Territories (CT) (Cremer and Cremer, 2001; Meaburn and Misteli, 2007). Every chromosome has a distinct space in the nucleus which is well separated from each other. This means that there is no intermingling of the different chromosomes.

The relationship between structure and function is still unknown. Two possible models are given by Misteli (2007). First the deterministic model where structure is the cause for function. In other words the compartments are there, independent of the ongoing function. This model is based on the assumption that the lamin network, short actin filaments or nuclear bodies may act as scaffolds and disruption of these scaffolds may disrupt function. The other model is based on self-organization. Here the structure is dictated by the ongoing functions in the nucleus. Evidence for this models includes the

fact that when some new functional sites appear, a new structural element also appears.

In 2002 cancer was responsible for 25% of deaths in developed countries (Jemal et al., 2005). It is a class of diseases where cells show uncontrolled growth resulting in a tumor. For most types of cancers the exact pathogenesis is still unknown, but it is known that cancer is a chromosomal disease (Duesberg et al., 2005). In all types of cancer there is abnormality of the karyotype, mostly showing aneuploidy, a deviation in normal ploidy (the number of copies of chromosomes which is two (diploid) in normal cells), and a number of other chromosomal aberrations (like mutations, translocations, breakage-fusion-bridges, etc.). One of the unanswered questions is what causes these aberrations.

1.2 Nuclear organization and imaging

Three elements in the nucleus have been studied in this thesis, telomeres, centromeres and lamin. Telomeres are the repetitive sequences of DNA at the ends of the chromosomes. In mouse and humans the repeating sequence consists of TTAGGG. The main function of telomeres is to solve the DNA end replication problem. When DNA replicates in the cell a small part at the end is unable to replicate and this part is lost. The telomere acts as a buffer, since losing a part of the telomere prevents the DNA from any information loss. Another important feature of telomeres is that they prevent 'sticky' ends of DNA from fusing together. It is therefore believed that telomeres play an important role in chromosome stability. A comprehensive review about this subject can be found in (Mai and Garini, 2006). Centromeres are also satellite repeats and serve as anchor points for the mitotic spindle to attach during cell division. They also have a role in transcriptional silencing. The third element is the lamins. These proteins form the nuclear membrane, but are also present inside the nucleus. They have also been associated with transcription and replication sites. It is believed there might be some tethering function of the lamins of chromatin to the periphery of the nucleus and also tethering particular chromatin regions in the nucleus. Hutchinson-Gilford progeria syndrome is a disease showing extreme aging with children leading to death at about 13 years. This disease is an effect of a point mutation in the gene Lamin A (LMNA) coding for the proteins lamin A and lamin C. A review of the possible structural versus functional mechanisms of telomeres, centromeres and lamins can be found in (Parada et al., 2004).

In situ and *in vivo* three-dimensional (3D) microscopy studies have become increasingly popular over the recent years. Although *in vitro* studies can give a lot of information or even answer specific questions, 'seeing is believing' is appreciated even more. The last three decades, fluorescent microscopy

methods have become more and more mature. The combination of newer and better hardware (microscopes, cameras, computers) and wetware (new fluorescent dyes and proteins) is able to produce an enormous amount of data that needs to be processed and analyzed. Van Leeuwenhoek already introduced the first problem, people who process the images are subjective (see the quote at the beginning of this section). Another problem is the amount of data. Tens, hundreds, thousands or even more images need to be analyzed (this is of course dependent on the question asked and the statistics related to the specific problem). The third problem is that the 3D images are eventually looked at by the eye, which is, inherently, a two-dimensional (2D) imaging system. This makes it extremely hard for humans to analyze 3D data. To solve these issues also software (image processing and analysis) has significantly evolved. Faster computers in combination with smarter algorithms can solve these problems. The first problem of objectiveness is partially solved, the analyses done will be the same every time the algorithm is used. The algorithm, however, is designed by a human and will therefore be subjective. This reasoning shows that the development of applied image processing algorithms is highly dependent on the research question asked and the person who develops them.

A popular method to study chromosomal arrangements in the nucleus is by radial distribution analysis. Here the amount of stained DNA is measured against the relative radius of the nucleus. To characterize the chromatin distribution in nuclei [Young et al. \(1986\)](#) developed several measures, one of them being the radial distribution of the chromatin. In [\(Mayer et al., 2005\)](#) several mouse cell types were studied and showed non-random correlations in radial CT position. [Bolzer et al. \(2005\)](#) use a combinatorial labeling for all chromosomes so they can be imaged simultaneously giving a complete map of all CTs in human fibroblast nuclei. Again a non-random correlation of radial positions was found. In the same study, correlations between CT size, gene-density and radial position were shown. In [\(Gerlich et al., 2003\)](#) photobleaching experiments were done where bleached parts in the nucleus remained constant after cell division. CT and gene-density radial distributions of higher primates have also been studied and compared to humans showing evolutionary conservation [\(Tanabe et al., 2002\)](#). The gene-density distributions have been modeled in [\(Kreth et al., 2004\)](#), where the measurements correlate better to the model when the gene position is dependent on gene density and CT sequence length.

A different class is detection and analysis of dot-like structures in the nucleus. Here we can think of labeling specific genes, telomeres or centromeres. In [\(Netten et al., 1997\)](#) chromosome specific sites were labeled to perform dot counting and study aneuploidy. Here, in 2D images of interphase nucleus, dots were segmented after which they were counted. A model-based approach to segmentation was used in [\(Thomann et al., 2002\)](#) after which the dots were tracked in time. Chromatin components (CC), like telomeres and centromeres,

have been studied to get either information indirectly about the chromosome position as done by (Bin Sun et al., 2000) or to get information about the CCs themselves. In (Nagele et al., 2001) it is suggested that telomeres play a role in interphase chromosome topology. Telomeres are manually segmented and positions and intensity are measured. The relationship between function and nuclear organization of telomeres has been studied extensively in baker's yeast (*Saccharomyces cerevisiae*). Telomeres in yeast are normally clustered into three to seven foci and reside near the nuclear envelope. When transcription sites are near the nuclear envelope, especially near non-pore sites, they can become inhibited, this effect is increased in the presence of telomeres (Akhtar and Gasser, 2007; Tham and Zakian, 2002; Feuerbach et al., 2002; Galy et al., 2000). This latter effect is known as the Telomere Position Effect (TPE). In (Therizols et al., 2006) it is suggested that also the repair of DNA double-strand breaks in subtelomeric regions is dependent on telomeres tethering to the nuclear envelope. In (Taddei and Gasser, 2006) the mechanism of double-strand break repair is described more. Metazoan cell nuclei are more than 10-fold larger than yeast cells. This gives a smaller surface-volume ratio which might be problematic for tethering all the silenced chromatin (Sexton et al., 2007). Ku, a telomere binding protein complex involved in telomere maintenance (Fisher et al., 2004) and tethering to the nuclear envelope, and other telomere binding factors have been reviewed by Fisher and Zakian (2005) and Tham and Zakian (2000).

1.3 Scope

The primary goal of this thesis is the development of image processing and analyses methods to study the organization of nuclear elements, based on 3D fluorescence microscopy images. As described in the previous section, many methods and algorithms already exist. This thesis will follow some existing methods and show newly developed methods specific to research questions from molecular biology. The basic structure of the thesis is found in figure 1.3.

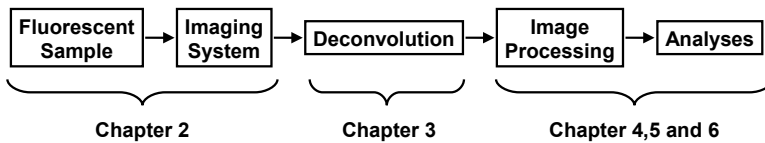


Figure 1.3: Basic overview of the thesis.

In chapter 2 the tools of the trade are described. Specific DNA sequences

of interest need to be labeled before they can be imaged. Here we describe two methods: Fluorescence *in situ* Hybridization (FISH) and fused proteins. Furthermore the principles of wide-field microscopy and confocal microscopy are discussed. Although this is not in the scope of this thesis, new, ground-breaking methods in microscopy are reviewed. To acquire 3D images several methods exist. Confocal microscopy is a hardware solution. Another method is to acquire an image stack of 2D wide-field images at sequential focus depths. This requires a post-acquisition processing step called deconvolution, which is explained in chapter 3. The principle of the "poor-mans" confocal microscope is explained together with a deconvolution method developed for this microscope. It is well known that 2D images of small spots (smaller than the diffraction limit, so-called point sources) can be approximated by a 2D Gaussian profile (Zhang et al., 2007). The ability to approximate deconvolved 3D images of point-sources by a 3D Gaussian profile has been studied in chapter 3.

Chapter 4 deals with the segmentation and localization of these small spots. A newly developed segmentation algorithm will be used to characterize the spatial organization of telomeres in normal mouse lymphocytes during the cell cycle. No algorithms were available to measure and analyze the relative size of telomeres from 3D fluorescent microscopy images. Therefore a new algorithm was developed in chapter 5. Analysis from the measurements from this method includes a method to statistically determine aggregating telomeres. Together with a method to measure the overlap of chromosomes in the interphase nucleus, these new methods can be used to analyze and understand remodeling of the cell nucleus after induction of external factors like activation of the c-Myc gene (chapter 5), which is associated with 70% of all cancers (Nesbit et al., 1999). The techniques developed in chapter 4 were also used to study the radial redistribution of nuclear components like telomeres, centromeres and Promyelocytic Leukemia (PML) nuclear bodies (chapter 6).

Fluorescence microscopy

Although father and son Janssen from Middelburg, the Netherlands, had already constructed a compound microscope in the 16th century and the first fluorescent microscopes were developed in the beginning of the 20th century, fluorescence microscopy really became more useful when Ploem invented the filter cube in 1967 (Ploem, 1967) and, with it, epifluorescence microscopy. This breakthrough was followed by the development of Minsky's confocal microscope in 1979 by Brakenhoff (Minsky, 1961; Brakenhoff, 1979; Brakenhoff et al., 1979), which made it possible to perform true optical sectioning.

In section 2.1 we will discuss the basics of fluorescence and touch upon some labeling techniques to visualize the DNA. Section 2.2 will discuss wide-field microscopy, the point spread function (PSF), optical transfer function (OTF) and the microscope's image formation. The same subjects will be handled in 2.3 for confocal microscopy. In section 2.4 some microscopy methods will be presented where the diffraction limit is broken.

2.1 Fluorescence

In 1852 Sir George G. Stokes first observed and described fluorescence. He noticed that, when illuminating a mineral called fluorspar (also known as fluorite) with ultra violet light, the mineral radiates blue light. This change in color is what we now call the Stokes shift. The phenomenon of fluorescence can be described by a Jablonski energy diagram, see figure 2.1. In such a diagram we can see the different possible energy levels of an electron in a molecule. When a photon interacts with this electron there is a chance that the electron will absorb the photon's energy, and be excited into a higher energy state, i.e. any vibrational state of the singlet state. After some vibrational relaxation the electron can drop back into a vibrational state of the ground state and radiate a photon. It is evident that the emission photon will at least have the same wavelength as the excitation photon, but is likely to be longer. Herein lies the origin of the Stokes shift. The function describing the relative chance of a photon being absorbed as a function of wavelength is called the excitation

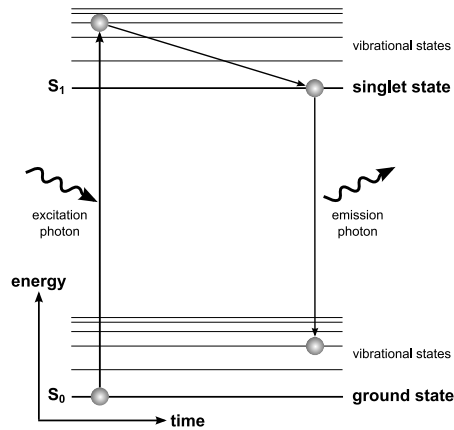


Figure 2.1: Jablonski energy diagram. An incoming photon can excite an electron into a higher energy state. After some relaxation (time scale in the order of picoseconds) to the singlet state (a meta-stable state where the electron can live in the order of nanoseconds) the electron will fall back into its ground state, emitting a photon with a wavelength which will be longer than the wavelength of the original photon.

spectrum. Such a function can also be made for the radiated photon, which is called the emission spectrum. In figure 2.2 the excitation and emission spectra for Texas Red are shown. The Stokes shift is defined here as the difference in wavelength between the maximum of the emission spectrum and the maximum of the excitation spectrum and is about 20 nm in this example. In fluorescence microscopy this shift is used to our advantage. With the use of filters the excitation light can be separated from the emission light as described in section 2.2.

2.1.1 Labeling Techniques

To detect specific DNA sequences we must use labels that are targeted to those sequences. A wide range of methods is available. Here we will discuss two methods: FISH and fused proteins. When several nuclei are present in the field of view of the microscope we also need a method to distinguish the individual nuclei. This is done by a counterstain, i.e. we stain all of the DNA. A well known method is by using DAPI. This is an intercalating fluorescent molecule that binds to A/T-rich sequences in the minor grooves of the DNA.

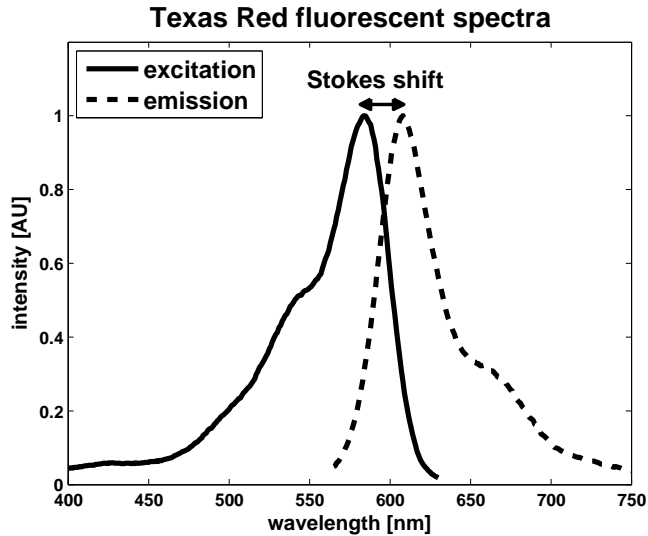


Figure 2.2: Excitation and emission spectra of Texas Red. We can also see the Stokes shift for this fluorescent dye¹.

Fluorescence in situ Hybridization (FISH)

FISH is a technique to label specific parts of the DNA (Rudkin and Stollar, 1977). In figure 2.3 we see the principle of FISH. Since the specific DNA sequence of interest is not visible as such, it needs to be labeled. This is done by use of the fact that single stranded (ss)DNA will anneal to a complementary sequence of ssDNA. The success of FISH lies in the fact that the ssDNA has a higher chance of annealing to added sequences of ssDNA with a fluorescent label attached to it than to its original complementary part.

Fluorescent proteins

In contrast to FISH one can also follow proteins that are co-localized with the DNA of interest, e.g. trf1 (telomere repeat binding factor 1) which is one of the proteins in the nucleoprotein complex surrounding the telomere. To visualize the protein of interest, the DNA of the cell is genetically altered, see figure 2.4. Before the stop codon of the DNA that translates to the protein, extra DNA

¹Texas Red Spectrum, Invitrogen/Molecular Probes, Carlsbad, California, USA, data at <<http://www.invitrogen.com/site/us/en/home/support/Product-Technical-Resources/Product-Spectra.1395lip.reg.us.html>>

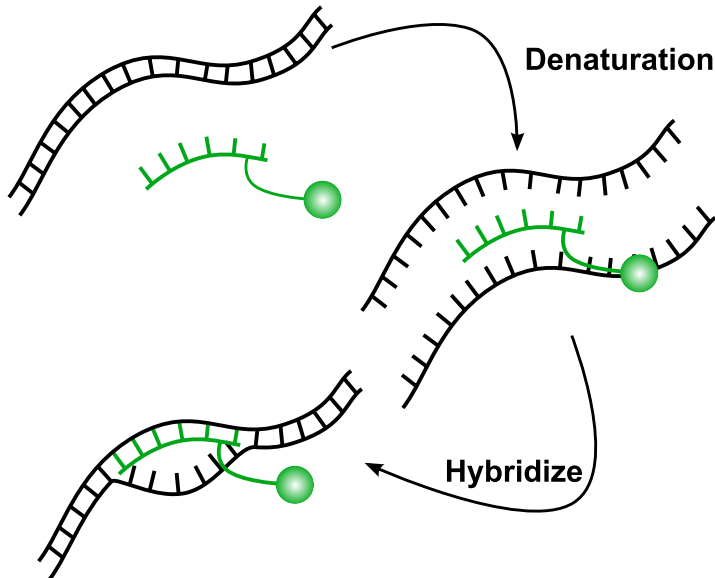


Figure 2.3: The principle of Fluorescence *in situ* Hybridization. Here we see the DNA sequence of interest (black). After denaturation of the DNA (by heating), probes, consisting of a sequence of complementary DNA, and a label (green), are added. If enough probes are added the chance is high that a probe will anneal instead of the original DNA. The label can consist of a fluorescent molecule (direct labeling) or a hapten molecule after which another step is needed to add a conjugate of a fluorescent molecule and a molecule that has a high affinity to the hapten molecule (indirect labeling), e.g. biotin-streptavidin.

is inserted. This DNA codes for a fluorescent protein. Now every time the protein of interest is expressed it will be conjugated to the fluorescent protein. Although green fluorescent protein (GFP) was the first protein to be used, a wide range of fluorescent proteins are now available (Shaner *et al.*, 2005).

2.2 Wide-field microscopy

In figure 2.5 we see a sketch of an epi-fluorescence wide-field microscope. The main light source is usually a mercury or xenon arc lamp, depending on the application. The mercury lamp emits only some lines in the spectrum, but at high brightness levels. The xenon lamp has a much flatter spectrum, but is less bright. The main components of this microscope are the filter cube and the objective. The filter cube is the component in the microscope which needs to be matched to the excitation and emission spectra of the fluorescent molecules.

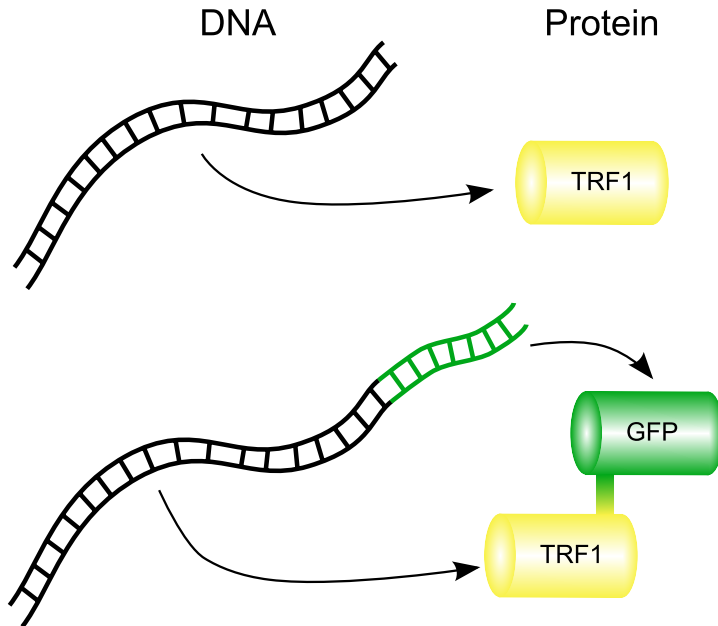


Figure 2.4: Fused Proteins. In the top row we see the DNA that codes for TRF1. To visualize this protein, DNA of GFP is inserted. Now a conjugated (or fused) protein will be expressed (bottom row). Because TRF1 is a protein associated with the telomeres, fluorescent signals from the GFP are likely to be colocalized with the telomeres.

In figure 2.6 we see an example of the spectra of the filters and the dichroic mirror.

The objective lens is the defining part of the microscope. It defines the point spread function (PSF), which in turn defines the resolution of the system. The PSF is the impulse response of the lens, in other words it is the image of a mathematical point. The PSF is formed because the lens is diffraction limited. This means that not all the diffracted light will pass through the lens, so the higher order interference that is needed to form a point in the image will not reach the image plane. This results in a three-dimensional interference pattern. This interference pattern is the PSF. Now, because the object can be seen as an infinite number of points and the superposition principle holds, the image of an object is the object convolved with the PSF of the imaging lens. Since the PSF has the properties of a distribution function (it is positive and the sum is finite) it acts as a blurring function: the image is a blurred version of the object. It should be noted that this is only valid for a PSF which is spatially invariant. In practice this is never the case. For example the object

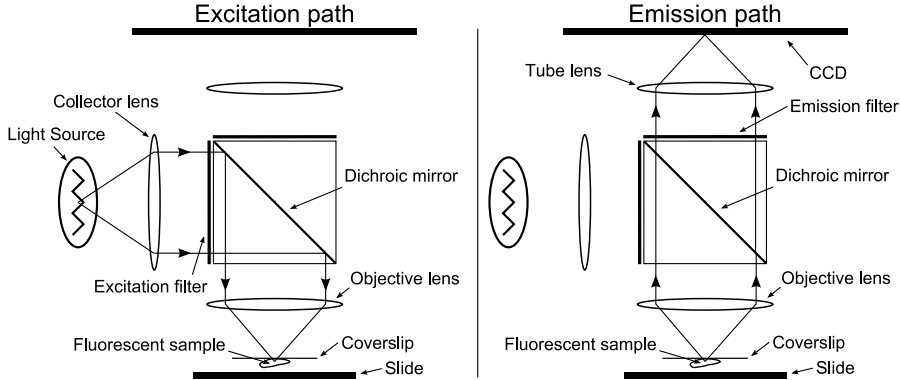


Figure 2.5: Wide-field microscopy sketch. On the left we see the excitation path of the light. After the light passes the filter cube, it hits the sample. Fluorescent molecules in the sample with an excitation spectrum which matches the excitation filter and dichroic mirror reflectance spectra can be excited. On the right we see the emission path of the microscope. The excited molecules can emit photons which, if matching the emission filter and dichroic mirror transmittance spectra, can reach the charged-coupled-device (CCD) camera.

itself will influence the PSF, which could result in a different PSF in every focal plane of the object. In figure 2.7 we see an example of a PSF. This PSF is a simulation according to the model derived by Gibson and Lanni (1991). We used a wavelength, $\lambda = 600$ nm, magnification, $M = 63x$, numerical aperture, $NA = 1.3$, and an isotropic sampling distance of, $dr = dz = 40$ nm.

Lord Rayleigh (born John William Strutt) saw that the blurring because of the PSF, which is an intrinsic property of the microscope system, results in a limited spatial resolution. He therefore defined the resolution of an imaging system as the distance between two point sources which can still be resolved by the human eye (Strutt, 1879, 1880). To make it less arbitrary, he defined it by the distance from the middle of the PSF to the first zero crossing, so the maximum of the PSF from the second point source is on top of the first zero crossing of the first point source. In figure 2.8 we see an example. This distance, δ_R , given by the Rayleigh criterion is:

$$\delta_R = 0.61 \frac{\lambda}{NA} \quad (2.1)$$

Note that this is close to the Abbe diffraction limit (Abbe, 1873):

$$\delta_A = \frac{\lambda}{2NA} \quad (2.2)$$

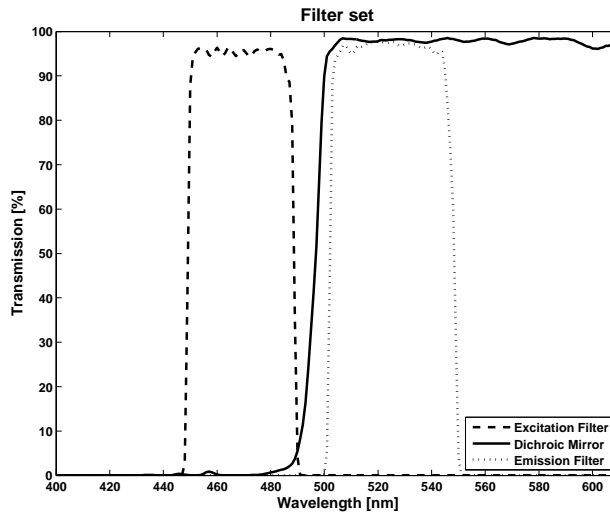


Figure 2.6: Transmission spectra of an excitation filter, dichroic mirror and emission filter. In the ideal case for the dichroic mirror this means that in the spectral region where the mirror is not transmitting it is reflecting. This filter can be used for a molecule which absorbs blue and excites green light, for example FITC, Cy2 or GFP.¹

In our example of figure 2.7 this results in $\delta_R = 282$ nm and $\delta_A = 231$ nm.

Karl Ernst Abbe discovered this fundamental limit of resolving power of a lens when he was hired by Carl Zeiss by the end of the 19th century to optimize the manufacturing process of lenses. He saw that to image an object, at least the first order of diffraction has to pass the lens. Since light passing an object with structures with higher spatial frequencies will diffract in a higher angle, there must be a highest frequency that can be imaged, giving the diffraction limit. More information can be obtained when we take the Fourier transform of the PSF. This will give us the so-called optical transfer function (OTF). It tells us which spatial frequencies are passed through the objective. We immediately see that the OTF has cut-off frequencies in the lateral direction, $f_{r,c}$, and in the axial direction, $f_{z,c}$. These cut-off frequencies are given by (Wilson and

¹Chroma Technology Corp, Rockingham, Vermont, USA, Excitation filter data: ET470/40x <http://www.chroma.com/index.php?option=com_products&Itemid=53&task=details&productType=part&id=938>, Emission filter data: ET525/50m <http://www.chroma.com/index.php?option=com_products&Itemid=53&task=details&productType=part&id=852> Dichroic mirror data: T495LP <http://www.chroma.com/index.php?option=com_products&Itemid=53&task=details&productType=part&id=851>

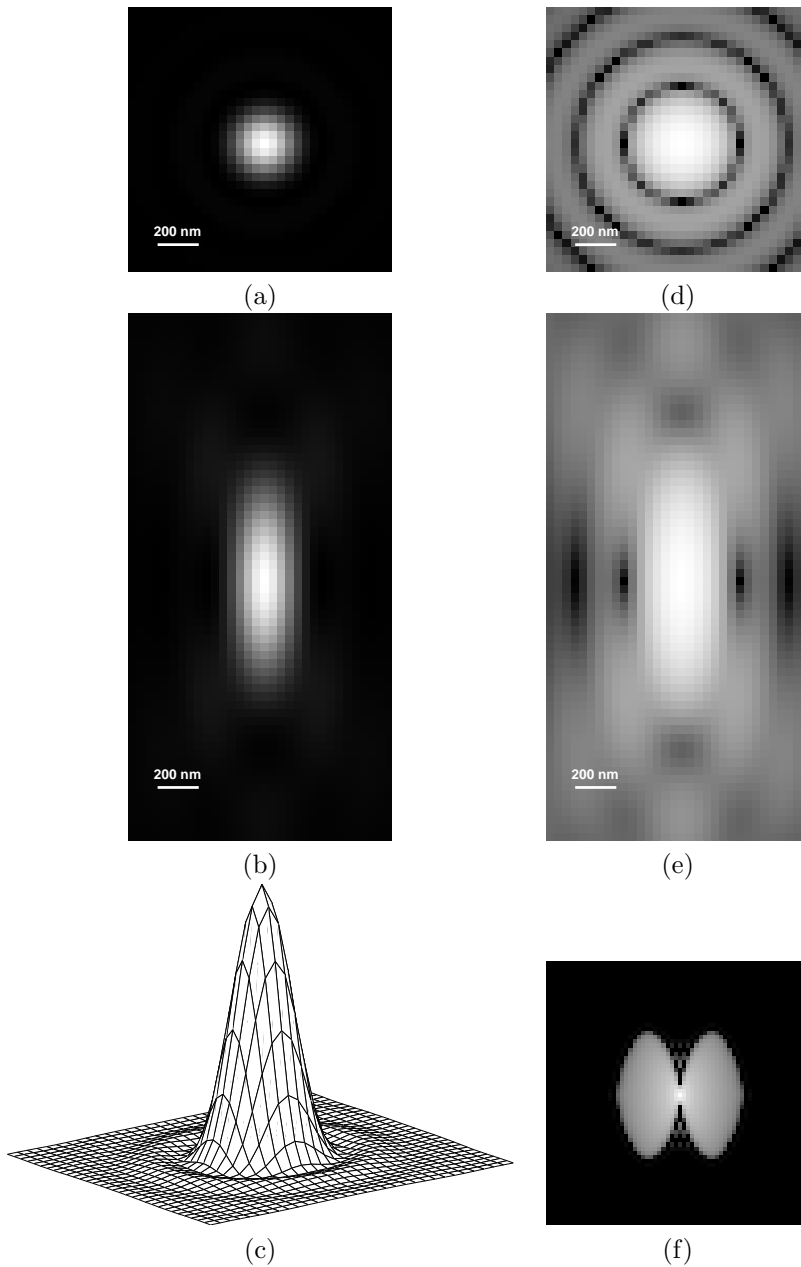


Figure 2.7: (a) shows a middle lateral (xy) section of a simulated wide-field PSF. (b) shows the middle axial (xz) section of the PSF. (c) shows a mesh representation of (a). In (d) and (e) we see the same as in (a) and (b) respectively where the intensities have undergone a logarithmic stretch. (f) shows a simulated OTF of the wide-field microscope.

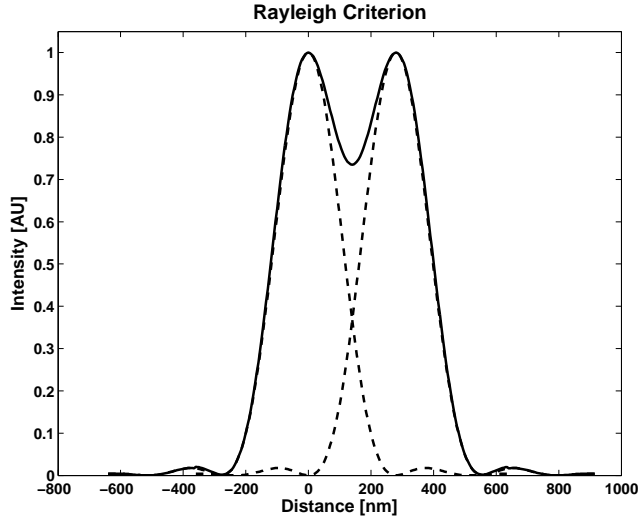


Figure 2.8: The dashed lines show the single point spread functions of two single point sources. The black line is the image of the two sources (superposition). The contrast (the relative difference between the maxima and the minimum in between) is approximately 26.5%.

(Tan, 1993):

$$f_{r,c} = \frac{2NA}{\lambda} \quad (2.3)$$

$$f_{z,c} = \frac{n - \sqrt{n^2 - NA^2}}{\lambda} \quad (2.4)$$

where n is the refractive index of the immersion medium. This information is useful because these frequencies also define the Nyquist frequencies, ($f_N = f_c/2$) and therefore the Nyquist sampling distance, $d = 1/f_N$. In our example this results in a sampling rate in the lateral direction of $d_r \leq 115$ nm and in the axial direction of $d_z \leq 407$ nm. Note that the cut-off frequency in the lateral direction is the reciprocal of the Abbe diffraction limit.

The OTF also shows why a simple wide-field setup cannot give true optical sectioning, i.e. 3D imaging. In the middle of the OTF we see the so-called "missing cone", see also figure 2.12. Low frequencies in the lateral direction in the object are not imaged outside of the focus plane. In practice this means that, when imaging in the focus plane, we also image objects that are far out of the focus plane and therefore blurred. In the next section we will describe confocal microscopy, which solves the problem of the "missing cone".

2.3 Confocal microscopy

The confocal microscope, also known as the laser scanning confocal microscope (LSCM), owes its name to the fact that it has pinholes in the *conjugate focal planes* as seen in figure 2.9. The object is illuminated by a single spot which of course is defined by the PSF. Note that this PSF is excitation wavelength dependent and therefore different from the emission PSF from wide-field microscopy. In figure 2.10 we see the principal of the confocal microscope.

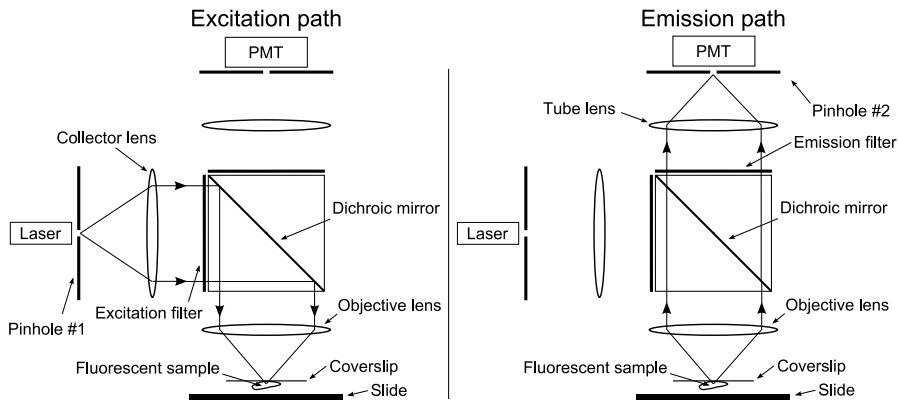


Figure 2.9: Confocal microscopy sketch. On the left we see the excitation path of the light. The object is illuminated with a laser light source through a pinhole. After the light passes the filter cube, it hits the sample. Fluorescent molecules in the sample with an excitation spectrum which matches the excitation filter and dichroic mirror reflectance spectra can be excited. On the right we see the emission path of the microscope. The excited molecules can emit photons which, if matching the emission filter and dichroic mirror transmittance spectra, can reach the PMT through a pinhole. Because of the setup with pinholes the object needs to be scanned.

Although the sample is mostly illuminated in the focal plane, it is also illuminated in regions in the out-of-focus planes. So fluorophores in this region will also be excited and emit photons. The image of the out-of-focus point will "arrive" blurred at the detection plane. The simple solution is to block this light with a second pinhole, so that most of the light in the pinhole are photons from the in-focus plane. It is easy to see from this construction that the total confocal PSF, h_{con} , can be derived from the excitation PSF, h_{ex} , and the emission PSF, h_{em} :

$$h_{con} = h_{ex} \cdot h_{em} \quad (2.5)$$

In figure 2.11 we see an example of a confocal PSF. The most striking point is

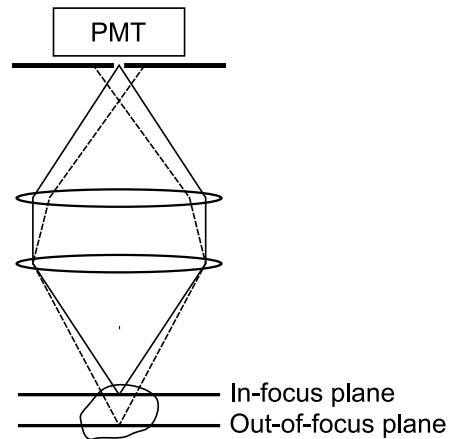


Figure 2.10: Principal of the confocal microscope: after the object is illuminated, most of the emission arriving at the pinhole will originate from the in-focus plane. Most of the light from the out-of-focus plane will be blocked at the pinhole.

that when we compare the wide-field PSF (Figure 2.7c) with the confocal PSF (Figure 2.11c) it does not look very different. But when we take a look at the confocal OTF we see that the "missing cone" has disappeared. This is because one of the properties of Fourier transforms is that a multiplication in one domain gives a convolution in the other. So the confocal OTF, H_{con} , can also be derived from the excitation and emission OTF, H_{ex} and H_{em} respectively:

$$H_{con} = H_{ex} \otimes H_{em} \quad (2.6)$$

where \otimes is the convolution operator. In figure 2.12 we see a sketch of a comparison of the wide-field OTF with the confocal OTF. Because of the convolution we see two differences. First, the cut-off frequencies have doubled. This also means that the sampling distances should be halved in confocal microscopy when compared to wide-field microscopy. Second, the "missing cone" is filled. This is the most important property of the confocal microscope: it has optical sectioning capabilities.

In figure 2.13 we see an image of a thick section of the root of a convallaria which is autofluorescent. Both images have been acquired with a confocal microscope. In figure 2.13a the pinhole has been opened as far as possible (1000 μm) to mimic a wide-field microscope. During acquisition of the image in figure 2.13b the pinhole has been set to the optimal conditions for confocal imaging: the size of 1 Airy disk (given by the system as 96 μm). The images are

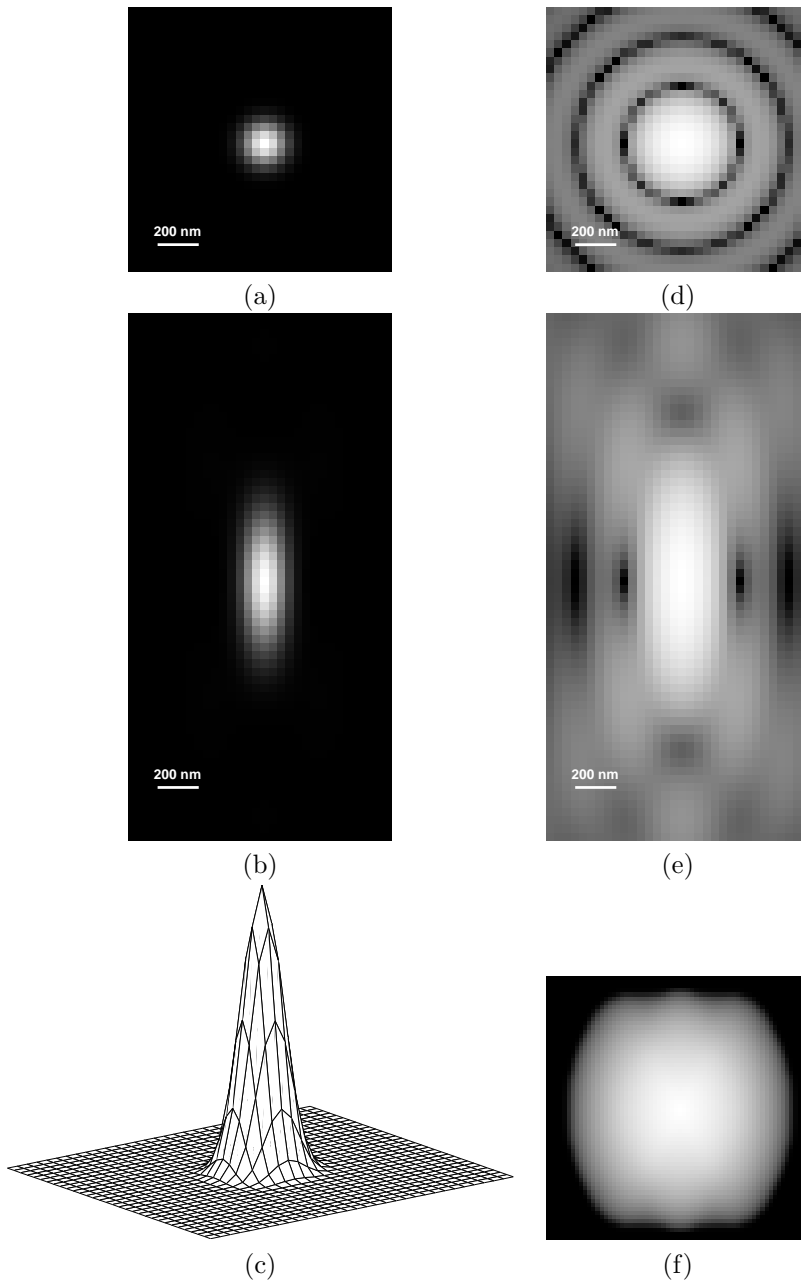


Figure 2.11: (a) shows a middle lateral (xy) section of a simulated confocal PSF. (b) shows the middle axial (xz) section of the PSF. (c) shows a mesh representation of (a). In (d) and (e) we see the same as in (a) and (b) respectively where the intensities have undergone a logarithmic stretch. (f) shows a simulated OTF of the confocal microscope.

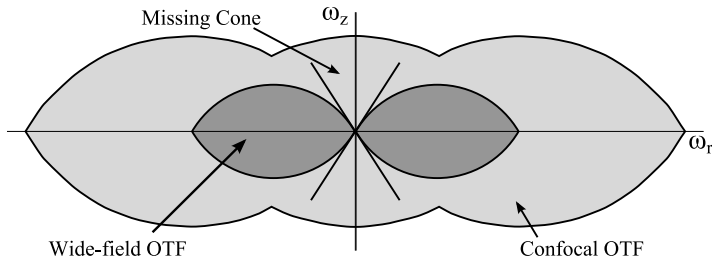


Figure 2.12: Sketch of the wide-field and the confocal OTF. We see that for the confocal OTF the cut-off frequencies have been doubled and the "missing cone" has been filled compared to the wide-field OTF.

acquired with a Zeiss LSM510 confocal system with a Plan-Apochromat 63x Oil objective with $NA = 1.4$. The sample was excited with a laser at 488 nm and a long pass 505 nm filter was used to detect mostly emitted light from the sample. In figure 2.13c we clearly see the advantage of the confocal microscope: out-of-focus light has been blocked resulting in less blur and the two lines at approximately $8 \mu\text{m}$ are now resolved.

2.4 Microscopy beyond Abbe

In section 2.2 the Abbe diffraction limit is discussed. The objective of the microscope works as a low pass filter for spatial frequencies, giving a highest possible resolving power of:

$$\delta_A = \frac{\lambda}{2NA} \quad (2.7)$$

One basic research focus in life-science microscopy the last two decades is to be able to image details as small as possible, smaller than δ_A , and therefore to break the Abbe diffraction limit. This diffraction limit tells us that this is not possible using conventional imaging: a wide-field setup. In section 2.3 the confocal microscope is discussed, where basically the diffraction limit has been broken by a factor of two in both the lateral and axial direction. The diffraction limit is closely related to the Heisenberg's uncertainty principle (Heisenberg, 1927), which basically tells us that the more accurately one can measure the position of a particle the less accurately one can measure its momentum. This means that breaking the diffraction limit will always come at a cost. Since confocal imaging is inherently a scanning system the cost therefore is time. Basically, in all high resolution imaging techniques the cost is time. Discussing all these techniques is beyond the scope of this thesis. In the following para-

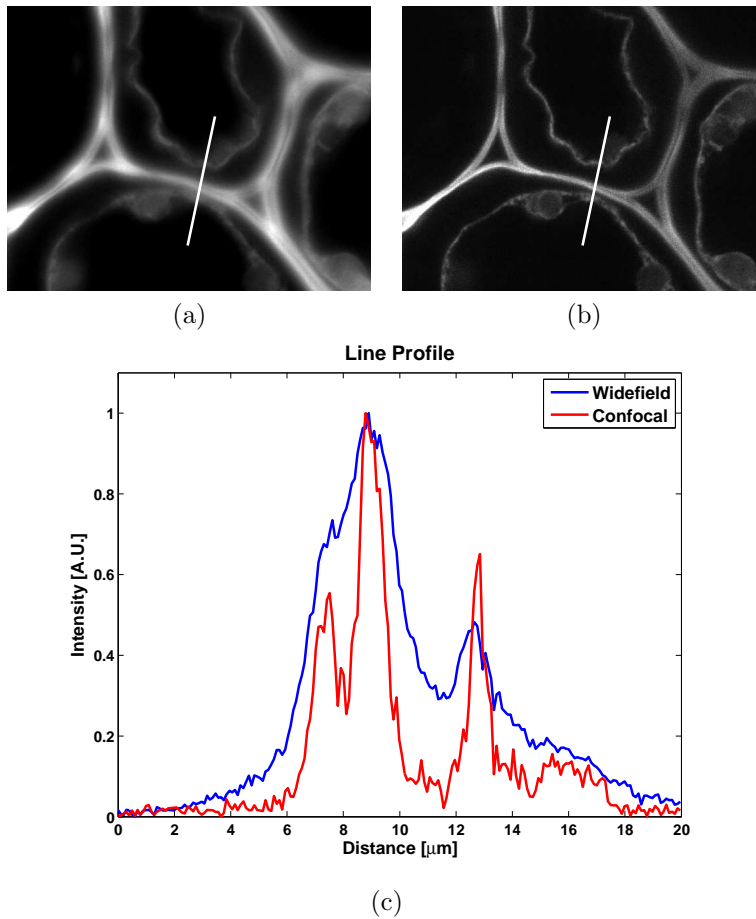


Figure 2.13: Image of the root of a convallaria. (a) wide-field image with the pinhole opened (1000 μm). (b) confocal image with the pinhole at 1 Airy disk (96 μm). The white line in both (a) and (b) is where the line profile is measured and is 20 μm long. (c) the line profile from the wide-field image (blue) clearly is less resolved than the line profile from the confocal image (red).

graphs four methods will be discussed shortly. More techniques are reviewed in (Garini et al., 2005; Hell, 2007).

2-Photon microscopy

Another method to square the PSF and thus get a better resolution and optical sectioning is to use 2-photon microscopy (Denk et al., 1990). To excite a fluorophore a specific amount of energy is needed. This does not have to be one photon with energy $E = hf$, where h is Planck's constant and f the frequency of the photon. Two photons arriving simultaneously with an energy $E/2 = hf' = h\frac{f}{2}$ can also excite the fluorophore. Now, every one of these two photons has a spatial distribution given by the PSF. So the chance of two photons arriving at the same position is again PSF^2 . Not only do the photons need to arrive at the same position but also at the same time. This is achieved by using a pulsed laser.

4Pi

The 4Pi microscope is an example of a method using the interference properties of light (Hell and Stelzer, 1992). The basic idea lies in the fact that to catch as much higher order diffractions as possible, is to collect all the light coming from the sample in a solid angle of 4π sr. Achieving this is impossible, but to mimic this the setup consists of two objectives on either side of the sample. If the excitation light now comes from both sides an interference excitation spot can be created in the sample with a better resolution than the conventional PSF. A second possibility is that the sample is excited conventionally (with one objective) but the interference is created at the detection using both objectives. The third method is to combine the first two methods, thus having interference in both the illumination and detection. An advantage of the 4Pi microscope is that, on top of an improved resolution in both the lateral as axial direction, it gives an almost spherical PSF. The improvement is most noticeable in the axial direction where resolutions up to 80 nm have been shown.

The disadvantage of this method is that the interference pattern not only has a main lobe but also two significantly large side lobes. So the acquired image always needs to be deconvolved to remove the influence of the side lobes. Another disadvantage is the alignment; since the principle of the microscope is based on interference, the two objectives need to be aligned with high accuracy. Besides that, the interference pattern is also dependent on the sample itself and therefore the alignment needs to be performed for each individual sample.

STED

STimulated Emission Depletion (STED) microscopy excites a normal PSF spot in the sample with a pulsed laser (Hell and Wichmann, 1994). Then, within the lifetime of the excited state, a second pulse is generated and the beam is shaped into a donut-like interference pattern. This donut-like pattern is projected onto the original PSF where the 'hole' of the donut coincides with the maximum of the PSF creating stimulated emission. Since the stimulated emission is a non-linear process, the emission PSF of the remaining excited fluorophores, which will emit nanoseconds later, will be much narrower than the original PSF.

The resolution of STED is dependent on the ratio of intensity of the non-depleted region, I_{max} , and the intensity of the depleted region, I_s , and is given by (Hofmann et al., 2005):

$$\delta_{STED} = \frac{\lambda}{2NA\sqrt{1 + \frac{I_{max}}{I_s}}} \quad (2.8)$$

PALM

The criterion for resolution is the smallest distance for which two point sources can be resolved after imaging. This does not mean that a single point source can not be localized with a better precision than this. The localization precision δ_x is approximately given by:

$$\delta_x \approx \frac{\sigma}{\sqrt{N}}, \quad (2.9)$$

where σ is the standard deviation of the PSF and N the number of collected photons. In (fluorescent) Photo-Activatable Localization Microscopy ((f)PALM) (Betzig et al., 2006; Hess et al., 2006) or STOchastic Reconstruction Microscopy (STORM) (Rust et al., 2006) the sample is labeled with a protein that has an 'on' and 'off' state. When starting the acquisition, the proteins need to be in a 'off' state, that is they will not be fluorescent. Using light with the appropriate wavelength the protein can be switched into the 'on' state and now is fluorescent. The key to PALM is to use such a low power of switching light that only a sparse subset of the proteins will switch from the 'off' to the 'on' state. If the distances between the 'on' proteins are far enough they can be seen as point sources, and therefore the localization precision is dependent on N . After switching, the subset of proteins can be imaged until they are photobleached. Now sub-images are created from the acquired images by fitting a 2D Gaussian distribution on the image of the single protein to get its position and replacing the wide PSF spot (with width σ) in the image with a spot at this position with a narrower spot (with width $\frac{\sigma}{\sqrt{N}}$). The total image is constructed by simply adding the sub-images. This cycle of switching 'on'

some proteins and acquiring an image is repeated until enough proteins have been imaged to form a nice total image.

The disadvantage of PALM method is time. In the original article (Betzig et al., 2006) one image would take 2~12 hours. This has improved to a couple of minutes in PALMIRA (PALM with Independent Running Acquisition) (Egner et al., 2007).

2.5 Conclusions and discussion

In this chapter fluorescence microscopy is discussed. Some terms of fluorescence are explained, like the Stokes shift and the Jablonski diagram. To detect specific DNA sequences or specific proteins in the cell nucleus we can label these with a fluorescent marker. Two popular methods to do so are FISH, where the DNA is labeled, and fused proteins, where a protein is coupled to a fluorescent protein. Then the wide-field and confocal microscopes are explained. The most important properties are given using the point spread function and the optical transfer function. The main difference being that the confocal microscope is able to, unlike the wide-field microscope, perform optical sectioning. Finally we presented some new state-of-the art high resolution techniques that have been developed in the last two decades, like 2-photon-, STED-, 4PI-microscopy and PALM.

Image restoration

This chapter will discuss several image restoration techniques. In section 3.2 the well-known Tikhonov-Miller (TM) filter, a linear restoration filter, is derived. Then section 3.3 will handle a restoration technique for a "poor-mans" confocal microscope. For this purpose a Maximum A-Posteriori restoration algorithm assuming Poisson noise and Gaussian priors (MAPPG) is chosen. It is adjusted to be able to handle two images that have been acquired simultaneously and is therefore named MAPPG2. In section 3.4 we will show that a deconvolved image of a small fluorescent object can be approximated by a Gaussian profile.

3.1 The inverse problem

The goal of image restoration is to recover some physical property of the object from its image. To do this we need to have knowledge of the image formation. The most fundamental form for this image formation can be given by the following matrix notation (Pratt, 1978):

$$g = Hf \tag{3.1}$$

Here the object, f , and the PSF, H , are both sampled and g is the resulting image. When the image has size $M = m \times n \times k$ voxels, both f and g will be column vectors with size $1 \times M$ and H a matrix with size $M \times M$. In this formalism the PSF can be spatially variant. However when the PSF is spatially invariant this equation can be most efficiently implemented in the Fourier domain where the spatial matrix multiplication becomes an element-by-element multiplication in the frequency domain. Equation 3.1 has to be rewritten if we want to include a known background and a noise process. The inclusion of a known background will lead to better results in restoration algorithms using a non-negativity constraint (i.e. the object can only have zero or positive values). The most commonly used models for noise are Gaussian and Poisson noise. The image formation equation that takes into account both the

background and noise is given by:

$$g = N(Hf + b) \quad (3.2)$$

where b is the known background and $N(\cdot)$ is the noise process.

When we look at equation 3.1, the most intuitive restoration algorithm would be:

$$\hat{f} = \frac{g}{H} \quad (3.3)$$

Here \hat{f} is the restored object. The problem is that, in general, H does not have an inverse because some of its eigenvalues are zero. For example, if the one-dimensional transfer function is a rectangular pulse, than its Fourier transform is a sinc-function. This function has zero-crossings and that is where spectral information of the object is lost after convolution. Because of these zero-crossings we cannot restore by simple division in the Fourier domain; we would be dividing by zero.

Another approach is minimizing the squared difference between the blurred object and the image, which leads to minimizing the functional:

$$\Psi = \| Hf - g \|^2 \quad (3.4)$$

The least squares estimate is obtained by setting the derivative of this functional to zero, which results in the pseudo-inverse:

$$\hat{f} = \frac{H^T g}{H^T H} \quad (3.5)$$

where H^T is the transpose of matrix H . This also doesn't work because some of the non-zero eigenvalues are still too small. These kinds of problems, where eigenvalues are small or zero, are called ill-posed. Image recovery without any other knowledge than the blurring matrix H , is, therefore, impossible.

This means we need some other information. This can be information on smoothness, non-negativity or some other physically meaningful a priori constraint. Some examples of linear filters that are commonly used are Tikhonov-Miller and Wiener filters. But because these filters are still linear they have the big drawback that they cannot recover lost frequencies. Especially in wide-field imaging, where the "missing cone" problem exists, but also in confocal imaging, we want to recover those lost frequencies. This is called super-resolution restoration. Non-linear algorithms have shown this super-resolution property (Conchello, 1998; Markham and Conchello, 2001).

3.2 Tikhonov-Miller (TM) restoration

The TM filter makes use of the Lagrange multiplier. Besides minimizing the squared difference in equation 3.4, we also make use of the fact that energy, E ,

in the image has to be constant:

$$E = \| f \|^2 \quad (3.6)$$

The method of the Lagrange multiplier states that the gradient of the function to be minimized is proportional to the gradient of some side condition. Here the side condition is derived from equation 3.6 and is:

$$\varphi = \| f \|^2 - E = 0 \quad (3.7)$$

Then the equation to be solved is:

$$\nabla \Psi + \gamma \nabla \varphi = 0 \quad (3.8)$$

where γ is the Lagrange multiplier. Solving this equation gives the TM estimate:

$$\hat{f}_{TM} = \frac{H^T g}{H^T H + \gamma} \quad (3.9)$$

In image restoration the Lagrange multiplier is also called the regularization parameter, because it regularizes the amount of smoothing in the restoration result. Increasing this parameter will increase smoothing. Setting it to zero will again give us the least squares estimate.

3.3 3D Restoration with multiple images acquired by a modified conventional microscope

B.J. Vermolen, Y. Garini, I.T. Young

This section was first published in *Microscopy Research and Technique* (Vermolen et al., 2004).

3.3.1 Abstract

A problem in high magnification microscopy is the blurring in the imaging of an object. In this article we demonstrate a restoration technique that simultaneously makes use of the confocal image and the wide-field image. These images can be acquired by a modified conventional microscope. In front of the light-source there is an array of pinholes. There are no pinholes at the detection plane. Instead one or more pixels from the CCD camera are used, where the pinholes would have been. Using all pixels gives the wide field image, but using a selected subset can give a confocal image. The array is used to speed up the process of acquiring the image. Note that the speed of acquisition is proportional to the number of pinholes. We show that the restoration from the two images can lead to a better result than using only one of the images. If this is the case, we show that a distance of 5 times the diameter of the pinholes can give the same results as a distance of 20 times after deconvolution. This offers an increase in acquisition time of a factor 16.

3.3.2 Introduction

In applications such as fluorescent *in situ* hybridization (FISH) where specific DNA sequences can be stained, e.g. the telomeres, it is desirable to acquire images with the highest possible resolution. A problem in microscopy is that the lens system has limited resolving power; it acts as a low-pass filter. There are several ways to improve the resolution. Using a confocal microscope will pass higher spatial frequencies, especially in the direction of the optical axis, but at the cost of blocking photons. Another way is to deconvolve the image. This is a mathematical process done after the image has been acquired. Deconvolution can be done on the wide-field image but also on the confocal image. We use an algorithm that involves two images that are simultaneously acquired. This is done using a modified conventional microscope where an array of pinholes is placed in front of the light-source and a CCD camera is placed in the detection plane. A trade off is implied between speed and confocality. There are more pinholes in the array if they are placed close together, which increases speed of acquisition but this setup will have less optical sectioning power (Verweer et al., 1998). The extreme case, where the pinholes are placed infinitesimally close to one another, is equivalent to a wide-field microscope. In this article

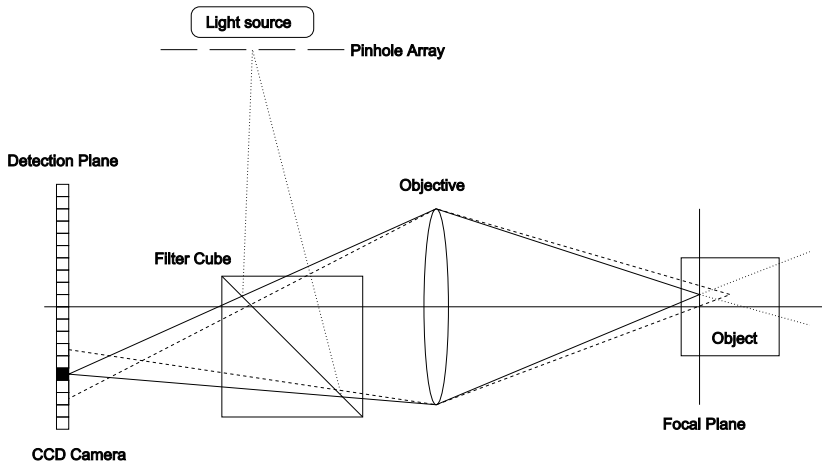


Figure 3.1: Setup of our epi-fluorescence microscope. The in-focus information from one pinhole is acquired by the black pixel. The surrounding pixels contain the out-of-focus blur.

we show the modified microscope and an algorithm for restoration. We discuss some practical problems to consider when doing simulations of acquisition and restoration. This includes topics like choice of the regularization parameter, noise, background and initial estimates for the restoration algorithm. Then we discuss the results from the simulations. Here we show that when we take images of spheres with a low signal-to-noise ratio (SNR) the pinholes can be placed as close together as 5 times the diameter of a single pinhole and, after restoration, the results will be equivalent to pinholes placed at a distance that is 20 times this diameter.

3.3.3 Materials and methods

Hardware and software

The presented results are all simulations done on an AMD Athlon XP 2700+ system. The software was written in MatLab code and run in MatLab 6.5 (R13). The software also makes extensive use of DIPimage 1.4.1 (Luengo Hendriks et al., 1999).

A modified microscope

In figure 3.1 we see the proposed microscope. The setup is similar to a conventional epi-fluorescent microscope with some modifications. In front of the

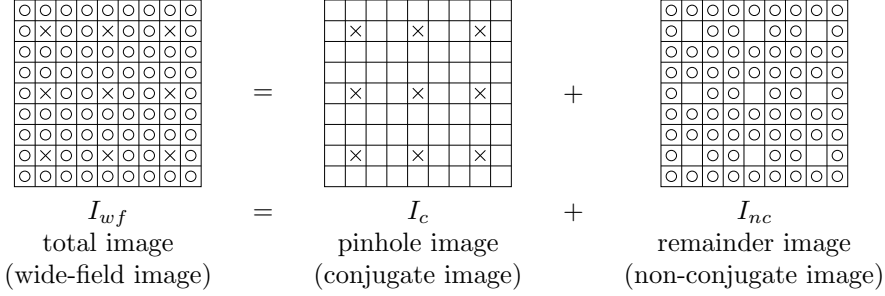


Figure 3.2: The total image is the actual acquired image by the camera, the pinhole image that would have been acquired if pinholes were used and the remainder image is the total image minus the pinhole image. Scanning the object gives a series of images which will form the conjugate, the non-conjugate and the wide-field image.

light-source, in the conjugate focal plane, is an array of pinholes and in the detection plane, the other conjugate focal plane, a CCD camera. A normal confocal microscope achieves its optical sectioning properties through two pinholes where the pinhole in front of the detector, blocks the out-of-focus blur. This microscope does the same by taking into account the pixels with coordinates corresponding to the place where the pinhole would have been, as illustrated in figure 3.2. Scanning the object using only these CCD pixel-‘pinholes’ forms the conjugate image. With one pinhole we would call it the confocal image; the remainder of the pixels form the non-conjugate image. Note that adding the conjugate, I_c , and the non-conjugate image, I_{nc} , gives the wide-field image:

$$I_{wf} = I_c + I_{nc} \quad (3.10)$$

Assuming a spatially-invariant PSF, H , the generic image formation can be represented as a convolution of the object, O , with the PSF:

$$I = H * O \quad (3.11)$$

The wide-field image is then formed by replacing H with the emission PSF, H_{em} . The PSF of the conjugate image formation, H_c , is given by [Verveer et al. \(1998\)](#):

$$H_c(x_o, y_o, z_o) = H_{em}(x_o, y_o, z_o; \lambda_{em}) \int_{-\infty}^{+\infty} \int_{-\infty}^{+\infty} G\left(\frac{q}{M}, \frac{r}{M}\right) \times H_{ex}\left(\frac{q}{M} - x_o, \frac{r}{M} - y_o, z_o; \lambda_{ex}\right) dq dr \quad (3.12)$$

where (x_0, y_0, z_0) is the 3D coordinate system in object space, G is the array function, M is the magnification of the lens and λ_{em} and λ_{ex} respectively the emission and excitation wavelengths. The PSF of the non-conjugate image formation, H_{nc} is the conjugate PSF subtracted from the wide-field PSF:

$$H_{nc} = H_{em} - H_c \quad (3.13)$$

Restoration

Another way of writing equation 3.11 in its most fundamental form is by using the following matrix notation (Pratt, 1978):

$$g = Hf \quad (3.14)$$

Here the object, f , and the PSF, H , are both sampled and g is the resulting image. Introducing a background, b , and noise process, $N(\cdot)$, equation 3.14 becomes:

$$g = N(Hf + b) \quad (3.15)$$

For this study we have chosen to implement the MAPPG restoration algorithm (Verveer and Jovin, 1997). MAPPG is an abbreviation for Maximum A Posteriori with Poisson statistics and a Gaussian prior. A MAP algorithm implies maximizing the a posteriori density function, $p(f | g)$, which is according to Bayes' rule:

$$p(f | g) = \frac{p(g | f)p(f)}{p(g)} \quad (3.16)$$

In words, we would like to find the most likely image f that led to the measured image g . Because $p(g)$ is constant, maximizing the left side of equation 3.16 is equivalent to maximizing the numerator of the right side of equation 3.16. This means that we must choose a prior density, $p(f)$, and a conditional density function, $p(g | f)$.

For the prior density we choose a Gaussian distribution:

$$p(f) \propto \exp\left(-\frac{1}{2\tau^2} \| C(f - m) \|^2\right) \quad (3.17)$$

where τ can be used as a penalty term and C and m are in image restoration, commonly known as, the regularization matrix and the model respectively. Choosing a Gaussian distribution for the prior density is an arbitrary choice. Because we have no prior knowledge of the object, any assumption of a model would be arbitrary. Still a Gaussian distribution is chosen because the Gaussian distribution is computationally simple and because one could argue that the intensity distribution in images often resembles a superposition of Gaussian distributions.

The conditional density function will be a statistical model. Poisson statistics are chosen because the acquisition of an image can best be described as a photon counting process (Mandel and Wolf, 1995). If we assume pixel independence we can write this as:

$$p(g|f) = \prod_{i=1}^K \frac{\mu_i^{N_i} \exp(-\mu_i)}{N_i!} \quad (3.18)$$

where $\mu_i = \beta[Hf + b]_i$ is the mean, $N_i = \beta g_i$ is the number of photons, β is the photon-conversion factor, and K is the size of the image (in pixels).

Now we obtain the MAPPG functional Ψ_{PG} by substituting equation 3.17 and equation 3.18 in equation 3.16 and taking the negative of the logarithmic. Leaving out the terms that are independent of f gives us the functional:

$$\Psi_{PG} = \sum Hf - g^T \ln(Hf + b) + \gamma \| C(f - m) \|^2 \quad (3.19)$$

Here γ is the regularization parameter and T the transpose operator. In the rest of this report the regularization matrix, C , will be chosen as unity and m zero as in Verveer (Verveer and Jovin, 1997).

To implement a non-negativity constraint a transformation of variables is made: $f = e^2$. If E is given by the diagonal matrix with $E_{ii} = e_i$, then the new functional is given by

$$\Psi_{PG} = \sum H e^2 - g^T \ln(H e^2 + b) + \gamma \| e^2 \|^2 \quad (3.20)$$

and its gradient by:

$$\nabla \Psi_{PG} = 2E(H^T(1 - \frac{g}{H e^2 + b}) + 2\gamma e^2) \quad (3.21)$$

By minimizing Ψ_{PG} with respect to e we obtain our MAP estimates. This minimization is described in Verveer (Verveer and Jovin, 1997) and uses the nonlinear conjugate gradient algorithm.

The MAPPG algorithm is made suitable for multiple images by replacing one image, g , by a vector of images:

$$g = (c_1 g_1 \quad c_2 g_2 \quad \dots \quad c_N g_N) \quad (3.22)$$

The same is done for the PSF:

$$H = (c_1 H_1 \quad c_2 H_2 \quad \dots \quad c_N H_N) \quad (3.23)$$

Here c_i is a weighting factor which will be discussed later and N is the number of images. Substituting equations 3.22 and 3.23 in equations 3.20 and 3.21 gives the new functional:

$$\Psi_{PG} = \sum_{i=1}^N \left(\sum c_i H_i e^2 - c_i g_i \ln c_i H_i \right) + \gamma \| e^2 \|^2 \quad (3.24)$$

and its gradient:

$$\nabla \Psi_{PG} = 2E \left(\sum_{i=1}^N c_i H_i \left(1 - \frac{c_i g_i}{c_i H_i e^2} \right) + 2\gamma e^2 \right) \quad (3.25)$$

In our case $N = 2$, the conjugate and the non-conjugate image. We call this multi-image restoration algorithm MAPPG2.

Weighting factors

The choice of the weighting factors has a high impact on the quality of the restoration. A simple choice is to consider the fact that the noise in the images is Poisson noise. This means that for both images the conversion factor, β , should be the same. So we choose as weighting factors:

$$\frac{c_1}{c_2} = \frac{\beta_1}{\beta_2} \quad (3.26)$$

Because in our system $\beta_1 = \beta_2$ we simply choose $c_1 = c_2 = 1$. There are similar systems, where a conjugate and non-conjugate image are acquired simultaneously, e.g. the Programmable Array Microscope (PAM) (Verveer et al., 1998). The difference is that there the detectors do not have to be the same. MAPPG2 can be applied there but because $\beta_1 \neq \beta_2$ we need to use these weighting factors.

Regularization parameter

The regularization parameter is calculated with the method of generalized cross validation (GCV) (Galatsanos and Katsaggelos, 1992).

The basic idea is that a regularization parameter is calculated using a leave-one-out principle with the Tikhonov-Miller filter (Tikhonov and Arsenin, 1977). Tikhonov-Miller restoration is applied to all pixels except the pixel under consideration. Then the mean squared error (MSE) is calculated between the original data and the restoration result derived by filtering each pixel with its associated Tikhonov-Miller filter. We therefore have to minimize (Galatsanos and Katsaggelos, 1992):

$$GCV(\gamma) = \frac{\sum |(I - HA(\gamma))g|^2}{[\text{trace}(I - HA(\gamma))]^2} \quad (3.27)$$

with respect to γ . This gives us an estimate of the regularization parameter to be used for the Tikhonov-Miller filter, γ_{TM} . Here I is the identity matrix and A the Tikhonov-Miller filter:

$$A(\gamma) = \frac{H^T}{H^T H + \gamma} \quad (3.28)$$

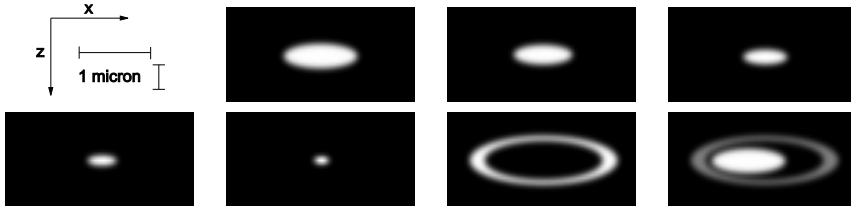


Figure 3.3: Test-objects. These images are the center slices of the full 3D image stack. Note that the spheres look oblate because the pixel distance in the z -direction is larger than in the x -direction.

Equation 3.27 can be written in the Fourier domain, where ω is the spatial frequency:

$$GCV(\gamma) = \frac{\sum_{\omega} \frac{\gamma^2 |G(\omega)|^2}{(|H(\omega)|^2 + \gamma)^2}}{(\sum_{\omega} \frac{\gamma}{|H(\omega)|^2 + \gamma})^2} \quad (3.29)$$

Minimizing is done using Brent's minimization algorithm (Press et al., 1992). As explained in (Kempen, 1998) we now have to simply divide the outcome, γ_{TM} , by 2 and the mean of the image, \bar{g} to determine the regularization parameter to be used in MAPPG:

$$\gamma_{MAPPG} = \frac{\gamma_{TM}}{2\bar{g}} \quad (3.30)$$

This regularization parameter has shown to be quite effective. For a better understanding and derivation of the GCV function see (Golub et al., 1979).

Test-objects

The test-objects in the simulations have been created with DIPimage (Lungo Hendriks et al., 1999). Here band-limited images of objects can be made. These are implemented in Fourier space and then transformed into the spatial domain (Kempen, 1998). Because a real object has spatial frequencies into infinity and a simulation of an object is sampled, the Nyquist criterion can never be met. To avoid aliasing effects the object is convolved with a Gaussian. According to van Vliet and Verbeek (1994) only simulated objects free from aliasing can give a good representation of the real object.

Different test-objects have been chosen. In figure 3.3 are spheres with varying diameter (1 μm , 800 nm, 650 nm, 350 nm, 200 nm) and a maximum intensity of 200 ADU (Analog-to-Digital Unit). A shell with an outer diameter of 2 μm which is 200 nm thick with a maximum intensity of 200 ADU. The same shell combined with a shifted sphere (-200 nm in the x -direction) of 1

μm where the sphere has a maximum intensity of 200 ADU and the shell a maximum of 100 ADU. All these objects are convolved with an anti-aliasing Gaussian with $\sigma = 40$ nm as previously described. Furthermore all images are shifted a random sub-pixel distance, creating asymmetry.

Noise

Acquiring images introduces noise. Poisson noise dominates other noise sources such as thermal noise, KTC-noise or quantization noise (Young et al., 1998). Therefore, only Poisson noise is simulated. An algorithm has been implemented in DIPimage (Luengo Hendriks et al., 1999) which uses the reciprocal of the photon conversion factor, β , as a parameter to vary the SNR:

$$SNR = 10 \log(\beta\mu) \quad (3.31)$$

The algorithm for Poisson noise can be found in Knuth (1969). In our simulations we used a β that corresponds to an SNR of 25 dB and 40 dB in the wide-field image. Since Poisson noise is dependent on the signal, we had to choose some μ as the signal. Here we chose the maximum of the wide-field image:

$$\beta = \frac{10^{\frac{SNR}{10}}}{\max(g_{\text{wide-field}})} \quad (3.32)$$

This means that the SNRs of the conjugate images are far less than this 25 or 40 dB, because the signal, μ , is smaller.

Background

In all simulations we assume a constant background. As shown in figure 3.4, the image has size 2×2 and the total image acquired by the camera consists of a confocal and a non-confocal part. The number in the pixel represents its background and not the signal. For every pixel in the resulting confocal image we need to take one total image. One of the pixels of the total image is for the confocal image and the others for the non-confocal image. This leads to a total background in the resulting confocal image of intensity 1, the resulting background in the non-confocal image of intensity 3, and the resulting background value for the conventional wide-field image of intensity 4. It is now easy to see that if one pinhole has to scan over an area with size $M \times N$ and the wide-field image has a known background bg then the conjugate image has a background of

$$bg_c = bg \frac{1}{M \times N} \quad (3.33)$$

and the non-conjugate image a background of

$$bg_{nc} = bg \left(1 - \frac{1}{M \times N}\right) \quad (3.34)$$

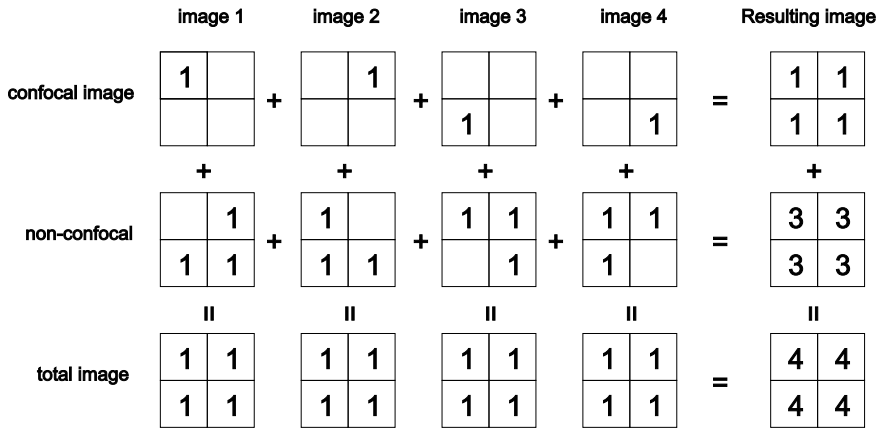


Figure 3.4: An example of the relation between the background of the confocal, non-confocal and wide-field image. The number in the pixels represent the intensity of the background.

The example of figure 3.4 is consistent with this. Note that $bg = 4$ and so $bg_c = 1$ and $bg_{nc} = 3$.

Initial estimate

An initial estimate is necessary for the MAPPG and MAPPG2 algorithm. It is important to choose a suitable image for this. Choosing a wrong image will not always converge to the solution that was expected. Some alternatives for initial estimates are: the original wide-field data, the original confocal data, smoothed versions of these. Another way is to calculate the estimate with the Tikhonov-Miller filter, see equation 3.28, using the wide-field or the confocal data. The Tikhonov-Miller estimate from the confocal data gave the best overall results in our simulations, therefore was chosen as the initial estimate.

Comparing results

To compare the different restorations the MSE is used as a measure. The MSE between the object, f , and the restored image, \hat{f} , is defined as:

$$MSE(f, \hat{f}) = \frac{1}{K} \sum_i (\hat{f}_i - f_i)^2 \quad (3.35)$$

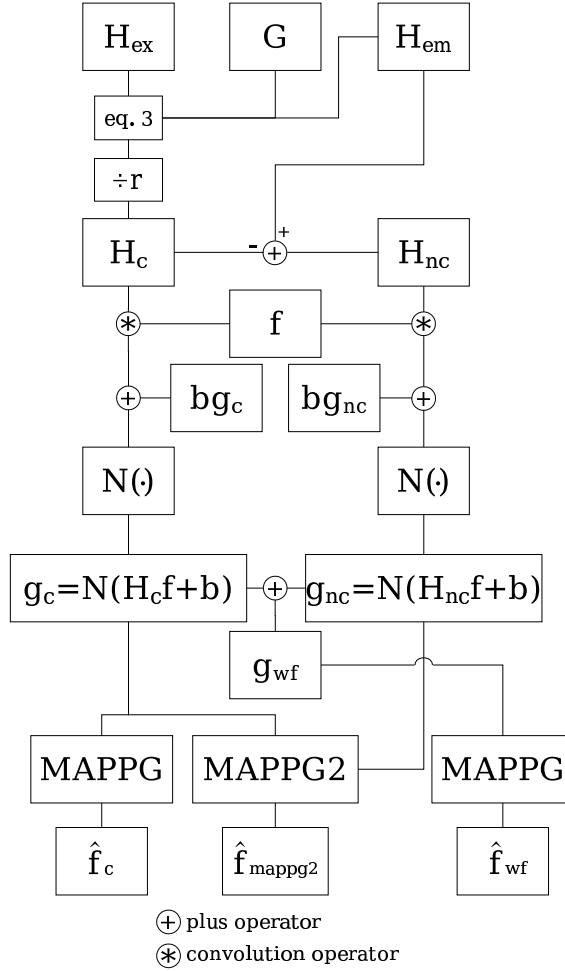


Figure 3.5: Flow diagram, from top to bottom, illustrating the simulation

Algorithm of simulations

The algorithm is presented in figure 3.5. First the test-object, f , was simulated in an image of $64 \times 64 \times 32$ pixels with a pixel distance of 40 nm in the xy -direction and 120 nm in the z -direction. Then we simulated the excitation, H_{ex} , and the emission PSF, H_{em} , with excitation wavelength 488 nm and emission wavelength 590 nm (e.g. SNARF-1), the refractive index of the immersion oil is 1.518 and a numerical aperture of 1.4 (Voort and Brakenhoff, 1990). The

diameter of the back-projected pinholes, $D_{pinhole}$, was 200 nm. The lattice distance of the array, G , was $\delta_{xy} = \{2, 5, 10, 20\} \cdot D_{pinhole}$. From these we construct the conjugate, H_c , and the non-conjugate PSF, H_{nc} . To simulate the fact that fewer photons are used in the conjugate image than in the wide-field image we chose to divide the conjugate PSF by $r = \{50, 100, 150\}$. So r is the ratio between the sum of the wide-field PSF and the conjugate PSF. We determine the non-conjugate PSF by subtracting the conjugate PSF from the wide-field PSF. After convolution of the object with the conjugate and the non-conjugate PSF we add background, bg , and corrupt the data with Poisson noise, $N(\cdot)$. The wide-field image, g_{wf} , is then simply the sum of the conjugate image, g_c , and the non-conjugate image, g_{nc} . Then we apply restoration on the conjugate image and the wide-field image separately with MAPPG, which gives us the estimates \hat{f}_c and \hat{f}_{wf} . And on the conjugate and non-conjugate image combined we apply MAPPG2 which gives us \hat{f}_{mappg2} .

3.3.4 Results

In figure 3.6 to figure 3.12 we see the results of the simulations. For every object, noise level of the wide-field image and ratio, r , there is a graph. The first thing we notice is that the restorations from the wide-field images almost always perform better than the restorations from the conjugate image. This is easily explained, because, as mentioned in the section on noise, the SNR of the conjugate image is lower because of the lower signal.

Compared to the restorations from the wide-field images it looks like the MAPPG2 restorations perform better if the SNR is smaller. We suspect that this is an effect of the difference in ratio of the SNR of the wide-field image and the SNR of the conjugate image. Take for example the $1 \mu\text{m}$ sphere with $r = 50$. There are 2 situations. Situation 1 is when the SNR of the wide-field image is 25, then in the conjugate image: SNR= 8.4. So the SNR in the conjugate image is 3 times smaller than in the wide-field image. The second situation: if the SNR for the wide-field image is 40, then in the conjugate image: SNR= 23.4. So here the SNR is 1.7 times smaller. For the first situation the minimization algorithm will relatively look more at the conjugate image than in the second situation. In this case, where the MAPPG2 restoration performs better than the wide-field restoration, we also see that most of the time this will happen with an array that has pinholes distances down to 5 times the diameter of the pinhole. Compared to 20 times this diameter this means an increase of acquisition speed of a factor 16.

The object where we have a sphere in a shell shows that the optical sectioning powers become important. In contrast to what was mentioned before, the higher SNR MAPPG2 restoration performs better compared to the wide-field restoration. The structure of a sphere close to a shell is better preserved in the

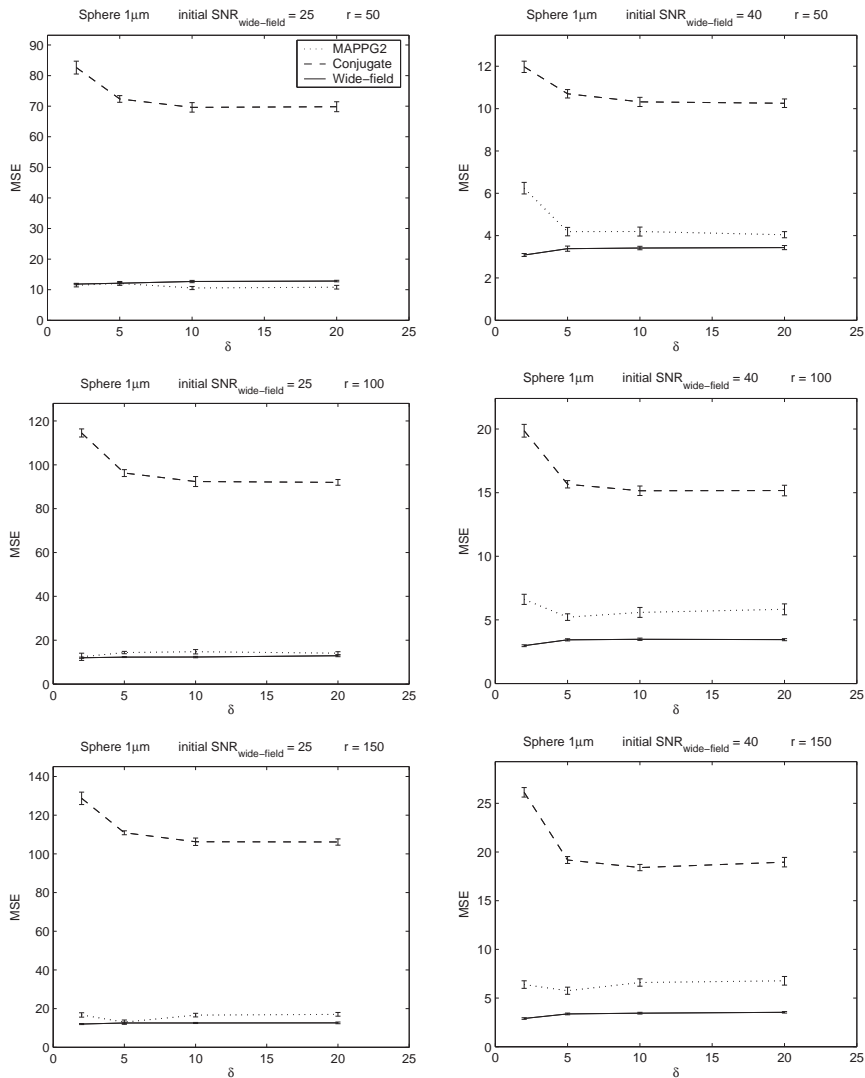


Figure 3.6: The figures show the MSE values of the MAPPG restored conjugate and wide-field images and of the MAPPG2 restored image. These are plotted against the distance between the pinholes normalized by the diameter of the pinhole. The object is a sphere with $1\mu\text{m}$ diameter.

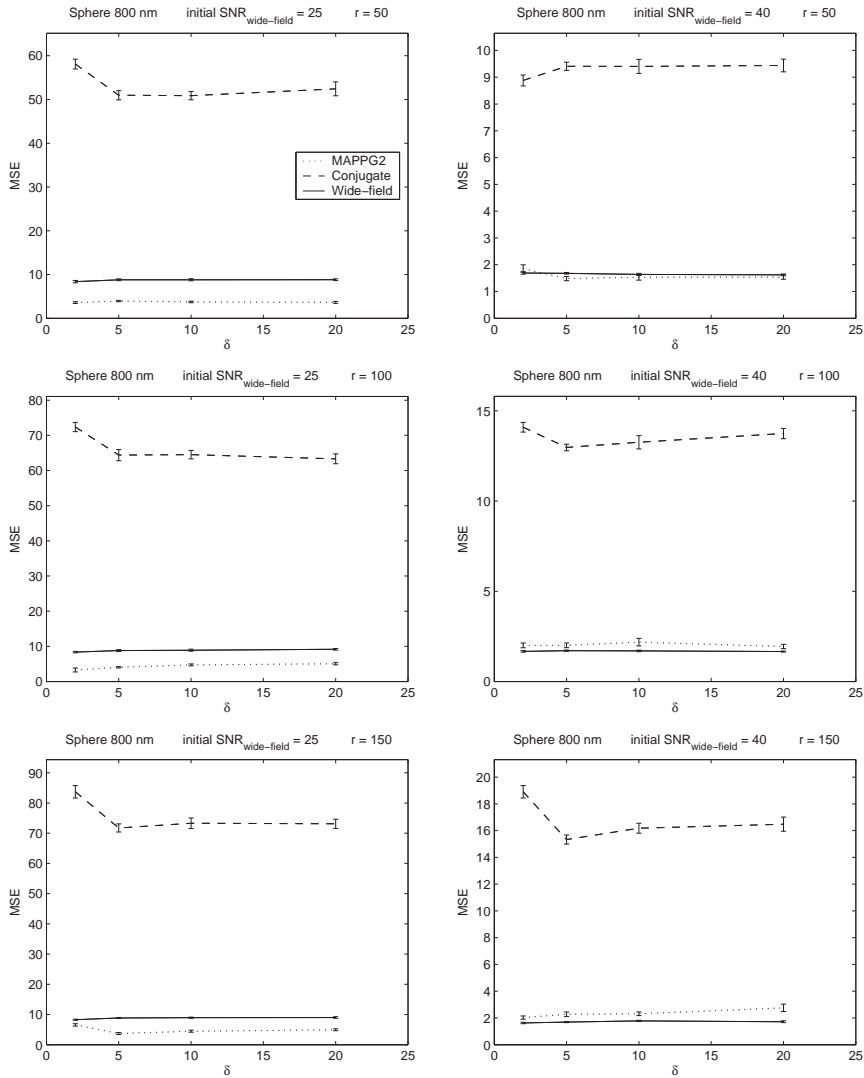


Figure 3.7: The figures show the MSE values of the MAPPG restored conjugate and wide-field images and of the MAPPG2 restored image. These are plotted against the distance between the pinholes normalized by the diameter of the pinhole. The object is a sphere with 800 nm diameter.

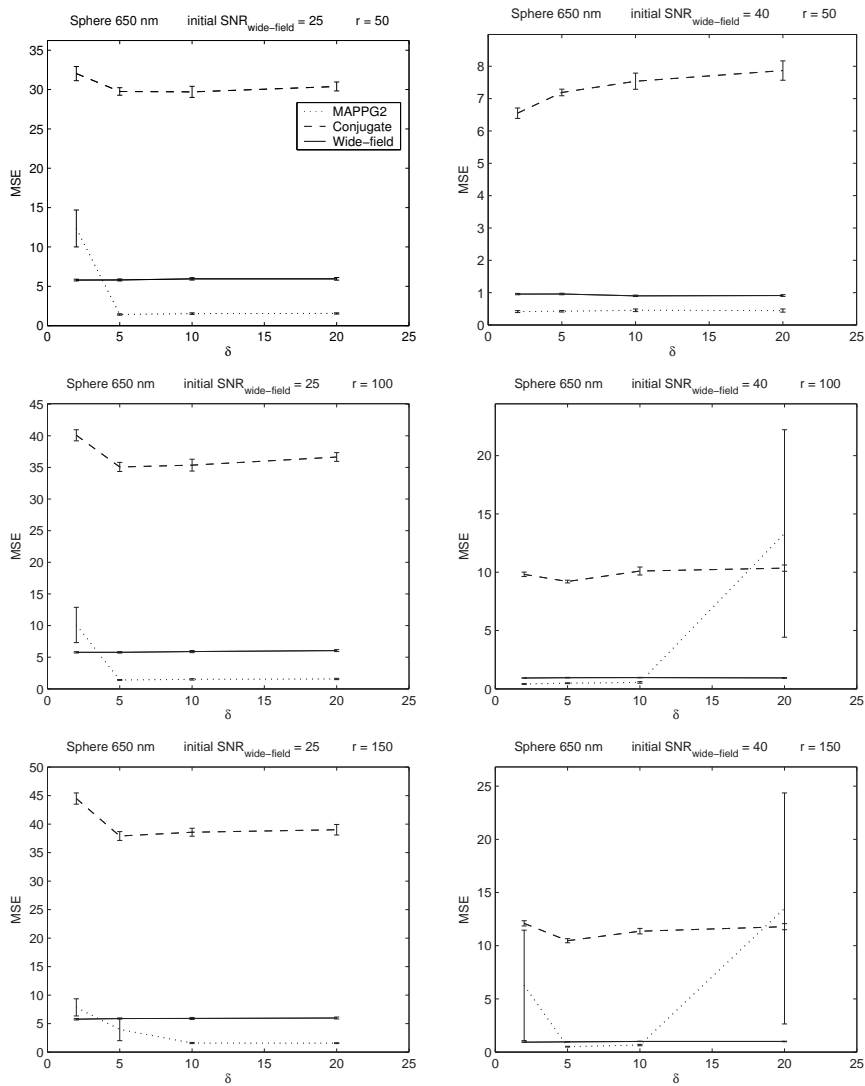


Figure 3.8: The figures show the MSE values of the MAPPG restored conjugate and wide-field images and of the MAPPG2 restored image. These are plotted against the distance between the pinholes normalized by the diameter of the pinhole. The object is a sphere with 650 nm diameter.

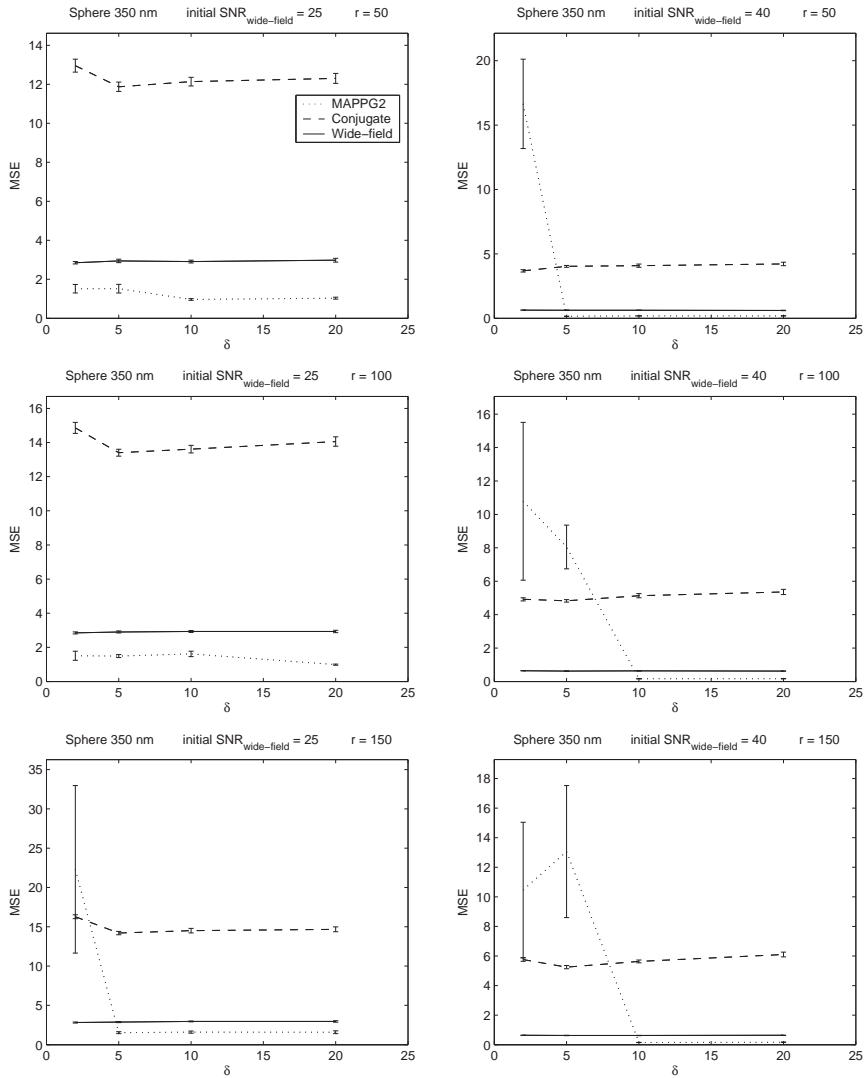


Figure 3.9: The figures show the MSE values of the MAPPG restored conjugate and wide-field images and of the MAPPG2 restored image. These are plotted against the distance between the pinholes normalized by the diameter of the pinhole. The object is a sphere with 350 nm diameter.

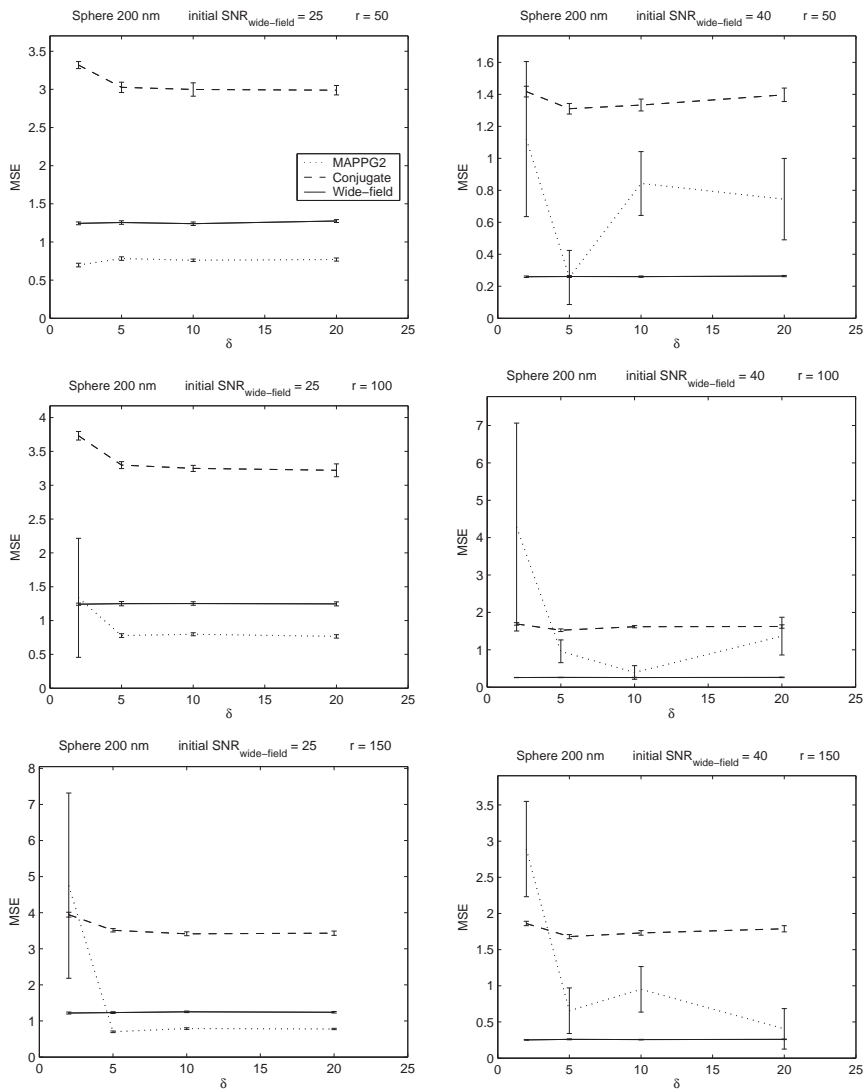


Figure 3.10: The figures show the MSE values of the MAPPG restored conjugate and wide-field images and of the MAPPG2 restored image. These are plotted against the distance between the pinholes normalized by the diameter of the pinhole. The object is a sphere with 200 nm diameter.

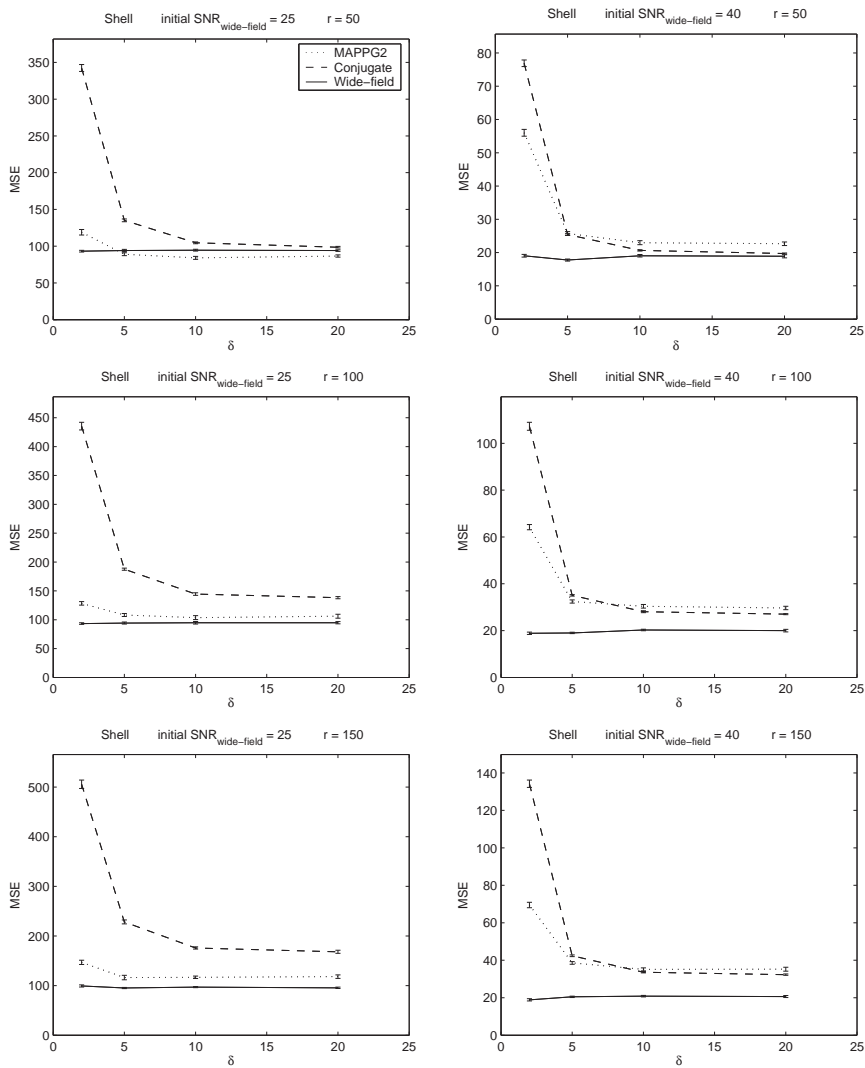


Figure 3.11: The figures show the MSE values of the MAPPG restored conjugate and wide-field images and of the MAPPG2 restored image. These are plotted against the distance between the pinholes normalized by the diameter of the pinhole. The object is a shell with an outer diameter of $2 \mu\text{m}$ and which is 200 nm thick.

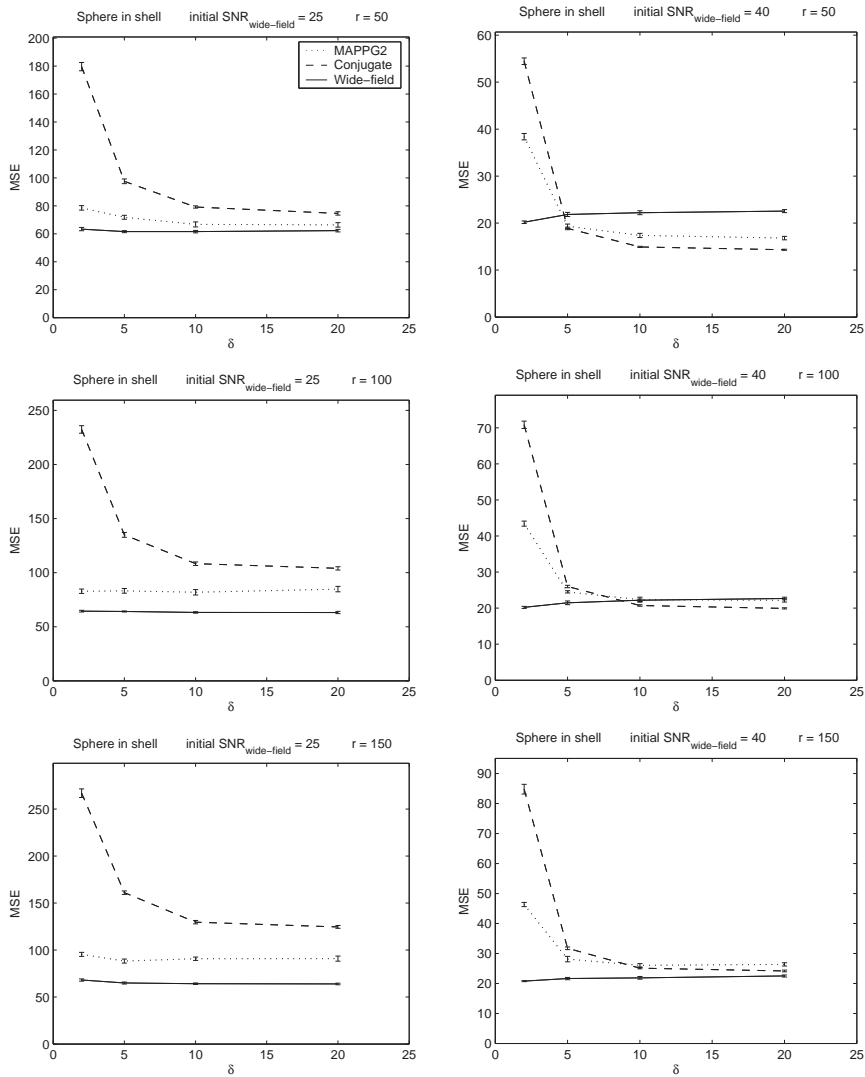


Figure 3.12: The figures show the MSE values of the MAPPG restored conjugate and wide-field images and of the MAPPG2 restored image. These are plotted against the distance between the pinholes normalized by the diameter of the pinhole. The object is a shell with an outer diameter of $2 \mu\text{m}$ and which is 200 nm thick. In the shell is a sphere with a diameter of $1 \mu\text{m}$ which is shifted -200 nm in the x-direction.

conjugate image than in the wide-field image. For low r this even leads to a better restoration from the conjugate image than from the wide-field image.

In the case of the 650 nm sphere we see in SNR= 40 at $r = 100$ and 150 we see a larger value for $\delta = 20$. This shows that the algorithm is not always as stable. It depends on the object, initial estimate and if the noise 'falls right'. Here we mean that if the noise in the image by accident looks to have some structure the algorithm will try to comply to this structure.

3.3.5 Discussion

In this article we show that it is possible to do restorations on images acquired by a modified conventional microscope. The quality of these restorations are dependent on a number of factors: the object, the initial estimate, the ratio r , and the SNR of the acquired images.

In most all cases it seems that the conjugate image is not a good choice to use for restoration. This is because the SNR of the conjugate image is much lower than the SNR of the wide-field image. Only in the case where there is more structure, like in the sphere in the shell, the benefits of better optical sectioning compensates for the lower SNR.

With smaller spheres and low SNR the MAPPG2 restoration algorithm shows improvement in the resulting restored image compared to restoring the wide-field image. Here the distance of the pinholes in the array can be close together, down to 5 times the diameter of the pinholes. This means an increase of speed of a factor 16 compared to an array with a distance of 20 times the pinhole.

3.4 Gaussian approximation of deconvolved images acquired by a wide-field microscope

3.4.1 Introduction

In (Zhang et al., 2007) it is shown that the 3D confocal PSF is a close approximation of a 3D Gaussian profile. They also show that the 3D wide-field PSF cannot be approximated by a 3D Gaussian. In this section we will show that the deconvolved wide-field image of a small fluorescent object can be approximated by a 3D Gaussian.

3.4.2 Methods

To simulate a small object we made a test object, f , by constructing an image with size $128 \times 128 \times 128$ voxels. The sampling distance in the lateral direction is $dr = 26.5$ nm, and in the axial direction $dz = 50$ nm. These are approximately the sampling distances according to the Nyquist sampling theorem, divided by four. In the middle of this image we create an object with a Gaussian profile with width $\sigma = 1$ pixel. Now we have an oversampled image of the object, which is a point source; an object smaller than the PSF spot. We also create a PSF, h , according to Gibson and Lanni (1991) with wavelength $\lambda = 560$ nm, magnification $M = 63x$, numerical aperture $NA = 1.32$ and refractive index of the immersion fluid $n = 1.515$. We create an intermediate image, g_{int} , by convolving the object with the PSF:

$$g_{int} = h \otimes f \quad (3.36)$$

where \otimes is the convolution operator. Now we simulate an image recorded by the camera by integrating a region of 4×4 pixels in every xy-slice and subsampling by a factor of 4 in the z direction. This gives us new sampling distances in the lateral direction $dr = 106$ nm, and in the axial direction $dz = 200$ nm. Hereafter we corrupt the resulting image with Poisson noise:

$$g = N(g_{int}) \quad (3.37)$$

where $N(\cdot)$ is a Poisson noise process. We have chosen to normalize the mean of the maximum number of counted photons in g_{int} to be $\mu = 100$, which gives a signal-to-noise ratio of $\frac{\mu}{\sigma} = \frac{\mu}{\sqrt{\mu}} = \sqrt{\mu} = 10$ according to Poisson noise theory.

The next step is to deconvolve the image using the MAPPG deconvolution method as described by (Verveer and Jovin, 1997) and in section 3.3.3. We will use a set regularization parameter, $\gamma = 10^{-6}$, which gives satisfactory results.

Then we will do a least squares fit of a Gaussian as in Zhang et al. (2007) using the L^1 constraint, which conserves energy. Practically it means we will normalize the sum of the pixels in the image. The L^∞ constraint, where the

image is normalized to its maximum, cannot be used here because this will normalize to the noise introduced in the simulations. Two fitting parameters are used, the lateral and the axial standard deviation of the Gaussian profile.

The performance measure used here is the relative squared error (RSE) (Zhang et al., 2007):

$$RSE_{gauss} = \frac{\|g_f - f_d\|^2}{\|f_d\|^2} \quad (3.38)$$

where f_d is the deconvolved image and g_f is the fitted Gaussian profile. RSE_{gauss} will show how well a Gaussian profile can be fitted to the deconvolved image.

We have repeated this simulation 300 times with a different noise realization for every instance.

3.4.3 Results

In figure 3.13 we see the results after fitting the Gaussian to the deconvolved image. The mean RSE is 1.3% with a standard deviation of 0.5%. In figure

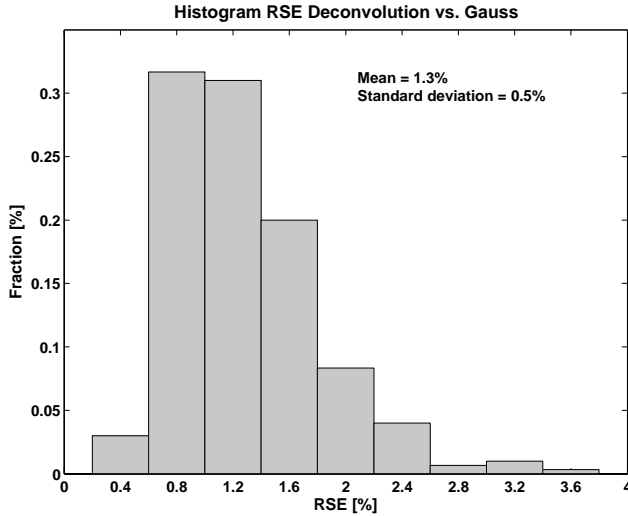


Figure 3.13: Histogram showing the distribution of RSE_{gauss} . 300 simulations have been performed with different noise realizations.

3.14 we see an example how well the deconvolved image fits the object and the Gaussian profile fits the deconvolved image.

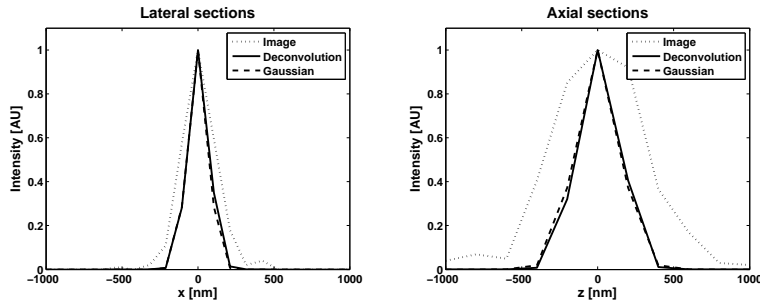


Figure 3.14: Sections through the middle of the simulated image, the deconvolved image and the Gaussian profile fit. Left: lateral sections, right: axial sections.

3.4.4 Conclusions

The result of $RSE = 1.3\%$ is comparable to results from (Zhang et al., 2007), where the conclusion is made that some PSFs are close approximations of 3D Gaussian profiles. Therefore we conclude that that deconvolved wide-field images of small fluorescent objects can also be approximated by a Gaussian profile. This result is not surprising, since the effect of the regularization in the MAPPG algorithm is smoothing of the data.

This result will be used in section 4.2.2 where a Gaussian scale space method is used to segment fluorescently labeled components in the cell nucleus.

3.5 Conclusions and discussion

This chapter deals with image restoration. Several methods of deconvolution have been explained including the Tikhonov-Miller filter, linear restoration filter, and MAPPG, an iterative algorithm, capable of super-resolution. A poor-man's confocal microscope has been introduced where no pinhole in the detection path is needed, together with a restoration scheme which permits the pinholes to be closer together and therefore has a 16 fold increase in scanning speed. Finally we show that, when dealing with small objects, deconvolved images can be approximated by a 3D Gaussian profile.

Three-dimensional organization of telomeres

4.1 Introduction

Telomeres are the repetitive sequences of DNA at the ends of the chromosomes. When the DNA is being synthesized in the S phase of the cell cycle, the ends of the DNA strand will not be fully copied. To prevent valuable genomic information being lost, the ends of the chromosomes have a buffer of repeating base pairs without any genes. These repeating parts (TTAGGG in mouse and in humans) are called the telomeres. A review of the significance of studying the spatial distribution of telomeres in the cell nucleus can be found in (Mai and Garini, 2006).

This chapter will focus on the spatial distribution of telomeres in the cell nucleus. We will present two methods of segmentation in section 4.2. Using the spatial coordinates of the found telomere signals, a parameter, ρ_T , is defined to characterize the spatial distribution of the telomeres during cell cycle in section 4.3 and a statistical correction method in section 4.4. These algorithms have been bundled in TeloView, a program initially aimed for analysis of telomere signals, in section 4.5. The results of the measurements with TeloView of ρ_T will be shown in section 4.6. Parts of this chapter have been previously published in BMC Biology (Chuang et al., 2004), Proceedings of SPIE (Vermolen et al., 2005b), Cytometry Part A (Vermolen et al., 2005a, 2008).

4.1.1 Cell Preparation

We have studied a mouse B lymphocyte cell nuclei population. The immortalized cells were sorted according to their DNA content for the determination of G0/G1, S or G2 phase. Cell cycle fractions were quantified through fluorescent-activated cell sorting analysis (Chuang et al., 2004). Flow analyses were performed on an EPICS AltraTM cytometer operating under MulticycleTM software (Beckman-Coulter, France). Approximately 10-15 nuclei from each phase were analyzed for this study, representing a total of 35 cell nuclei.

To further study the phase transition timing along the cell cycle, we used the synchronous bromodeoxyuridine (BrdU) sorting method (Chuang et al., 2004). The mouse B lymphocytes were labeled *in vivo* with BrdU. All BrdU-positive cells (i.e. cells in S phase, replicating their DNA) were live sorted and placed into culture. Populations of nuclei were then harvested at different times (3, 3.5, 4.5, 5.5, 6.5, 7.5, 8, 8.5 and 9.5 hours) of which approximately 20 nuclei were analyzed, representing a total of 180 cell nuclei.

For measurements of the telomeric disk the cells were first fixed and then telomere fluorescence *in situ* hybridization (FISH) was performed as described in Figueroa et al. (2000) using a Cy3-labeled PNA probe (DAKO, Glostrup, Denmark). DAPI was used as a DNA-specific counterstain. Telomere hybridizations were specific and we verified the correct number of telomeric signals observed at the ends of chromosomes prepared from primary cells using 2D FISH metaphase spreads. The lymphocytes were fixed in such a way that the 3D structure of the nuclei was conserved (Chuang et al., 2004).

4.1.2 3D Image Acquisition

For analysis of the telomere distribution, images were acquired with a Zeiss Axioplan 2 with a cooled AxioCam HR CCD in combination with a PlanApo 63x/1.4 oil immersion objective (Zeiss). This gives a pixel (sampling) distance in the lateral plane of $\Delta x = \Delta y = 106$ nm. The axial sampling distance between the planes was $\Delta z = 200$ nm. The point spread function (PSF) of the objective, which determines the optical resolution, gave a Full Width at Half Maximum (FWHM) of approximately $FWHM = 200$ nm in the lateral direction and 400 nm in the axial direction. Typical image size was 200 x 200 x 100 pixels. Table 4.1 gives a summary of these values for this imaging system. Figure 4.1 illustrates the system resolution. An image of a pair of telomeres relatively far apart and an image of a pair close together is shown. It is clear that the telomeres at a distance of 1200 nm can be easily distinguished and telomeres at a distance of 400 nm are just barely separable.

4.1.3 3D Image Processing

The 3D digital images were processed to improve the resolution using a constrained iterative maximum-likelihood deconvolution (Schaefer et al., 2001) which is available in the AxioVision 3.1 (Zeiss) software. This deconvolution method was chosen for this work because it has been shown to provide the best results (Verveer et al., 1999).

Table 4.1: Characteristics of the microscope system

$\text{FWHM}_{\text{lateral}}$	200 nm
$\text{FWHM}_{\text{axial}}$	400 nm
Δx	106 nm
Δy	106 nm
Δz	200 nm
M	63x
NA	1.4
Filters	DAPI, Cy3
Typical image size	200 x 200 x 100

4.2 Segmentation of telomere signals

To localize the telomeres inside the cell nucleus we can make use of different segmentation algorithms. The first uses a TopHat transform to remove some of the shading (varying background signal) present in the images. The second is a scale space method which enhances spot signals involving both size and signal strength. Both algorithms include a thresholding step for segmentation after which the center of mass is calculated to obtain the position of the telomeric signal.

4.2.1 TopHat segmentation

Before starting the segmentation we pre-process the data by smoothing with a 3D Gaussian kernel. Figure 4.2 shows how the data are transformed during the different steps of segmentation. For segmentation of the individual signals we have chosen an algorithm based on a morphological TopHat transformation (Meyer, 1979; Meyer and Beucher, 1990). The TopHat transform on an image A with structuring element B is defined as follows (Young et al., 1998). To find objects with high intensity ("light" objects):

$$\text{TopHat}(A, B) = A - \max_B(\min_B(A)) \quad (4.1)$$

The "structuring element", B , can be a quite general three-dimensional, gray-value object but in our case we have chosen for the simple case that B is spherical. The size of B should be bigger than the objects that are being sought but smaller than any shading in the background. For a gray-scale image

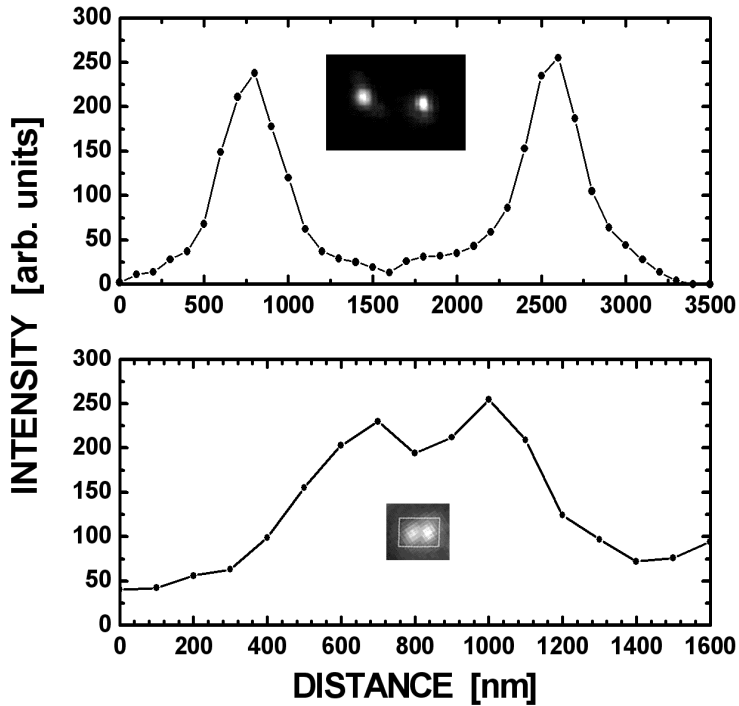


Figure 4.1: Demonstration of the spatial resolution of our measurements, Two pairs of telomeres are shown: 1200 nm apart (top), which can be easily separated, and 400 nm apart (bottom). The inserts show the original image and the graphs a section through the telomeres.

of telomeres, the telomeres would be our objects and any non-specific binding of Cy3 uniformly spread over the nucleus gives us shading. Thus, for our case, this translates to a spherical B with radius of 742 nm (7 pixels). After the TopHat transform the resulting image is thresholded with a user chosen value to produce a binary mask. To eliminate noise spikes that may still remain, we conclude with an erosion with a structuring element of 318 nm (3 pixels). This algorithm gives satisfying results for small telomeres. Using the binary image mask from the segmentation, the center of gravity of each dot is found. This gives coordinates (x_i, y_i, z_i) for each individual dot, where i is the index number of the dot.

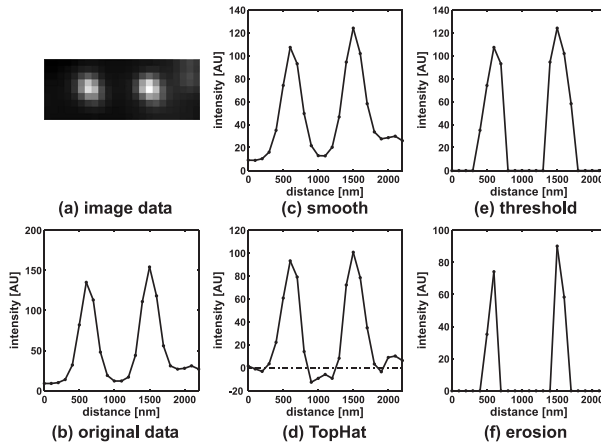


Figure 4.2: Working of the algorithm. First we see the raw "image data". A line through the center of this image gives a line section seen in "original data". After we "smooth", we perform a "TopHat" transform. Note that shading is now removed. We "threshold" and end up with two spots. One last "erosion" is performed to make sure that there are no remaining noise spikes.

4.2.2 Scale Space segmentation

To segment the probe signal of interest in the image a derivative scale-space method has been chosen. In (Chuang et al., 2004; Vermolen et al., 2005a) we have suggested using the morphological TopHat transformation (Meyer, 1979) to segment labeled telomeres in the mouse lymphocytes. Although this algorithm gave satisfactory results we chose to implement a new and faster algorithm and compared it to the TopHat method. This method is based on a robust method developed by Olivo-Marín (2002) where spots in a highly variable and noisy background can be segmented. The kernel used in (Olivo-Marín, 2002) is $[1/16, 1/4, 3/8, 1/4, 1/16]$, which is an approximation of the B-spline function and also an approximation of the 1D Gaussian with standard deviation $\sigma = 1$. We therefore propose to adjust this method in order to find objects that resemble 3D Gaussian intensity profiles of spots with a lateral size around 200 nm, as described below. This choice has been made because the signals in the nucleus are smaller than the optical resolution of the microscope system, and therefore the intensity profiles resemble the point spread function (PSF). The 3D Gaussian is an appropriate approximation of the 3D confocal PSF (Zhang et al., 2007) and it is also an approximation of deconvolved images of small fluorescent spots acquired by wide-field imaging as shown in section 3.4. Furthermore, the 3D Gaussian has a number of the same features as the

proposed à trous wavelet algorithm in (Olivo-Marin, 2002): it is translation invariant, the images after convolution with the 3D Gaussian are correlated and the implementation is fairly simple. The feature that it needs to be isotropic is let go, since the 3D PSF is anisotropic. The algorithm is implemented using 3D Gaussian profiles with different widths characterized by the standard deviation, σ , of the Gaussian function. In the axial (z) direction the width is three times larger than that in the lateral (x, y) direction because of the fundamental anisotropy in the 3D PSF. The PSF is longer in the axial direction than in the lateral direction. The image, g , is now convolved with Gaussian profiles with different widths to produce a Gaussian scale space of the image:

$$g_i = g \otimes G(\sigma_i) \quad (4.2)$$

with $i = 0 \dots 2$ and where \otimes is the convolution operator, G is the Gaussian profile with width σ_i in the lateral direction and $3\sigma_i$ in the axial direction. The factor 3 corresponds to the typical ratio of axial to lateral dimensions in confocal microscopy:

$$G(\sigma_i) = \frac{1}{3\sigma_i^3(2\pi)^{\frac{3}{2}}} \exp\left(-\frac{1}{2}\left(\frac{x^2}{\sigma_i^2} + \frac{y^2}{\sigma_i^2} + \frac{z^2}{9\sigma_i^2}\right)\right) \quad (4.3)$$

Next we choose a scale *base* to define the different widths:

$$\sigma_i = base * \sqrt{2^i} \quad (4.4)$$

with *base* \approx 100 nm, so we are looking for spots of size \approx 200 nm, which is approximately the full width at half maximum of a confocal PSF. After multiplying the differences in the Gaussian scale space, we produce the result:

$$g_{product} = (g - g_0)(g_0 - g_1)(g_1 - g_2) \quad (4.5)$$

For further noise reduction we convolve $g_{product}$ with a 3D Gaussian profile ($\sigma = 1$ pixel). This resulting image is thresholded at a value, T :

$$g_{bin} = \begin{cases} 1 & g_{product} > T \\ 0 & g_{product} \leq T \end{cases} \quad (4.6)$$

We propose to define the threshold T by treating the high intensity values in $g_{product}$ as outliers. This means we will define T using the mean, μ , and the standard deviation, σ , of the intensity values of $g_{product}$:

$$T = \mu + 3\sigma \quad (4.7)$$

In most cases this gives a satisfactory result, indicating that the signal-to-noise ratio is sufficient for accurate segmentation of the probe. Otherwise the user

can alter this threshold level. The result is a binary mask, g_{bin} , with objects representing probe locations. We compute the center of gravity of intensities for every object in the resulting mask to estimate the center of gravity of intensities for the n^{th} probe signal. This spot detection and localization algorithm has been embedded in TeloView (Vermolen et al., 2005a) (see section 4.5), which further offers the operator the ability to visually check the localization results within a matter of seconds, and manually add or remove the coordinates of probe signals if needed. This includes separation of touching objects.

4.2.3 Contrast enhancement of the TopHat and Scale Space method

Introduction

Both segmentation algorithms involve a contrast enhancement followed by a simple threshold. Therefore to test the methods we chose to see how well they enhance the contrast.

Methods

Figure 4.3 gives a definition of the contrast. We can define two intensity levels,

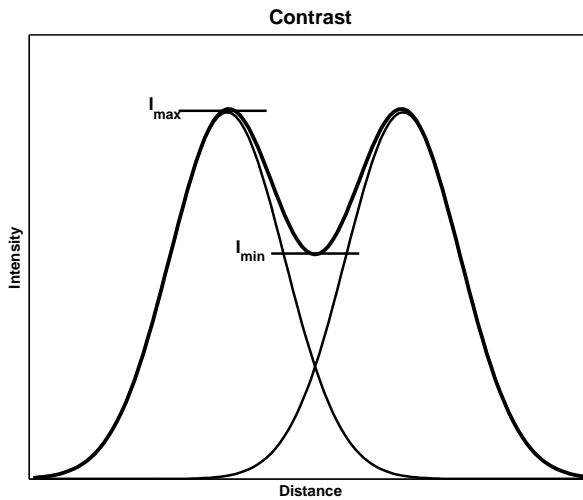


Figure 4.3: The contrast is defined as the ratio of $\frac{I_{max} - I_{min}}{I_{max}}$

I_{max} and I_{min} . The intensity I_{max} is the intensity at the position of the peak

of one of the spots. Note that this does not have to be the intensity of a peak of one spot alone, since we add intensities of the other neighboring spots. The intensity, I_{min} , is the intensity in the middle of the peak positions of the two spots. Now we can define the contrast, c , as:

$$c = \frac{I_{max} - I_{min}}{I_{max}} \quad (4.8)$$

If the spots come close together I_{min} will be larger than I_{max} and consequently $c < 0$.

We have simulated images, g , of two fluorescent spots, f , by modeling them as small sphere-like objects convolved by a Gaussian profile, G , after which we introduce a background, b , and some Poisson noise, $N(\cdot)$:

$$g = N(G \otimes f + b) \quad (4.9)$$

The Gaussian profile has a standard deviation of $\sigma_r = 1$ pixel in the lateral direction and $\sigma_z = 3$ pixels in the axial direction. With a given radius, r , of the spots we chose a random position of the two spots with distance d , which is varied. We have measured the contrast before and after the two methods. The size of the structuring element in equation 4.1 in the TopHat method is 2 pixels and the size of the *base* from equation 4.4 is 1 pixel. This gave the best results for the smallest sized spots we chose (1 pixel³ which corresponds to $r = 0.62$ pixels). By keeping these scale parameters constant and increasing the size of the spots we can see where the algorithms break down, i.e. there is no improved contrast.

Results

In figure 4.4 we can see the results of the contrast enhancements of the TopHat algorithm and of the scale space algorithm. We have performed the simulation 100 times for every spot size. Then we ordered the measured contrasts before enhancement and plotted these together with the results from the TopHat and scale space methods. Note that it is possible for the contrast to be negative when the spots are in close vicinity. In figure 4.4a we see the results for spots with $r = 0.62$ pixels. We have used a Wilcoxon rank sum test to test the null-hypothesis that the median of the differences of the two methods gives zero. The results are shown in table 4.2. For such small spots there is no statistical reason that this median is zero. In other words, looking at individual measurements, no method is preferred. The spread in the contrast in the TopHat method is clearly larger than in the scale space method. In figure 4.4b we see the results for spots with $r = 1.7$ pixels. Using the same statistic we can say there is a clear difference between the two methods. Again the spread in the TopHat method is higher. We sometimes see that the TopHat has a lower contrast than the

r	m(TopHat-Original) p(TopHat,original)	m(Scale space-original) p(Scale space,original)	m(Scale Space-TopHat) p(Scale space,TopHat)
0.62	0.1 4e-10	0.1 3e-11	0.01 0.1
0.78	0.1 4e-11	0.1 2e-11	0.02 0.2
1.1	0.1 2e-11	0.2 2e-12	0.02 4e-3
1.3	0.09 1e-10	0.10 5e-11	0.01 0.4
1.7	0.07 7e-9	0.1 7e-13	0.03 1e-6
2.3	0.04 2e-3	0.2 6e-18	0.09 8e-14
2.9	0.03 4e-3	0.2 3e-17	0.09 7e-14
3.6	0.02 0.5	0.2 2e-17	0.2 1e-14
4.9	-0.08 6e-4	0.2 4e-18	0.3 5e-16
6.2	-0.2 2e-5	0.2 2e-16	0.3 3e-16
7.8	-0.04 2e-3	0.3 2e-13	0.4 2e-12
11	-0.09 7e-5	0.4 2e-3	0.5 3e-5

Table 4.2: The upper values m is the median value of the differences of the paired outcomes, where the original contrast > 0 . The lower values are the p-values of the Wilcoxon Rank Sum test giving the chance that these medians are zero.

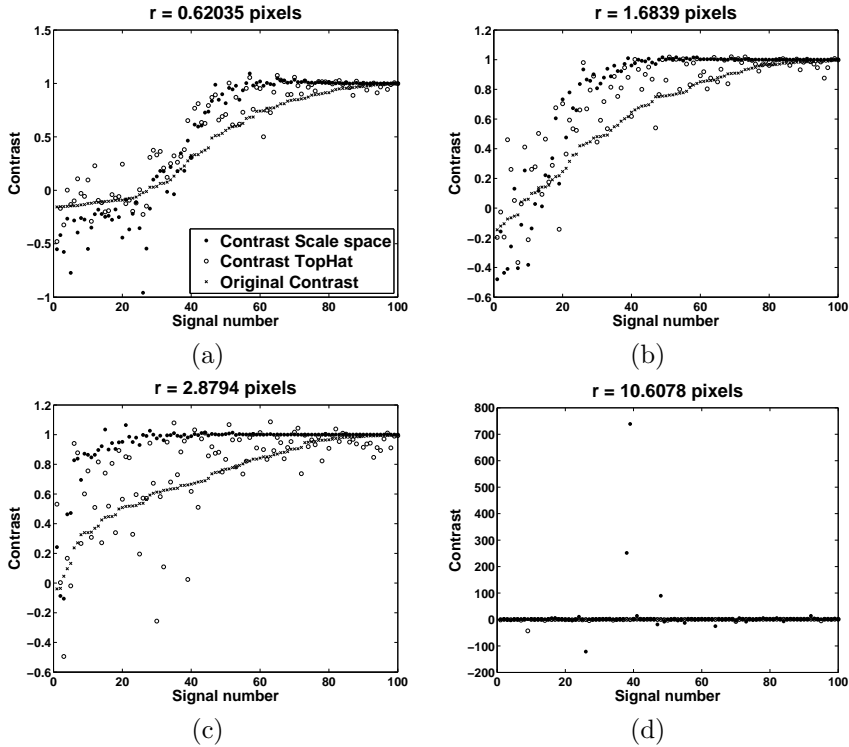


Figure 4.4: Here we show the results of the two contrast enhancement methods. In (a) we see that both methods improve the contrast and the difference between the Scale space method is not big. In (b) we see that the Scale space method performs better than the TopHat method. In (c) the TopHat method begins to lose its enhancement properties. In (d) the spots are so big that both methods lose their contrast enhancement properties.

original contrast even for higher starting contrasts. It should be noted that the original contrast is measured before adding the noise. So this result could be a result from the noise. Nevertheless, the scale space method is never smaller than the original contrast when the original contrast is high enough (approximately > 0.2). In figure 4.4c we see the results for spots with $r = 2.9$ pixels. Here we see that the TopHat method shows no improvement in contrast anymore. If we even make the spot size larger, like in figure 4.4d with spots with $r = 11$, we see that the Scale space method behaves even more unpredictably.

Conclusions

In this section we show that both the TopHat and the Gaussian Scale space method enhance the contrast of two spots lying in close vicinity as long as the spots are not too large. For small spots both the TopHat and the Scale space method show similar results, although the Scale Space method seems to have a smaller statistical variation. So it is easier to find a proper threshold for the Scale space method than for the TopHat method. If we leave the scale of the methods constant we see that the TopHat loses its enhancement properties faster than the Scale space algorithm with increasing spots sizes. So for images with small and large signals the Scale space method is preferable.

4.3 Characterization of the structure

Observing the organization of telomeres in many cells, we see that the envelope shape of the telomeres is usually a spheroid, as illustrated in figure 4.5. A

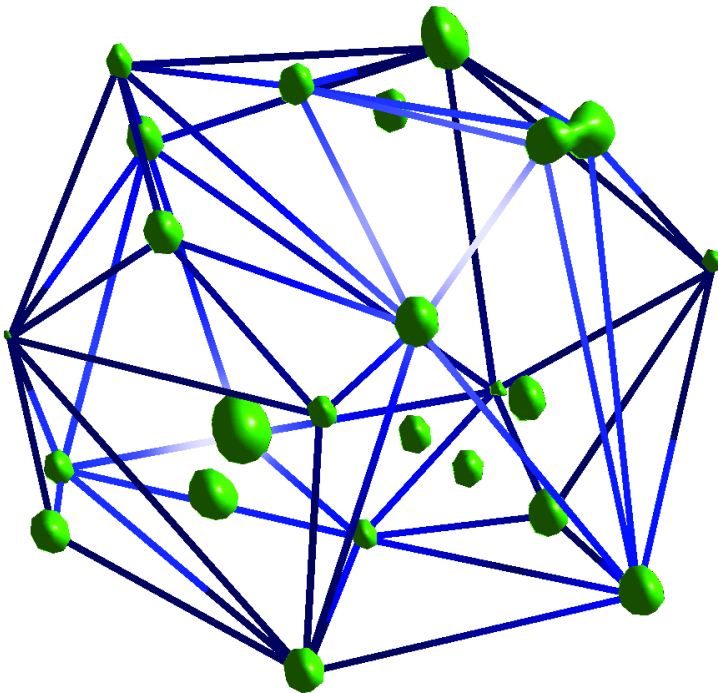


Figure 4.5: The telomeric territory can be given by a convex body containing all the telomeres. In most cases this envelope can be approximated by a geometric figure called a spheroid. Figure courtesy of Yuval Garini.

spheroid is a geometric figure, like an ellipsoid, where the two main axes have equal length, $a = b$ and the third axis has a different length, c . This is shown in figure 4.6. If $a = c$ we have a sphere, if $a < c$ we have a prolate spheroid

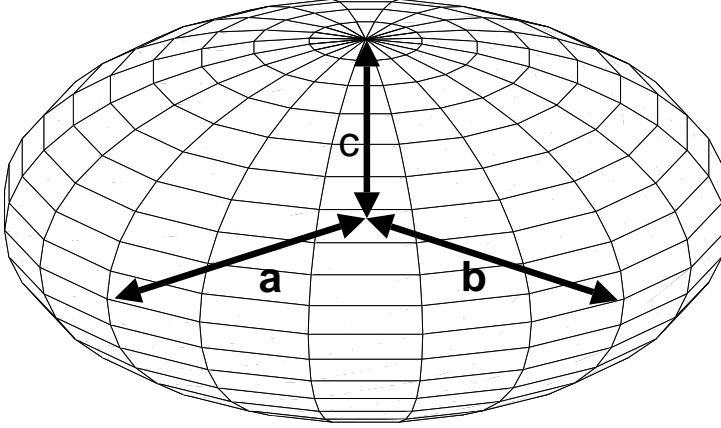


Figure 4.6: The telomeric territory is characterized as an oblate spheroid, where two of the main axes, a and b , are of equal length and the third main axis, c , is shorter. The ratio $\rho_T = \frac{a}{c}$ now gives a measure of the flatness of the spheroid.

and if $a > c$ we have an oblate spheroid. We can, therefore, define a telomere ratio parameter, ρ_T , which gives us a measure of the disk-like nature of this organization, given by:

$$\rho_T = \frac{a}{c} \quad (4.10)$$

If $\rho_T \approx 1$ then the telomeres are distributed in a spherical way within the cell. If, however, $\rho_T > 1$ then the telomeric territory is more disk-like. In the following, we describe how we determine ρ_T . Given the spatial coordinates of every spot $(x_i, y_i, z_i | i = 1, 2, \dots, N)$, we translate the original spatial coordinates (x, y, z) to a new orthogonal coordinate system such that the origin of the new coordinate system is in the center of the spots and rotated such that the distance from the spots to the new axes is maximized. This procedure is known as a principal component analysis (Wall et al., 2003). To accomplish this we calculate the singular values (eigenvalues) of the covariance matrix of the data points. The three singular values, $\lambda_1 \geq \lambda_2 \geq \lambda_3$, are real, positive and can be ordered. They are the variances of the distances from the spots to the new principal axes. The standard deviation for each new axis is then given by:

$$\sigma_i = \sqrt{\lambda_i} \quad (4.11)$$

From these standard deviations we then define the dimensionless ρ_T as:

$$\rho_T = \frac{\sqrt{\sigma_1\sigma_2}}{\sigma_3} \quad (4.12)$$

That is, the geometric mean $\sqrt{\sigma_1\sigma_2}$ is taken as the value for a and σ_3 is the value for c . Given that we work with ordered λ 's we have:

$$\rho_T \geq 1 \quad (4.13)$$

4.4 Correction of ρ_T by model fitting

For an infinite number of spots in a spheroid, the parameter, ρ_T , would give us the ratio of the length of the principal axes: $\frac{a}{c}$. Because we have a finite number of spots, N , this does not hold anymore. We have done Monte-Carlo simulations to see what the effect is on the observed $\rho_{T,o}$ with respect to the real $\rho_{T,r}$ and N .

For this we used MatLab to generate a set of uniformly distributed pseudo-random numbers (x, y, z) in the interval $(-1.0, 1.0)$. Then we calculate the squared distance to the center of the sphere

$$r^2 = x^2 + y^2 + (\rho_{T,r} \cdot z)^2. \quad (4.14)$$

Here $\rho_{T,r}$ scales the spheroid to a sphere. If

$$r^2 \leq 1, \quad (4.15)$$

we accept the point, because it is inside the spheroid. This process is repeated until N points are accepted. From this set of coordinates, (x_i, y_i, z_i) , $i = 1 \dots N$, we can compute $\rho_{T,o}$. For every $\rho_{T,r}$ we compute 10000 values of $\rho_{T,o}$. This gives us the probability distribution, $p(\rho_{T,o}|\rho_{T,r})$, for a given N . Using Bayes' rule we can now obtain the distribution, $p(\rho_{T,r}|\rho_{T,o})$, for a given N :

$$p(\rho_{T,r}|\rho_{T,o}) = \frac{p(\rho_{T,r})p(\rho_{T,o}|\rho_{T,r})}{p(\rho_{T,o})}. \quad (4.16)$$

Because no information is known about the a-priori probability we assume, for practical reasons, $p(\rho_{T,r})$ to be uniform. The $\rho_{T,r}$ which gives us the maximum of $p(\rho_{T,r}|\rho_{T,o})$ is the maximum likelihood estimator, $\hat{\rho}_{T,r}$. In figure 4.7 we can see $\hat{\rho}_{T,r}$ plotted against $\rho_{T,o}$ for $N = 40$.

The next step is to model a curve for a given N . This is done by cutting the curve in two:

$$\begin{aligned} \widehat{\rho}_{T,r} &= 1 && \text{for } \rho_{T,o} < d, \\ \widehat{\rho}_{T,r} &= \rho_{T,o} - \frac{a^c(d-1)}{(\rho_{T,o}-b)^c} && \text{for } \rho_{T,o} \geq d. \end{aligned} \quad (4.17)$$

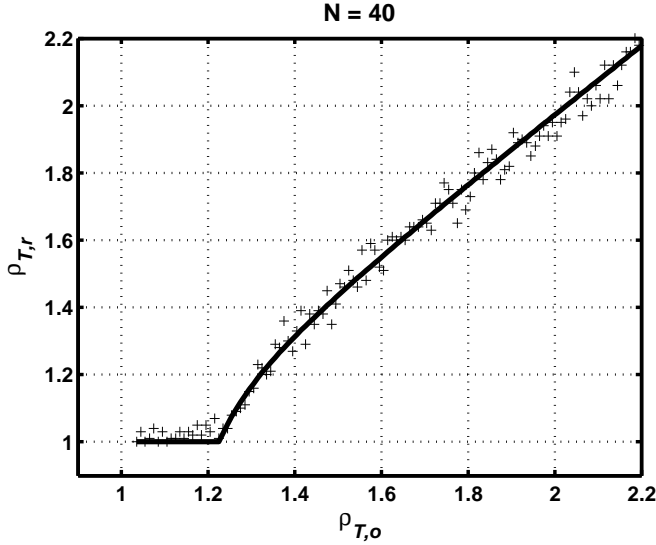


Figure 4.7: Figure showing maximum likelihood estimators $\hat{\rho}_{T,r}$ plotted against $\rho_{T,o}$ (pluses) and the fitted curve (line).

Here a, b, c and d are the model parameters, where b is dependent on d and a :

$$b = d - a, \quad (4.18)$$

to make the function continuous. Now we can model the independent parameters a, c and d as a function of N :

$$\begin{aligned} a &= \gamma_1, \\ c &= \gamma_2 N + \gamma_3, \\ d &= \frac{\gamma_4}{N^{\gamma_5}} + 1. \end{aligned} \quad (4.19)$$

This gives us the fitting parameters, γ_i ($i = 1 \dots 5$), for our model. Next, we fit the model to our data points using a least squares approach, i.e. we minimize the error:

$$\varepsilon = \sum_{\rho_{T,o}, N} (\widehat{\hat{\rho}}_{T,r}(\gamma_i) - \hat{\rho}_{T,r})^2, \quad (4.20)$$

which gives us γ_i . In figure 4.7 we see the result of the model fitting for $N = 40$. Using this result we can correct our estimate of $\rho_{T,o}$ for a finite sample size N .

Table 4.3: Results of phase sorted cells.

Phase	Before correction		After correction	
	Mean ρ_T	Stand. dev. ρ_T	Mean ρ_T	Stand. dev. ρ_T
G0/G1	1.4	0.2	1.03	0.10
S	1.5	0.3	1.02	0.06
G2	14	3	13	3

4.5 TeloView

Image segmentation and analysis of deconvolved 3D images of cells with labeled telomeres have been performed with a sequence of procedures that we have bundled together and named TeloView. The procedures themselves are from our image software library DIPIImage which is available as public domain software at <http://www.DIPIlib.org/>. The version of DIPIImage used in this development operates under MatLab (The MathWorks, Natick, MA, USA).

TeloView loads the 3D image and displays a maximum projection along the three main optical axes. While thresholds and other parameters can be adjusted for display purposes, the analysis is performed on the original 3D data. After segmentation, the 2D display indicates the location of the automatically found spots for verification. At this point the user can decide to remove falsely labeled spots or add spots that were not found. A screenshot of the user interface is shown in figure 4.8.

4.6 Organization during the cell cycle in mouse lymphocytes

Results of the analysis of the cell-sorted mouse lymphocytes before and after the correction are presented in table 4.3. The values of ρ_T are somewhat smaller after correction. Here we see small values (close to 1) of ρ_T for nuclei in G0/G1 and S phases, which indicates that the telomeres are distributed throughout the cell in a spherical like structure. For the telomeres in G2, however, there is a high value of ρ_T , indicating that the telomeres form a disk. A statistical analysis, using a two-sample Student's t test with unequal variances, indicates a significant difference in ρ_T between G0/G1 and G2 phases ($P < 1e-6$) and between S and G2 phases ($P < 1e-6$).

The results of the BrdU synchronization experiment can be seen in figure 4.9. In the left graph we see the results of nuclei counted by a human observer. The observer was presented with a 2D computer display of the 3D distribution. A display of the DAPI counterstain indicated the position of the total DNA. In this graph we see the fraction of nuclei with the telomeres in

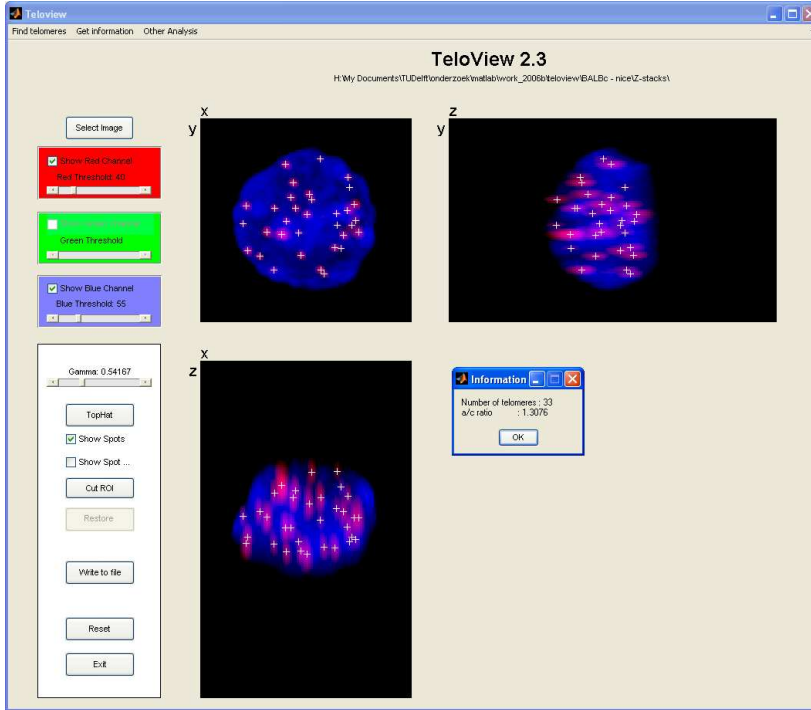


Figure 4.8: Screenshot of the user interface of TeloView. The screen shows the three displays with maximum intensity projections along the three main optical axes. It also shows crosses at the locations where the software identified a telomere. After automatic identification the user can interactively add or remove crosses.

a disk. At 3.5 h, 90% of the nuclei show a telomeric disk. Based on timing since S phase, most nuclei are believed to be in late G2. After this point, cells continue through the cell cycle, enter into prometaphase and metaphase (i.e. mitosis), and the number of cells in G2, accordingly, decreases. This correlates with the observation that the fraction of cells with a telomeric disk decreases.

In the right graph of figure 4.9 we show the results of ρ_T calculations on the same population of nuclei. The right graph however, does not correspond exactly to the left graph calculated by the observer, because it calculates the average ρ_T value of the complete population of nuclei at that time point; the nuclei can be in different cell-phases. By using a threshold on the ρ_T value, it is possible to imitate the classification of nuclei in a disk. If we choose a threshold of 6.7 between nuclei in a disk ($\rho_T > 6.7$) and others, we can calculate the fraction of these nuclei and get approximately the same curve as the human observer got. Apparently this is the subjective threshold that was

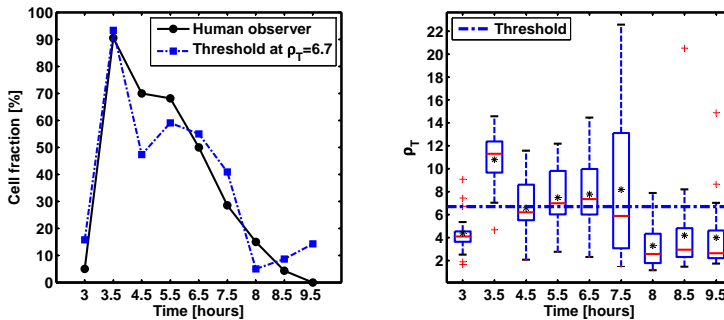


Figure 4.9: Results of synchronous BrdU sorting experiment. In the left graph we show the results obtained by a human observer (black line with circles). For each time point approximately 20 nuclei were analyzed and the fraction of nuclei with a telomeric disk was plotted. In the right graph we show a boxplot of ρ_T calculations on the same population. The asterisks give the mean ρ_T at every time point and the boxes and whiskers give the 0th, 25th, 50th, 75th and 100th percentile of the measurement. The plus-signs denote outliers. The blue line in the left graph shows the fraction of nuclei with $\rho_T > 6.7$.

selected when the left graph of figure 4.9 was created.

In the boxplot in figure 4.9 we also see outliers which are easily explained if the data within the box and whiskers are from the population with low ρ_T and the outliers are from the population with high ρ_T . The outliers in figure 4.9 at $t = 8.5$ hours, for example, are due to the last few cells from the G2 population that have not yet entered mitosis.

4.7 Conclusions and discussion

In this chapter we have presented two methods to segment signals of fluorescently labeled telomeres in mouse lymphocytes. First we have discussed the TopHat method. Second we have adapted the method introduced by [Olivo-Marin \(2002\)](#), which was initially a 2D wavelet method. We have adapted the method for 3D and replaced the wavelet by the computationally more favorable Gaussian profile. We have compared these methods with respect to their ability to enhance the contrast of small spots in a 3D image. The scale space method gives more stable results and is also more suitable for larger signals. Following the localization of the telomeres we have defined a parameter ρ_T . This parameter measures if the spatial distribution of the telomeres is sphere-like ($\rho_T \approx 1$) or disk-like ($\rho_T > 1$). We introduced a statistical correction, correcting for the fact that we do not have an infinite number of signals. These tools have been implemented in TeloView. We have used TeloView to study mouse lymphocytes during the cell cycle. First we have cell sorted nuclei for

the different phases. We found that the telomeres in G0/G1 phase and S phase have a more sphere-like volume. We emphasize that this does not mean that the telomeres are randomly situated in the cell nucleus. In late G2 phase, before the chromosomes have condensed, the spatial distribution of the telomeres changes into a disk-like volume. A BrdU synchronization experiment has given more evidence for this disk-like structure in G2. A human observer classified the images of the cell nuclei into disk/no-disk. We can give a threshold after calculation of ρ_T giving a classification which correlates nicely with the human observer.

Because the next step in the cell cycle is mitosis, it could be that this ordering of the telomeres is a first ordering of the chromosomes into the equatorial plate.

Telomere and chromosome remodeling in the interphase nucleus

In (Louis et al., 2005b) we have studied the effect of topological remodeling of the nucleus after overexpression of c-Myc. We found that, deregulation cycles of telomeric aggregates appear directly proportional to the duration of the c-Myc. I will discuss a way to assess the relative length of a telomere, section 5.2, and a way to find aggregates, 5.2.2. Also chromosome overlap will be discussed in section 5.3. Parts of this chapter are based on (Louis et al., 2005b).

5.1 Introduction

Constitutive expression of c-Myc due to chromosomal translocations, mutation, or amplification contributes to the development and progression of many cancers (Nesbit et al., 1999; Potter and Marcu, 1997). c-Myc deregulation directly promotes genomic instability (Mai and Mushinski, 2003), causing locus-specific and karyotypic instability (Mai, 1994; Mai et al., 1996b,a; Felsher and Bishop, 1999a; Rockwood et al., 2002). Additionally, c-Myc induces illegitimate replication initiation (Kuschak et al., 2002; Louis et al., 2005a), DNA breakage (Vafa et al., 2002), alterations of DNA repair (Hironaka et al., 2003; Karlsson et al., 2003a), and a low level of point mutations (Mac Partlin et al., 2003; Chiang et al., 2003). Effects of c-Myc on genomic instability are reversible after a transient experimental activation of c-Myc (Mai et al., 1996b). However, c-Myc continues to generate instability after constitutive deregulation (Mai et al., 1996a). In vivo, c-Myc deregulation directly initiates and promotes tumorigenesis (Adams et al., 1985; Potter and Wiener, 1992; Pelengaris et al., 2002; Felsher and Bishop, 1999b; Marinkovic et al., 2004). When c-Myc deregulation is abolished, in vivo tumorigenesis is reversible, provided that no additional mutations had occurred (Felsher and Bishop, 1999b; Marinkovic et al., 2004; D’Cruz et al., 2001; Jain et al., 2002; Karlsson et al., 2003b; Shachaf et al., 2004). Prompted by the complexity of downstream genetic alterations that result from c-Myc deregulation, we investigated whether c-Myc affected the 3D

organization of the mammalian interphase nucleus and whether this remodeling had an impact on genomic stability. We show that c-Myc deregulation causes remodeling of the 3D nuclear organization of telomeres and chromosomes, thus creating the topological conditions that initiate genomic instability. In previous work (Chuang et al., 2004), we showed that telomeres of normal cells are organized within the 3D space of the interphase nucleus in a non-overlapping and cell cycle-dependent manner. This order is distorted in tumor cell nuclei where telomeres are found in close association forming aggregates of various numbers and sizes. In (Louis et al., 2005b) we show that c-Myc overexpression induces telomeric aggregations in the interphase nucleus. Directly proportional to the duration of c-Myc deregulation, we observe three or five cycles of telomeric aggregate formation in interphase nuclei. These cycles reflect the onset and propagation of breakage-bridge-fusion cycles that are initiated by end-to-end telomeric fusions of chromosomes. Subsequent to initial chromosomal breakages, new fusions follow and the breakage-bridge-fusion cycles continue. During this time, nonreciprocal translocations are generated. c-Myc-dependent remodeling of the organization of telomeres thus precedes the onset of genomic instability and subsequently leads to chromosomal rearrangements. Our findings reveal that c-Myc possesses the ability to structurally modify chromosomes through telomeric fusions, thereby reorganizing the genetic information.

This chapter will focus on two aspects of (Louis et al., 2005b).

1. Telomeric aggregates. These aggregates have been counted manually in this study. In this chapter we will propose an automatic method to measure the relative intensity of telomeric fluorescent signals and find outliers (aggregates).
2. Chromosome overlap. We have implemented a relatively simple algorithm to measure the volume overlap of two chromosome fluorescent signals in the cell nucleus.

5.2 Telomere length assessment and aggregates

5.2.1 Introduction

In (Louis et al., 2005b) aggregates are counted manually from a screen after thresholding and rendering of a isosurface of the 3D images. Although we believe that this can give a good indication of the increase in telomeric signal aggregation, we propose to use a new and automatic algorithm to define and find aggregates.

5.2.2 Methods

Telomere length

The integrated intensity is proportional to the size of the telomere because the size is proportional to the amount of fluorochrome that is attached to the telomere and therefore to the telomere length (Lansdorp et al., 1996). The binary mask, g_{bin} (as defined in section 4.2.2), is not suitable for calculating the intensities, because the objects in the mask do not cover the complete volume of voxels that include intensities coming from a telomere. A different approach, used here, is to first create a binary mask with the watershed algorithm (Verwer et al., 1993) of the image data, g , convolved with a Gaussian profile with $\sigma = 1$ pixel for noise reduction. The telomere coordinates (x_n, y_n, z_n) , determined in 4.2.2, tell us which objects in this mask are telomere regions. Simply integrating intensities in these regions will also give the wrong answer because background pixels are not excluded from these regions and will bias our calculations. Our solution is to calculate the integrated intensity in a region of interest with (x_n, y_n, z_n) as middle point within this mask resulting from the watershed. The region of interest is a small sphere, with radius r , convolved with a Gaussian profile with width $\sigma = 1$ pixel in the lateral and $\sigma = 3$ pixels in the axial direction, which results in an elongated sphere. We will call this region of interest, which is gray-scale, $sphere_{gray}$ and the region from the watershed, which is binary, we will call $mask$. The next binary region with which we work with is $sphere_{bin}$. This is a binary sphere with radius $r + 3\sigma$ (with $\sigma = 1$ or 3 pixels depending on the direction). Now we define the mean of the gray values of g at the coordinates where $mask$ has value one and $sphere_{bin}$ has value zero as our background level, b . Our signal image, g_{signal} , becomes:

$$g_{signal} = g(mask) - b \quad (5.1)$$

We normalize both $sphere_{gray}$ and g_{signal} for their maximum value and calculate their mean squared difference, ϵ_{new} , using $sphere_{gray}$ as a weighting function:

$$\epsilon_{new} = \frac{\sum_i sphere_{gray,i} (sphere_{gray,i} - g_{signal})^2}{\sum_i sphere_{gray,i}} \quad (5.2)$$

This weighted least squares function gave satisfactory results after a trial and error process using several least squares methods. The process starts with $r = 1$. First we rename ϵ_{new} :

$$\epsilon_{old} = \epsilon_{new} \quad (5.3)$$

Now we grow the region by using $r = r + 1$ for the next iteration and calculate ϵ_{new} again. The iterative process is stopped when

$$\epsilon_{new} > \epsilon_{old} \quad (5.4)$$

Table 5.1: Results of the intensity measurements.

Ground truth	Before processing		After processing			
	Mean	Std	SNR = 25		SNR = 100	
			Mean	Std	Mean	Std
1.600	1.577	0.004	1.543	0.007	1.526	0.006
2.700	2.677	0.004	2.613	0.009	2.560	0.007
3.840	3.832	0.003	3.86	0.01	3.803	0.007
5.625	5.617	0.004	5.78	0.05	5.468	0.04

The integrated intensity, I_n , for the n^{th} telomere is now

$$I_n = \sum g_{\text{signal}}(\text{sphere}_{\text{bin}}) \quad (5.5)$$

In figure 5.1 we show a flow chart of the algorithm.

Simulation

Given the simulation technique described in (Kempen, 1998), where it is explained how to simulate a ellipsoid-like object in an image, we have simulated an object with 16 fluorescent spots. In figure 5.2a we can see a section of the 3D image, we see 12 small spots (radius, $r = 1$ pixel) and four spots with different larger sizes (radius, $r = \{2, 3, 4, 5\}$ pixels). The relative integrated intensities are known and given in table 5.1. We also simulated the PSF according to Gibson and Lanni (1991) with a lateral sampling distance, $\delta r = 106$ nm, axial sampling distance, $\delta z = 200$ nm, wavelength, $\lambda = 550$ nm, magnification, $M = 63$, numerical aperture, $NA = 1.3$, and refractive index of the immersion oil, $n = 1.515$. After convolution of the object with the PSF we corrupt the image with Poisson noise and then deconvolve as described in section 3.3.3. To get some statistics we have repeated this process 100 times. In each instance all spots in the object have been given a random sub-pixel shift. We also repeated this experiment for two levels of noise, $SNR = \sqrt{N} = \{25, 100\}$, where N is the number of photons of the maximum in the image. In figure 5.2 we can see one realization of the simulated image and a restoration result.

We have chosen to show the relative integrated intensities. For every image, we have normalized the intensity of the four larger spots to the mean intensity of the 12 small spots. We measured these intensities before we do the convolution and deconvolution and after. The results of these measurement are given in table 5.1. In this table three main columns are present. The 'ground truth' is given by the simulation. The results of intensity measurements 'before processing', thus on figure 5.2a. And the results 'after processing', thus on figure

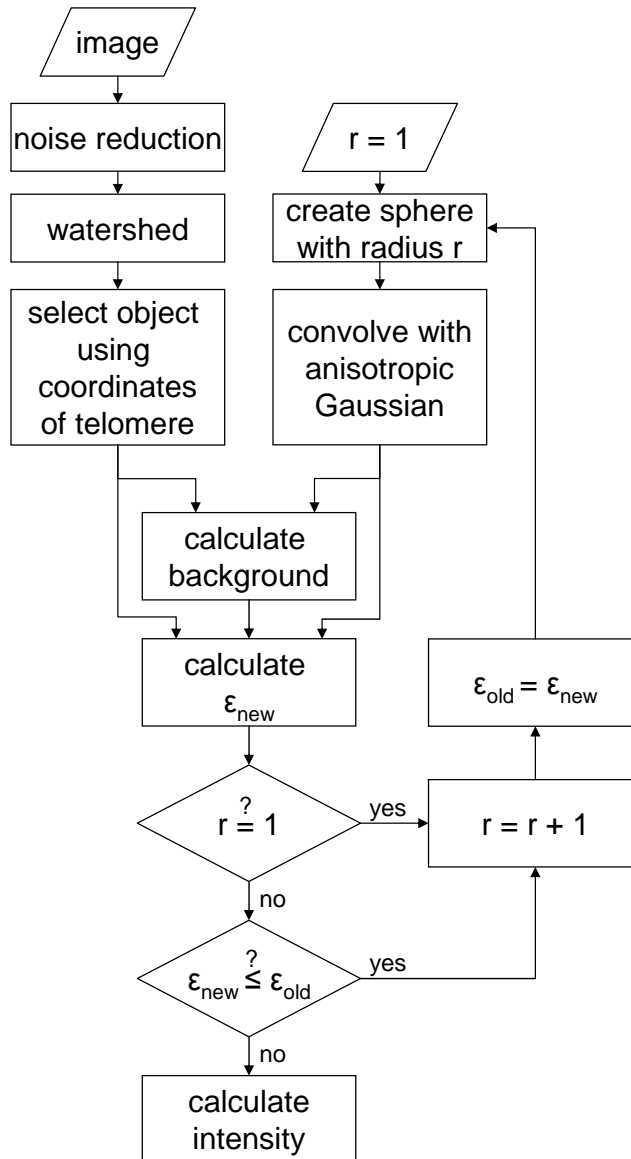


Figure 5.1: Flow chart showing the algorithm to calculate the integrated intensity of a telomere signal. The basic idea is to calculate the integrated intensity in a growing region of interest until no more intensity is added. The growing is confined by a mask created by a watershed.

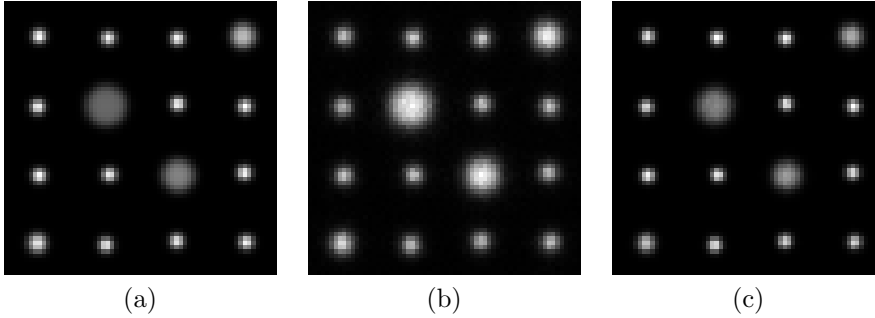


Figure 5.2: (a) Shows the simulated object. There are 12 small spots and four larger spots. (b) Shows the image of the object after convolution with the PSF and corruption with Poisson noise. (c) Shows the result of the restoration. These images are the middle lateral sections of a 64x64x64 pixel object. All images have been stretched linearly to give more contrast.

5.2c. We see that all results of the measurements fall within 5% of the ground truth. We therefore conclude that our method gives an accurate representation of the relative integrated intensities with a majority of small spots with some outlying larger spots.

Aggregates

Introduction To find aggregates of telomeres one has to first define an aggregate. Officially aggregation would be multiple telomeres clumping together. Since this would be below the resolution of the microscope, aggregates in TeloView are defined as signals with an unexpectedly high intensity. To find these outliers we have to choose what is normal. In TeloView two versions of normal intensities have been defined. First, we use intensities that show a linear function when ordered from small to large. This method will be explained in section 5.2.2. Second, we use intensities that show a distribution around one 'normal' intensity. This method is defined in section 5.2.2.

Line Method After calculating the intensities of the telomeres signals, TeloView orders the intensities from small to large. In figure 5.3 we see that we can draw a straight line through the signals with small intensities. We can also see that the two larger signals do not fall on this line. We have chosen to use robust statistics and weighted linear regression (Fox, 2002; Hampel et al., 1986) to find the line and the outliers (i.e. data not on the line). We start with an initial estimate of the line coefficients, a , with a least squares fit:

$$a = \frac{x^t y}{x^t x} \quad (5.6)$$

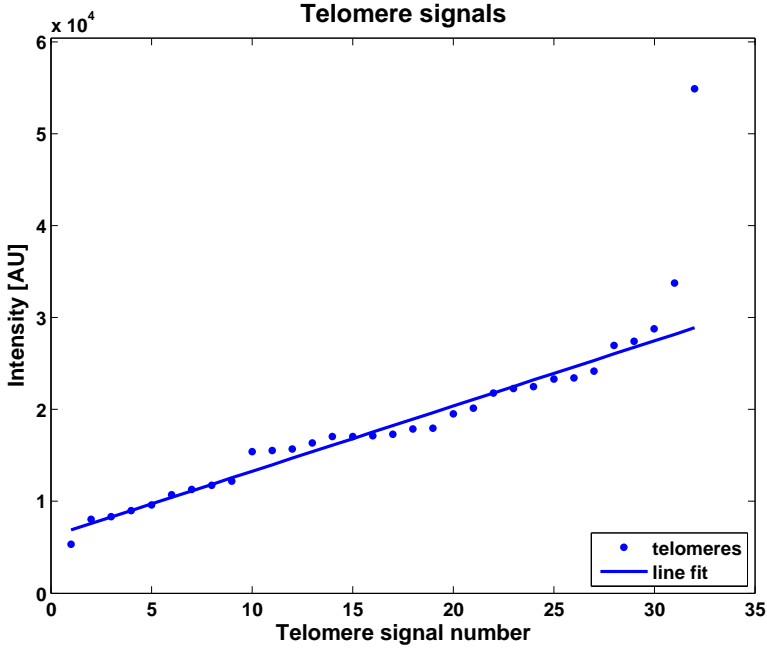


Figure 5.3: Graph showing the telomere signal intensities ordered from low to high. We can draw a straight line through the signals if we ignore the two highest signals.

Where, y , is the telomere signal intensity, x the ordered telomere signal number and $(\cdot)^t$ is the matrix transpose operation. We can calculate the residuals, r , from the data to the line:

$$r = y - xa \quad (5.7)$$

Now we calculate weights, w , for the *Huber M-estimator* and calculate a weighted least squares fit:

$$a = \frac{x^t w y}{x^t w x} \quad (5.8)$$

Now we repeat equations 5.7 and 5.8 until the line coefficient-vector a converges.

Now we calculate the *one-step M-estimator* (Hampel et al., 1986):

$$T_n = T_n^{(0)} + S_n \sum_{i=1}^n \psi\left(\frac{r_i - T_n^{(0)}}{S_n^{(0)}}\right) / \sum_{i=1}^n \psi'\left(\frac{r_i - T_n^{(0)}}{S_n^{(0)}}\right) \quad (5.9)$$

where ψ is the *Huber estimator* defined as:

$$\psi = \min(b, \max(r_i, b)) \quad (5.10)$$

with $b = 1.345$. For $T_n^{(0)}$ and S_n we take robust estimators:

$$T_n^{(0)} = \text{median}(r) \quad (5.11)$$

$$S_n = 1.483\text{MAD}(r) \quad (5.12)$$

where MAD is the median absolute deviation. Now we define two groups, *inliers* and *outliers* as:

$$x_i, y_i \in \begin{cases} \text{inliers} & \text{if } \frac{r_i - T_n}{S_n} \leq t \\ \text{outliers} & \text{if } \frac{r_i - T_n}{S_n} > t \end{cases} \quad (5.13)$$

where t is a threshold defined by the *student's-t* distribution with $p = 0.01$. Then we normalize the intensity signals to the mean intensity of the *inliers*. In figure 5.4 we see the result of the algorithm.

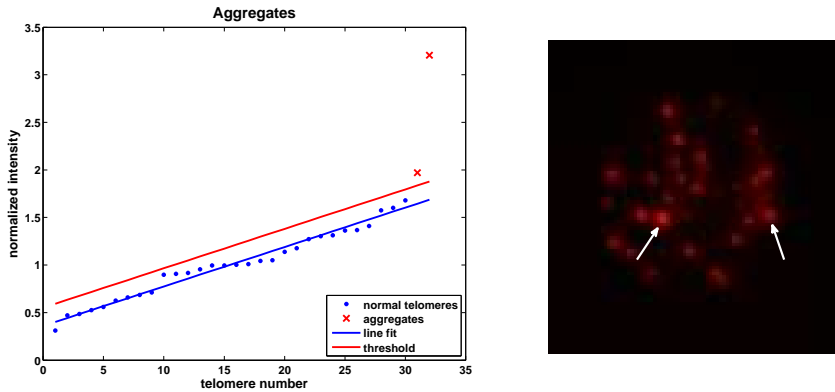


Figure 5.4: Left: graph showing the result of the 'line method'. Using robust linear regression we can estimate a line (blue line) through the telomere signal intensities. Using a threshold (red line) on the residuals we can define aggregates (red crosses) and normal sized telomeres (blue dots). Right: maximum intensity projection in the axial direction of the 3D image of the telomeres. The arrows indicate the found aggregates.

Normal Method The second method is based on the assumption of normality in the data. We start by calculating normalized intensities, $Z_{i,n}$, of sets

of increasing signal intensities:

$$Z_{i,n} = \frac{y_i - \mu_n}{\sigma_n} \quad i = 1:N, n = 2:N \quad (5.14)$$

where

$$\mu_n = \frac{\sum_{i=1}^n y_i}{n} \quad (5.15)$$

$$\text{and } \sigma_n = \sqrt{\frac{\sum_{i=1}^n (y_i - \mu_n)^2}{n - 1}} \quad (5.16)$$

and N is the total number of signals. Example: if $n = 13$ we calculate the mean and standard deviation of the 13 smallest intensities, then we use these to calculate the normalized intensities of all signals.

We use an iterative scheme to find the outliers:

1. $j = 0$
2. Define a threshold, t , with the *student's-t* distribution with $p = 0.01$ and $N - j - 1$ degrees of freedom
3. Calculate the number of signal intensities of $Z_{i,N-j} > t$ and call it $n_{outliers}$
4. If
 - $n_{outliers} > j$
 - then
 - telomere signal $N - j$ is an outlier
 - $j = j + 1$
 - repeat step 2, 3 and 4
 - else
 - we stop the iterations

Now the $n_{outliers}$ highest signal intensities are *outliers* and the others *inliers*. We normalize the intensity signals to the mean intensity of the *inliers*. In figure 5.5 we see the result of the algorithm.

5.3 Chromosome overlap

5.3.1 Introduction

Telomeric aggregates and the initiation of breakage-bridge-fusion cycles with subsequent chromosomal rearrangements prompted us to investigate whether chromosomes were affected in their 3D nuclear positions during MycER activation. To this end, we examined the overlap of specific chromosomes over the

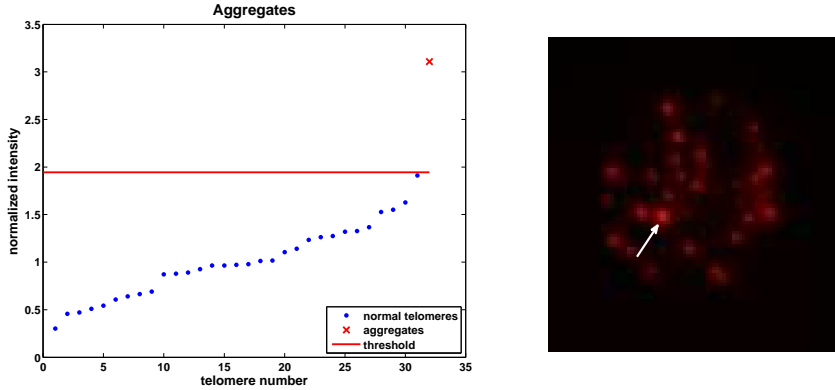


Figure 5.5: Left: graph showing the result of the 'normal method'. Using the iterative scheme from section 5.2.2 we can define a threshold (red line) and define aggregates (red crosses) and normal sized telomeres (blue dots). Right: maximum intensity projection in the axial direction of the 3D image of the telomeres. The arrow indicates the found aggregates.

120 hour period. SKY (Spectral Karyotyping) of MycER-activated PreB cells suggested chromosomal rearrangements involving chromosomes 7, 13, and 17. Additional rearrangements were found but did not reach significant levels (data not shown). We examined three combinations of chromosomes over a 96 hour period. This period covered all peaks of telomere aggregate formation (Fig. 4B in (Louis et al., 2005b)).

5.3.2 Methods

Cells and Conditional Myc Activation.

Culture conditions have been described for Ba/F3 (Fest et al., 2002) and PreB (Mai et al., 1999) cells. The plasmacytoma cell line MOPC460D was a gift of J. Mushinski (National Institutes of Health, Bethesda). Cell viability was determined by hemocytometer counts by using trypan blue. The primary mouse plasmacytoma DCPC21 was isolated from a BALB/c mouse (Wiener et al., 1999). v-abl/ myc-induced plasmacytomas (Wiener et al., 1995) and primary lymphocytes were collected from BALB/c mice (Central Animal Care protocol 02-039). To activate MycER (Littlewood et al., 1995) in Ba/F3 or PreB cells, 105 cells per ml were treated with 100 nM 4-hydroxytamoxifen (4HT). Cells were split 24 h before 4HT treatment. Non-4HT treated control cells were cultivated in ethanol, which is used to dissolve 4HT (Chiang et al., 2003; Adams

et al., 1985; Littlewood et al., 1995). Two different MycER activation schemes were performed. First, analyses of c-Myc-induced changes in 3D telomere organization were carried out after a single addition of 4HT that was left in the culture medium until its biological effects subsided (Grenman et al., 1988a,b; Mandlekar et al., 2000). Nuclei were examined every 24 h over a 10-day period. A second time course was performed every 6 h for 120 h (Fig. 5.6). To enable a time-dependent analysis of Myc activation, 4HT was given for 2 or 12 h and was removed. Alternatively, 4HT was added every 12 h or was given once but left in the culture. MycER activation was determined by fluorescent immunohistochemistry. Further details can be found in (Louis et al., 2005b).

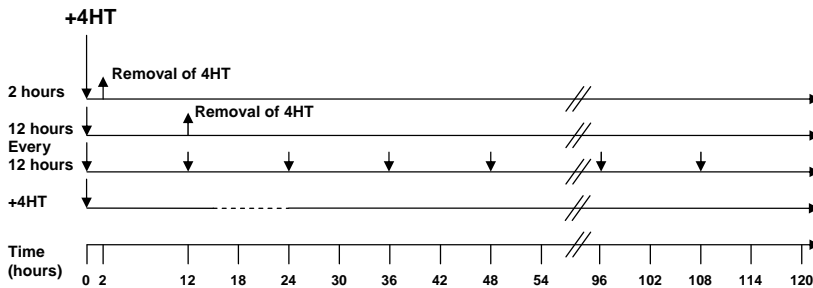


Figure 5.6: MycER activation scheme. The effects of 4HT last 15-24 h in cell lines (40-42), as indicated by dashed lines. Cells were harvested every 6 h over a time period of 120 h. Mock-treated control cells were processed in parallel.

Imaging and processing

Fixation and chromosome painting was carried out as described in (Beatty et al., 2002) by using paints for mouse chromosomes 5 (Cy3), 13 (FITC), 7 (Cy3), 10 (FITC), and 17 (FITC) from Applied Spectral Imaging (Vista, CA). 3D image acquisition of painted nuclei was performed as described above. Measurements of chromosomal overlaps were performed after 3D image acquisition and constrained iterative deconvolution as follows (Fig. 5.7): (i) based on the DAPI counterstain image, we determined the 3D boundary of the nuclear volume. Data outside that volume were ignored. (ii) For each one of the chromosomes, we determined an intensity threshold and referred only to voxels that were above the threshold that belonged to the specific chromosomes. The total volume occupied by each one of the chromosome pairs is measured (V_1 and V_2). (iii) The volume occupied by both chromosome pairs is measured, V_o . By dividing this value by V_1 and by V_2 , the level of overlap relative to the total volume of each chromosome pair was measured, V_o/V_1 , V_o/V_2 .

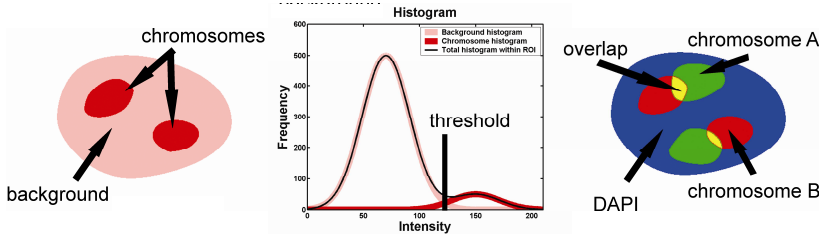


Figure 5.7: We clearly see that the larger part is background and the smaller parts are the chromosomes (left). We also see this in the histogram (middle). The large peak is from the background (with the lower intensities), and the smaller peak is from the chromosomes (higher intensities). The threshold is chosen where the fitted Gaussian shaped curve of the background histogram and of the chromosome histogram intersect. When we do this for both channels (chromosome pair A and B, right), we can calculate the volume occupied by chromosome pair A (green plus yellow), chromosome pair B (red plus yellow) and the overlap (only yellow). A more detailed description of these steps is as follows: (i) The region of interest (ROI) is selected by using the DAPI channel. The grayscale image from this channel is thresholded by using an isodata algorithm (Ridler and Calvard, 1978). This threshold is the mean value of the object intensities plus the mean value of the background intensities divided by two. We fill the holes of the resulting binary image by binary propagation with the edge as seed and the inverted DAPI binary as a mask. Now we invert the resulting binary image, leaving us with the holes filled. (ii) Now that we have the ROI (i.e., the location of the DNA), we can use this finding to make a histogram in this ROI of the channel of interest (i.e., the red or green channel). We use an adaptation of minimum-error thresholding (Rosenfeld and Kak, 1976). Here, we estimate the background level from the histogram by fitting a Gaussian curve on the lower (large) part of the histogram, assuming the larger part of the image to be background. We use a least squares fit for this. After we subtract this fitted Gaussian curve, we end up with the histogram belonging to the signal, in our case, the chromosomes. After this step, we threshold where the signal histogram and the background fitted curve intersect. (iii) Performing this algorithm on both channels leaves us with two binary images. After a logical AND operation (Young et al., 1998), where we input these binary images we end up with a binary image of the overlap. The sum of the voxels divided by the sum of the voxels of either the red or green binary image gives us a normalized parameter indicating the level of overlap.

5.3.3 Results

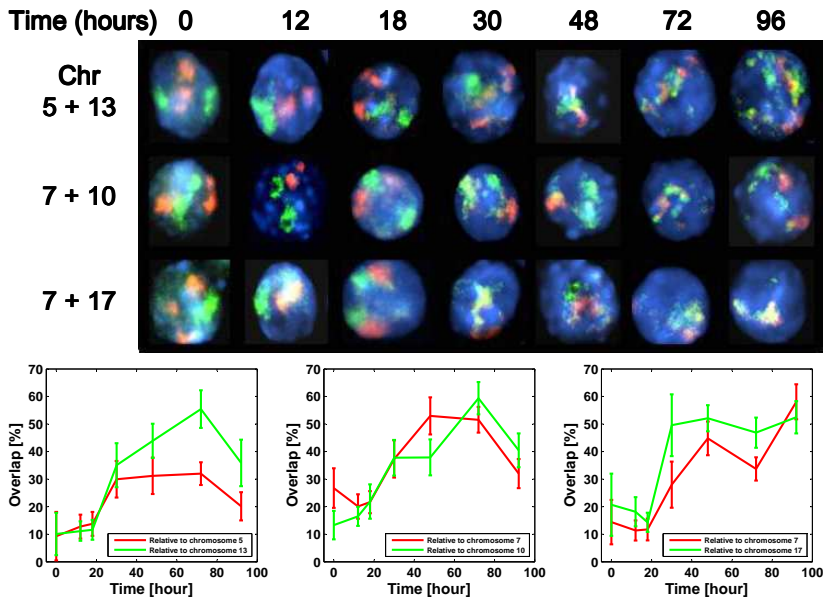


Figure 5.8: Chromosome positions in Myc-activated nuclei. (Top) Representative nuclei painted with chromosome paints over a period of 96 h after 4HT (Fig. 5.6). (Top row) Chromosomes 5 and 13. (Middle row) Chromosomes 7 and 10. (Bottom row) Chromosomes 7 and 17. (Bottom) Measurements of chromosomal overlaps in nuclei of c-Myc deregulated cells for chromosomes 5 and 13 (Left), 7 and 10 (Center), and 7 and 17 (Right) over a 96-h period.

As shown in Fig. 5.8, we observed a change in overlaps between chromosomes 5 (red) and 13 (green) over the time course (Figs. 7 A and B). Both chromosomes were found in closer vicinity as the cells entered into the first telomere aggregate cycle. Chromosomes 10 (green) and 7 (red) also showed increases in the percentage of overlap (Fig. 5.8), as did chromosomes 7 (red) and 17 (green) (Fig. 5.8). Representative 3D movies are shown in Movies 1-3 of the supplemental materials of (Louis et al., 2005b).

5.3.4 Conclusions and discussion

Local chromosome movement increases chromosomal overlap in the nucleus. This temporal change in local positioning may permit the direct contact of chromosomal ends and facilitate recombinations and/or fusions. Such movements were observed after c-Myc deregulation and suggested an impact of the

oncogene on local nuclear positioning of chromosomes. Chromosome movements were previously studied and found by others as well (Zink and Cremer, 1998; Walter et al., 2003; Vourc'h et al., 1993; Ferguson and Ward, 1992; Bridger et al., 2000). Several regulatory pathways involving oncogene deregulation may affect the 3D nuclear organization. Oncoproteins, including c-Myc, can alter the 3D nuclear organization and the organization of chromatin (Fischer et al., 1998a,b; Chadee et al., 1999).

5.4 Conclusions and discussion

In this chapter we have developed a method to measure the relative telomere length in 3D images of nuclei. We see a clear correlation between given relative intensities and measured intensities in simulations of a large number of small spots with several larger spots. We feel combining this tool together with one of the proposed methods to find aggregates will facilitate studying structural telomeric behavior in normal and cancerous cases. These tools have been used in several of these studies (Raz et al., 2006).

We also propose a method to measure chromosomal overlap of two chromosomes in cell nuclei. A higher overlap was measured after 40-80 hours after c-Myc activation.

Analysis of the three-dimensional redistribution of nuclear components in human mesenchymal stem cells

Abstract

Background To better understand the impact of changes in nuclear architecture on nuclear functions it is essential to quantitatively elucidate the three-dimensional organization of nuclear components using image processing tools.

Methods We have developed a novel image segmentation method, which involves a contrast enhancement and a subsequent thresholding step. In addition, we have developed a new segmentation method of the nuclear volume using the fluorescent background signal of a probe. After segmentation of the nucleus, a first order normalization is performed on the signal positions of the component of interest to correct for the shape of the nucleus. This method allows us to compare various signal positions within a single nucleus, and also on pooled data obtained from multiple nuclei, which may vary in size and shape. The algorithms have been tested by analyzing the spatial localization of nuclear bodies in relation to the nuclear center. Next, we have used this new tool to study change in the spatial distribution of nuclear components in cells before and after caspase-8 activation, which leads to cell death.

Results Compared to the morphological TopHat method, this method gives similar but significantly faster results. A clear shift in the radial distribution of centromeres has been found, while the radial distribution of telomeres was changed much less. In addition, we have used this new tool to follow changes in the spatial distribution of two nuclear components in the same nucleus during activation of apoptosis. We show that after caspase-8 activation, when centromeres shift to a peripheral localization, the spatial distribution of promyelocytic leukemia nuclear bodies (PML-NBs) does not change while that of centromeres does.

Conclusions We propose that the use of this new image segmentation method will contribute to a better understanding of the 3D spatial organization of the cell nucleus.

Parts of this chapter are based on [Vermolen et al. \(2008\)](#).

6.1 Introduction

The major function of the cell nucleus is to regulate gene activity which depends on well-studied molecular mechanisms such as transcription, pre-mRNA splicing and ribosome assembly. In contrast to what is known about the molecular regulation of these mechanisms, far less is understood about the extent that the dynamics of nuclear components and the three-dimensional (3D) structural organization of the nucleus contribute to the regulation of nuclear functions. Recent models of high-order genome organization suggest a non-random spatial localization of chromosome territories in the interphase nucleus ([Cremer et al., 2004](#)). Further, sub-chromosomal domains are suggested to be non-randomly positioned. Centromeres containing pericentric satellite repeats show a preferential peripheral orientation in G0-arrested human cells ([Solovei et al., 2004](#)) as well as in differentiated cells ([Solovei et al., 2004](#); [Wiblin et al., 2005](#); [Stadler et al., 2004](#)). Telomeres, which are satellite repeats at the ends of chromosomes, reveal a cell cycle-dependent localization in B-lymphocytes. Throughout the cell cycle, telomeres exhibit a spherical organization but in G2 they reorganize to a disk shape ([Chuang et al., 2004](#)). Together, these studies indicate a non-random organization of heterochromatic regions in the nucleus, and suggest that a functional correlation exists between the spatial organization of heterochromatic regions and gene activity ([Stadler et al., 2004](#); [Parada et al., 2004](#); [Kim et al., 2004](#)). The mechanism by which heterochromatic regions are organized in the cell nucleus is currently unknown. There is emerging genomic and biochemical evidence that give a role to the nuclear lamina proteins (which support the structure of the nucleus) in chromatin organization and control of gene activity ([Gruenbaum et al., 2005](#); [Kosak and Groudine, 2004](#); [Pickersgill et al., 2006](#)). Thus, if changes in lamina organization lead to changes in chromatin organization, correlation should be found using quantitative image analysis. In a recent study, we found that in cells, which are activated for apoptosis via the caspase-8 pathway, changes in lamina organization are followed by changes in the spatial organization of telomeres and centromeres ([Raz et al., 2006](#)). In this work we developed a new quantitative image analysis tool which facilitates our studies of the 3D localization of multiple (e.g. two or three) nuclear components relative to the lamina structure in a single cell. To test whether this tool is able to quantify changes in spatial localization, we have compared the spatial organization of different nuclear components (i.e. telomeres, centromeres

and PML-NBs) in human mesenchymal stem cells (hMSCs) before and after caspase-8 activation. Image processing and analysis have been carried out in four basic steps:

1. segmentation of the nuclear bodies
2. segmentation of the nucleus
3. normalization of the nuclear body positions
4. analysis of the nuclear body radial distribution

Several methods to detect spots, e.g. fluorescently marked telomere, centromere, and chromosomal loci signals, have been reported in the past. Most studies have been done in 2D (Netten et al., 1997; Feuerbach et al., 2002; Galy et al., 2000; Figueiredo et al., 2002) or semi-3D (Grigoryan et al., 2002); detection was done sequentially on the 2D slices of the 3D image stack. Few studies have implemented true 3D detection methods. In (Thomann et al., 2002, 2003) a Gaussian model driven segmentation algorithm has been used with the assumption of a high intensity curvature and high intensity. In (Therizols et al., 2006) a 3D wavelet method is used to segment the signals. Previously we segmented spots of varying intensities using a TopHat algorithm (Chuang et al., 2004; Vermolen et al., 2005a; Meyer, 1979).

In this study we applied a model driven segmentation approach, which is suitable for spots with varying intensities. To segment the nuclear bodies in three dimensions, we have adapted a method developed by Olivo-Marin (Olivo-Marin, 2002) and extended it to 3D. Together with an interactive correction step, this method allows us to accurately determine the spatial positioning of nuclear bodies. We also present and compare three segmentation algorithms to segment the nuclear volume. We show that the three methods give comparable results. Since one of the segmentation methods does not require imaging of the nuclear lamina it is technically easier and therefore preferable. Furthermore, as the nucleus of hMSCs vary in size and shape; we introduce a normalization of the nuclear size, which makes it possible to perform quantitative image analysis on pooled data. After normalization, the radial distribution of different nuclear components within a single nucleus has been analyzed. This provides a means to compare different components in a single cell and also to pool the different data from different cells, that is, a cell population. Using this new image processing tool, we show that changes in nuclear architecture can be monitored after activation of apoptosis by caspase-8.

6.2 Materials and Methods

6.2.1 Segmentation

Probe

Segmentation of the marker is described in section 4.2.

Nucleus

To position the molecular markers within the nucleus we had to define the nuclear sphere. We have used three methods to segment the nucleus (Fig. 6.1):

1. The lamina is labeled with lamin A or lamin B fused to a fluorescent gene product and the segmentation of the nucleus is carried out on the fluorescent signal of the lamina protein (Fig. 6.1Ai, labeled as 'la').
2. The lamina is labeled in the same way as in 1, but the segmentation of the nucleus is carried out after a logarithmic stretch of the lamina signal (Fig. 6.1Aii, labeled as 'nla').
3. The lamina is not labeled, but a logarithmic stretch is performed on the background signal of the probe. The background is probably caused by fluorescent molecules unbound to structural nuclear elements. This logarithm stretch highlights the probe background, which is sufficient to define the shape of the nucleus (Fig. 6.1Aiii, named as 'n'), now segmentation is carried out on this stretched background.

In all three methods we segment the nucleus with an isodata thresholding algorithm (Ridler and Calvard, 1978) after noise reduction by a convolution with a Gaussian filter. This easy algorithm is sufficient because there is only one nucleus per image and we do not need to separate touching objects. While method 3 differs from method 1 and 2 by using a different probe, method 1 and 2 differ from each other because the logarithmic stretch causes the isodata thresholding algorithm to choose a different thresholding level. Although method 3 is more sensitive to the signal-to-noise ratio compared to the other methods, nuclear segmentation worked for all our images with all three methods. This results in three different segmentations of the nucleus.

6.2.2 Probe distribution

Radial position with a segmented nucleus

In order to calculate the radial distribution of the components inside the nucleus, a method is required that eliminates the effect of the nuclear size and the non-spherical shape. We use a method that produces a normalized distance of

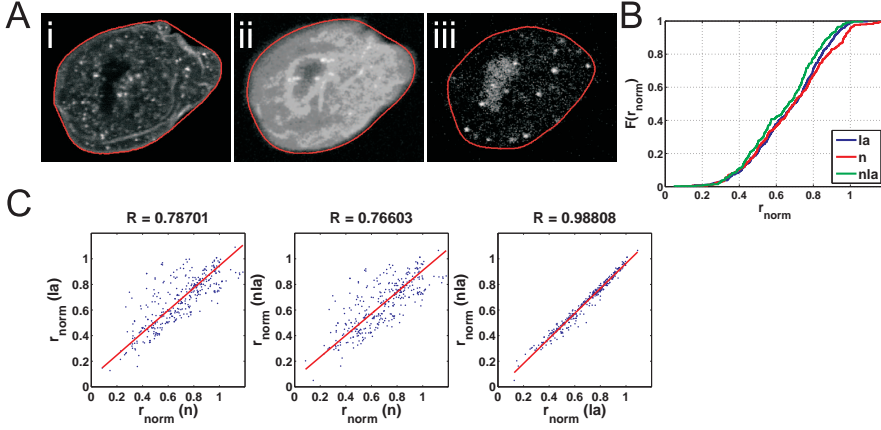


Figure 6.1: Comparison of three methods for segmentation of the nuclear sphere. A. Image representations of the different segmentation methods in one nucleus. The red line outlines the nuclear boundary, which was found by each of the segmentation methods. The n segmentation is calculated from the logarithmic stretched image of the background of the probe signal (i). The nla segmentation is calculated from the logarithmic stretched image of the lamina signal (ii). The la segmentation is calculated from the image of the lamina signal (iii). B. Cumulative distribution function plot of Trf1-DsRed spatial distribution. Plots show the distribution of pooled data from 5 cells after activation of caspase-8 at passage 4 using the three segmentation methods, object background (n), lamina in background mode (nla) and the lamina (la). C. Linear regression analyses of the pooled data (B) reveals that the nla and la segmentation methods are statistically equivalent. The n method, however, gives a good estimation of the spatial localization of the probes in the nucleus, as compared with the other two methods.

a probe, r_{norm} , from the center of a nucleus to the nuclear boundary. Thus $r_{norm} = 0$ means that a probe is at the center and $r_{norm} = 1$ means that a probe is at the boundary. Our method approximates the nucleus shape of the hMSCs by an ellipsoid. To normalize the probe position we used the coordinates of the pixels obtained from the segmented nucleus to find the center of the nucleus. We also use these coordinates to transform the coordinates of the probe signals (x_i, y_i, z_i) . From the nuclear coordinates we calculate the covariance matrix (the second order moments of inertia of the nuclear voxels). We then perform a singular value decomposition on this matrix. This gives a rotation matrix, S_n , and a matrix with the singular values, V_n . The singular values represent the variances, σ_i^2 , in the different principal directions given by the rotation matrix. The principal directions are the directions in which the

variances are largest. The singular matrix has the form:

$$V_n = \begin{pmatrix} \sigma_1^2 & 0 & 0 \\ 0 & \sigma_2^2 & 0 \\ 0 & 0 & \sigma_3^2 \end{pmatrix} \quad (6.1)$$

where:

$$\sigma_1 > \sigma_2 > \sigma_3 \quad (6.2)$$

The singular values, σ_i^2 , for a sphere with radius R are given by the standard integral for the variance:

$$\sigma_x^2 = \int_{-R}^R P(x)x^2 dx \quad (6.3)$$

where

$$P(x) = \frac{3}{4} \frac{R^2 - x^2}{R^3} \quad (6.4)$$

The product of the integral gives $\frac{1}{5}R^2$. Now we rotate and normalize the variances of the probe signal coordinates to the unit sphere:

$$(x_{new}, y_{new}, z_{new}) = (x_i, y_i, z_i) \times S_n \times \sqrt{V_n^{-1}} \times \sqrt{\frac{1}{5}} \quad (6.5)$$

A schematic presentation of this transformation is shown in Fig. 6.2. After this transformation the normalized radius, r_{norm} , is simply:

$$r_{norm} = \sqrt{x_{new}^2 + y_{new}^2 + z_{new}^2} \quad (6.6)$$

6.2.3 Cell preparation and molecular labeling

Human MSCs were isolated from bone marrow samples of adult donors and were cultured as described in (Raz et al., 2006). To visualize nuclear proteins, we expressed lamin A, lamin B (components of the nuclear lamina), Trf1, Trf2 (both associated with the telomeres) and CenpA (associated with the centromeres) as fusion proteins with GFP and DsRed in hMSCs as previously described (Raz et al., 2006). PML-NBs were visualized after fixation of the cells using a specific anti-PML antibody as described in (Raz et al., 2006).

6.2.4 Image acquisition and processing

3D images from live or fixed cells were acquired using a confocal microscope (Leica, model TCS-2) equipped with an argon/krypton laser and a 100x/1.3 NA Apo objective. The 3D images were loaded in TeloView, a custom non-commercial in-house developed analysis program for MatLab (The Mathworks,

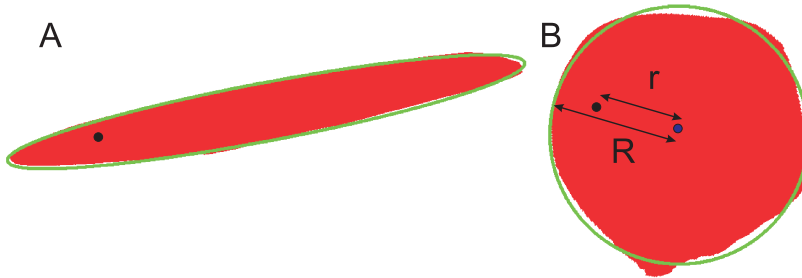


Figure 6.2: Schematic representation of the normalization procedure. A. 2D example of a nucleus (red) with a signal (black dot). B. The same nucleus (A) after normalization. The normalized radius, r_{norm} , is given by r/R . If $R = 1$ (green circle, the unit sphere), r_{norm} is given by equation 6.5.

Natick, MA). TeloView makes use of DIPimage (Luengo Hendriks et al., 1999) developed at the Quantitative Imaging Group (TU-Delft, The Netherlands, <http://www.diplib.org>). The typical sampling distances in the lateral direction were on the order of $\Delta x = \Delta y = 40$ nm and in the axial direction on the order of $\Delta z = 160$ nm. This anisotropy in the sampling distances makes weighing of pixel values and distances necessary during segmentation and analysis; we have solved this by interpolating the images to get isotropic sampling distances. Typical image size was $512 \times 512 \times 40$. Before segmentation, the images are interpolated linearly in the z direction from Δz to $\Delta z'$ so that the sampling distance in all three directions is the same: $\Delta x = \Delta y = \Delta z'$. Note that our remark about the fundamental anisotropy in the confocal PSF in section 4.2 still holds after this interpolation, since the PSF it is an intrinsic property of the microscope system and is therefore independent of the sampling.

6.2.5 Statistics

The spatial distribution of the probe is plotted in a cumulative distribution function (CDF) plot. We have chosen this representation to avoid the problem of choosing a binning size in a histogram (the conventional way of showing the empirical data distribution function), which can heavily influence the appearance of the distribution. The CDF of the radius, $F(r)$, is defined as:

$$F(r_{norm}) = \frac{\text{number of observations} \leq r_{norm}}{\text{total number of observations}} \quad (6.7)$$

Distributions were compared with the Wilcoxon rank-sum test (Mann and Whitney, 1947; Wilcoxon, 1945) and the two sample Kolmogorov-Smirnov test (Hollander and Wolfe, 1973).

6.3 Results

6.3.1 Probe segmentation

We have compared the scale space segmentation algorithm with a TopHat transformation method. For the scale space segmentation we used three scales ($i = 0, 1, 2$) and $base = 100$ nm. The TopHat transformation uses parameters for the structuring element (SE) as previously described in (Vermolen et al., 2005a); a spherical SE with radius 742 nm. A total of 14 images with 524 telomere signals have been analyzed. On average we find 37 telomeres per cell. This number is lower than expected since not all telomeres are labeled with this method and also possibly due to telomere merging. We have chosen the threshold for the scale-space method, T (see section 4.2.2), so that the number of interactive corrections (signals added and signals removed) in each image is minimized. This resulted in 26 corrections (≈ 2 corrections per image). For the threshold in the TopHat method we chose a threshold for each image in the same manner, resulting in 30 corrections (≈ 2 corrections per image). This number of corrections is acceptable for practical use. While no significant differences in the number of corrections have been found between the two methods, the new method, based on scale space, gives significant advantages in computation time. Typical computation time of the TopHat method is 5-15 minutes versus 1-3 minutes with the scale space method on an AMD OpteronTM244 1.8 GHz processor with 8 GB RAM. We have, therefore, chosen to use the scale space method.

6.3.2 Nuclear segmentation

We have used the fluorescent protein-tagged lamin A or lamin B proteins to visualize the nuclear envelope. During apoptosis, before degradation of the lamina proteins, the nuclear envelope changes from a round-flat to a convoluted shape. In addition, as previously described, the spatial organization of centromeres and telomeres changes (Raz et al., 2006). At this point we are interested in developing a more accurate quantitative image analysis tool that will allow us to study the spatial distribution of nuclear components with respect to the nuclear shape. We therefore tested three methods for segmentation of the nucleus (Fig. 6.1A). The segmentation methods are described in 6.2. The performance of the three segmentation methods has been tested on telomere signals. 3D confocal images were taken from hMSCs after activation of caspase-8 at passage 4, expressing Trf1-DsRed and lamin B-GFP. An example of a nucleus expressing both fluorescent fusion proteins is shown in Fig. 6.3A. After nuclear segmentation, using each of the methods, nuclear boundaries were indicated by a red line (Fig. 6.1A, red line). The nuclear shape was determined by segmenting the Lamin B-GFP signal without a contrast stretch (la), or after

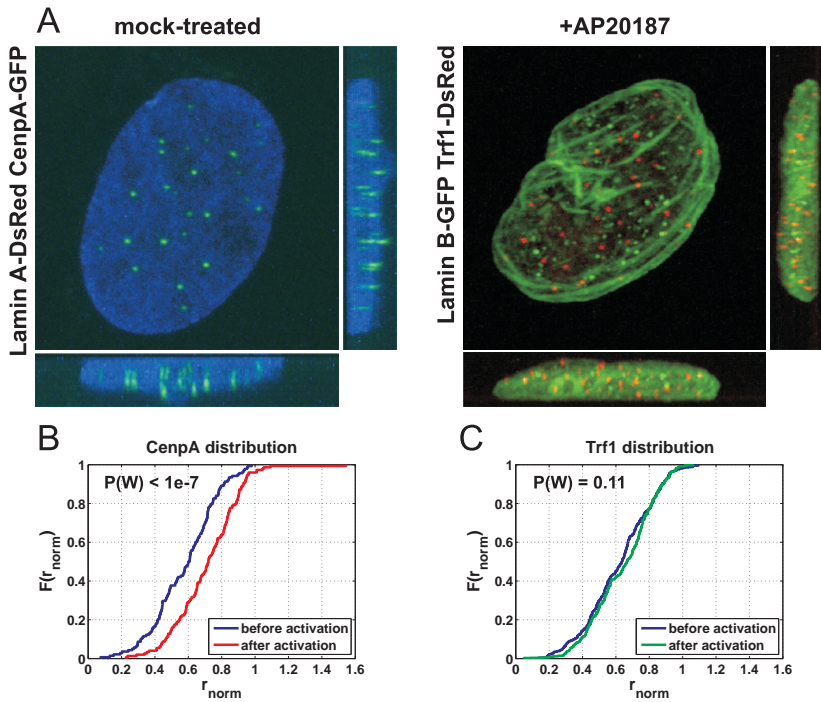


Figure 6.3: Changes in the spatial distribution of telomeres and centromeres during activation of apoptosis. A. Left: maximum intensity projection of a mock-treated cell expressing lamin A-DsRed (blue) together with CenpA-GFP (green). Right: maximum intensity projection of a cell expressing Lamin B-GFP (green), Trf1-DsRed (red) and FKCS, after AP20187 treatment. Lamin A and B expression marks the inner nuclear membrane, B. Cumulative distribution function plot of the spatial distribution of CenpA-GFP before (blue line) and 4 hours after caspase-8 activation with 100 nM AP20187 (red line). Segmentation of the nuclear sphere was carried out using the *nla* segmentation. The graph shows pooled data from 4 cells for each treatment. The P value of the Wilcoxon rank-sum test is given by $P(W)$. C. Cumulative distribution function plot of the spatial distribution of Trf1-DsRed analyzed in cells expressing lamin B-GFP before (blue line) and 6 hours after caspase-8 activation (green line). Segmentation of the nuclear sphere was carried out using the *nla* segmentation method. The graph shows pooled data from 9 cells and 5 cells before and after caspase-8 activation respectively. The P value of the Wilcoxon rank-sum test is given by $P(W)$.

a logarithmic stretch (*nla*), or by segmenting the nuclear background signal derived from Trf1-DsRed (*n*) (Fig. 6.1Ai, ii and iii, respectively). Comparisons of the three methods revealed little differences (Fig. 6.1B and 6.1C). Therefore, when analyzing the change in distribution of nuclear bodies from the center of mass it is possible to use the *n* method for nuclear segmentation as it is significantly faster and simpler. During apoptosis however, the shape of the nuclear envelope changes and in addition, the lamina forms intranuclear structures (Raz et al., 2006). Thus it would be interesting to analyze the change in the spatial distribution relative to the lamina. As changes in lamina organization precede changes in the spatial organization of centromeres and telomeres (Raz et al., 2006), it is possible that changes in lamina spatial organization affect the spatial organization of nuclear bodies. We emphasize that the images contain single nuclei, so that more sophisticated segmentation algorithms (Ortiz de Solórzano et al., 1999; Sarti et al., 2000; Parvin et al., 2007), where multiple cells or nuclei are present in one image, are unnecessary in this study. Next, the spatial distribution of the telomeres was quantified within each of the segmented nuclei and the frequency of telomeres was plotted against the nuclear radius. To perform statistical tests on pooled data, it was essential to first normalize the radius of the nuclei, as illustrated in Fig. 6.2 and in equation 6.5. The pooled data from five nuclei, representing 343 Trf1-DsRed fluorescent dots, revealed no significant differences between the three segmentation methods (Fig. 6.1B and 6.1C). However, a detailed comparison revealed that the *la* and the *nla* methods show a high level of correlation, $R = 0.99$ (Fig. 1C). This is not surprising since the *la* and the *nla* method are both based on the lamina signal. The correlation of the *la* or *nla* methods with the *n* method was less, $R = 0.78$ and $R = 0.77$ respectively (Fig. 6.1C). We suggest that the *n* method for nuclear segmentation gives a good estimation for the spatial localization of nuclear components. This method, however, does not outline the nuclear envelop as precisely when we visually evaluate the resulting segmentation and compare it to the lamina segmentation methods. Finally some general notes on the effect of radial positioning with respect to the accuracy of the segmentation. The segmentation might give two kinds of errors: with and without a bias. Statistically, these errors will not affect the final results in our application. For the non-biasing errors this is trivial: the ellipse fitting as explained in the section on probe distribution will reduce this error to a very small contribution. When a bias exists it will not affect differences in the radial position distributions we report. The accuracy of the nuclear segmentation should be further explored, depending on the specific application. Nevertheless, as the *n* segmentation method is the fastest and requires significantly less work, it can be used to estimate the nuclear shape.

6.3.3 Changes in spatial distribution during activation of apoptosis

To test whether the n segmentation method can be used to study changes in the spatial organization of multiple nuclear components, we applied it to images from cells expressing both CenpA-GFP and Trf1-DsRed (Fig. 6.4A). These cells were induced to go into apoptosis by expressing the FK8 gene, which was activated after AP20187 treatment (Raz et al., 2006; Carlotti et al., 2005). To study eventual differences between centromere and telomere spatial organization we developed a method that finds the radial distribution of multiple nuclear components in a single nucleus. Live hMSCs were imaged before and 4 and 6 hours after AP20187 treatment.

First we tested this method on single living cells. For a mock-treated cell, the CDF plots show that the centromeres have a higher preference for a central localization as compared with telomere positioning (Fig. 6.4B, mock-treated). This observation confirms previous studies done on fixed cells, showing a more central localization of centromeres as compared to telomeres in interphase nuclei in various cell types (Amrichová et al., 2003; Weierich et al., 2003). The CDF plot revealed that few telomeres are localized at the nuclear periphery in untreated hMSCs (Fig. 6.4B). This observation is consistent with previous studies showing that few telomeres are physically associated with the nuclear lamina (Ludérus et al., 1996). After apoptosis activation by AP20187 treatment, we observed in the round-shaped nucleus that the centromeres were positioned near the nuclear periphery (Fig. 6.4B, round, and (Kosak and Groudine, 2004)). At that time, in the same nucleus, the spatial distribution of telomeres was more central than the centromeres (Fig. 6.4B, round). At a later stage, in the convoluted-shaped nucleus, the radial distribution of centromeres and telomeres did not differ, as shown by the statistical tests. These analyses suggest that both centromeres and telomeres change position within the three-dimensional space of the cell nucleus at different rates. In addition, the shift in centromere localization is more significant than the telomere shift.

Unlike centromeres and telomeres that show changes in spatial organization upon caspase-8 activation, PML-NB organization is initially unchanged, even in cells showing a convoluted nuclear shape. The distribution of PML-NBs is disrupted only when the lamina shows massive degradation (Raz et al., 2006). Here we used our newly developed method to quantitatively compare the spatial localization of centromeres and PML-NBs in mock-treated cells showing a round nuclear shape and in caspase-8 activated cells showing a convoluted nuclear shape. To visualize PML-NBs, cells were fixed and incubated with the appropriate antibodies (Fig. 6.5A). The frequency distributions of both centromeres and PML-NBs were plotted in histograms against radial rings. Representative results are shown in Fig. 6.5B. The analysis of this one cell reveals a peripheral localization of several CenpA molecules in caspase-8 activated cells, while the spatial distribution of PML-NBs does not change. This

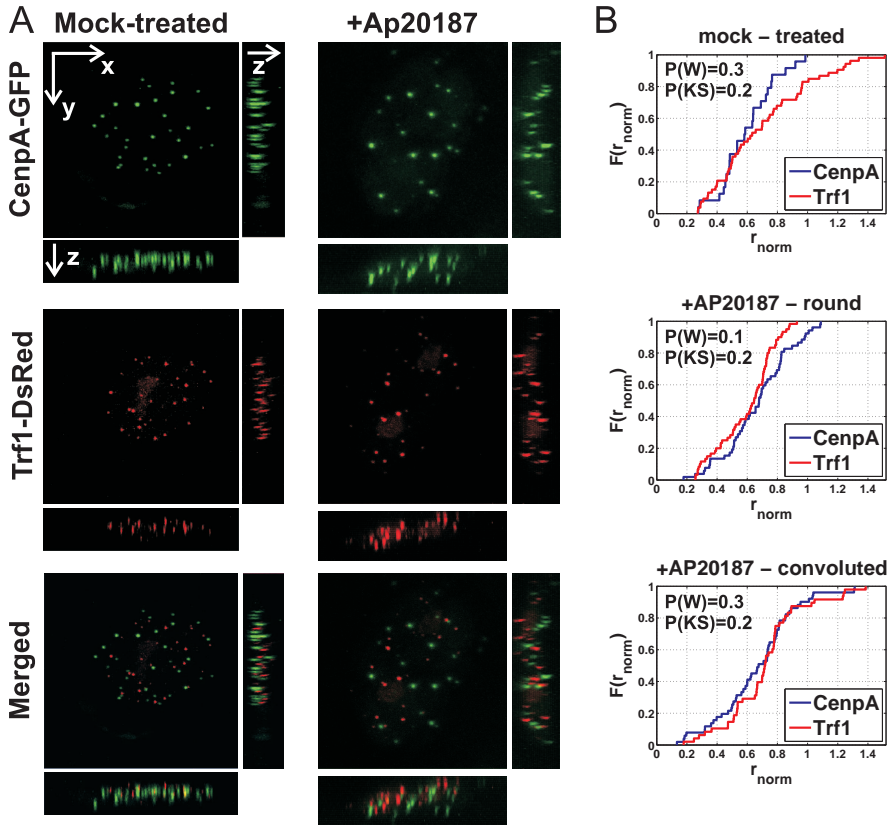


Figure 6.4: Distribution analysis of centromeres and telomeres in a single nucleus. A. Maximum intensity projections of single hMSC expressing CenpA-GFP (green) and Trf1-DsRed (Red), before (mock-treated) and after caspase-8 activation (+AP20187, 4 hours treatment). B. Cumulative distribution function plots showing changes in the relative distribution of CenpA and Trf1 signals during caspase-8 activation in a single representative cell. Analyses were carried out in cells expressing the FK8 vector before and after caspase-8 activation (+AP20187). Four hours after AP20187 treatment the nucleus showed a round shape and after 6 hours a convoluted shape. The plots show that in normal hMSCs, the spatial distribution of CenpA is more central compared with that of Trf1. Upon caspase-8 activation, the cumulative distribution function plots reveal a clear shift in CenpA localization towards the periphery in round-shape nuclei. A very similar distribution of CenpA and Trf1 is found in convoluted nuclei. The P values of the Wilcoxon rank-sum test and the two sample Kolmogorov-Smirnov test are given by $P(W)$ and $P(KS)$ respectively.

observation is consistent with previous results, showing shift in CenpA distributions in apoptotic cells (Raz et al., 2006)

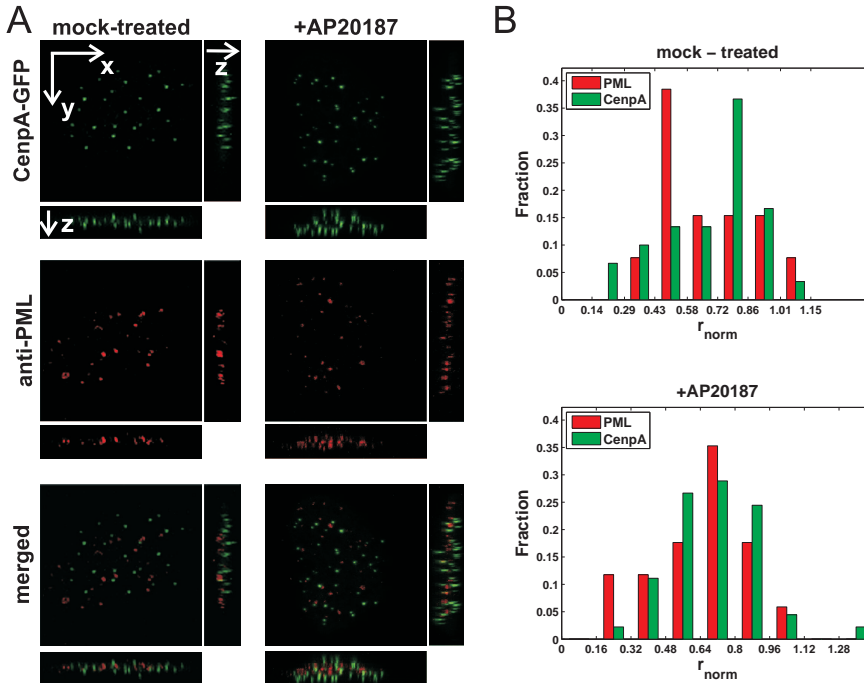


Figure 6.5: PML-NB and CenpA distribution in a single nucleus. A. Maximum intensity projection of CenpA-GFP (green) and PML-NB (red) within single hMSCs expressing FK8, before (mock-treated) and after caspase-8 activation (+AP20187, 6 hours treatment). B. Histograms show the fraction of centromeres (green) or PML-NBs (red) distributed in a normalized nucleus of a representative cell. Analyses were carried out on mock-treated cells and on cells 6 hours after AP20187 treatment. In mock-treated hMSCs, CenpA and PML-NBs have a similar spatial distribution pattern but upon caspase-8 activation, some CenpA molecules show a peripheral localization while the distribution of PML-NBs is not affected.

Next, we analyzed pooled data obtained from multiple cells expressing both CenpA-GFP and Trf1-DsRed before or 4 hours after caspase-8 activation. When we visually (by eye) analyzed the localization of centromeres with respect to the center of the nucleus, centromeres were shown to be centrally localized, while after caspase-8 activation their spatial distribution shifted towards the nuclear periphery (Fig. 6.3A). A clear shift in centromere localization towards the nuclear periphery is also shown by the CDF plot of the pooled

data of four cells before and after treatment with $P < 1e - 7$ calculated by the Wilcoxon rank sum test, using the nuclear background segmentation method (Fig. 6.3B). In contrast, the P values calculated by the Wilcoxon rank sum test did not show a significant change in Trf1 localization between nine normal nuclei, and five convoluted-shaped nuclei, in caspase-8 activated cells. From the CDF plot, we estimate that 20% of the telomeres are localized to the nuclear periphery ($r > 0.8$) in both untreated and AP20187 treated cells. Thus, the radial distribution of centromeres shifts to the periphery in convoluted-shaped nuclei, whereas the telomere distribution is not changed.

6.4 Discussion

We have presented a new segmentation method to analyze probe distribution in the cell nucleus. This method shows a clear improvement over the conventional thresholding method especially with respect to computation time. We have also developed an improved segmentation method for the nucleus itself, which is based on background signals derived from expressed fluorescent fusion proteins. Using this method, the preparation of samples and the acquisition of images is technically easier and therefore superior. Segmented images allow us to quantify the spatial distribution of centromeres and telomeres relative to the nuclear center. This tool also allows us to quantitatively relate the radial distribution between two or three nuclear components in a single cell nucleus. It also allows a quantitative comparison of the distribution of a nuclear components between cells and between treatments under varying biological situations. As an example, we have shown how the distribution of centromeres and telomeres changes after activation of caspase-8, which results in cell death.

Nuclear architecture not only describes the organization of the nucleus, but recent studies indicate that the spatial and temporal organization of the genome is likely to have functional consequences. Changes in nuclear architecture are among the most dramatic hallmarks of development and differentiation processes and defects in architectural elements of the cell nucleus are responsible for several human diseases. Yet, it is not clear how the spatial localization of nuclear bodies is changed during change in cell function. Two major models have been suggested (Misteli, 2005). In the structural scaffold concept, structural proteins, like the lamina proteins, confine the activation regions of the genome. The self-reinforcing concept suggests that the spatial organization of nuclear bodies reflects the transcriptional activity of the genome. Following the self-reinforcing concept, we have examined the spatial localization of nuclear probes relative to the center of mass. However, it is possible that changes in the nuclear lamina also contribute to the spatial localization of nuclear structures, as in human diseases with mutations in lamina genes (Broers et al., 2006) or cell death (Broers et al., 2006; Misteli, 2005; Raz et al., 2006). Therefore it would

be interesting to test the change in the spatial localization of nuclear probes using the distance transform approach (Mullikin, 1992), where the smallest distance to the lamina will be found. The distance from the center of the nucleus to the nuclear component, as described in this study, and the distance from the lamina to the nuclear component are fundamentally different metrics and can give complementary information. Finally, it would be most interesting to compare the two methods with respect to the biological models. A broad application of both tools will eventually lead to a better understanding of the nuclear architecture and its relation to nuclear function.

6.5 Acknowledgments

We thank the members of Prof. H. Tanke's group for fruitful discussions.

Conclusions and summary

Cancer is one of the most well-known groups of diseases that finds its cause in cells having chromosomal aberrations. How and why these aberrations can occur is one of the most important questions asked in modern molecular biology. In the last decades it has become clear that gene regulation in the nucleus, where the chromosomes reside, is strongly correlated with structural organization of nuclear components like the telomeres, centromeres and the chromosomes themselves. With new microscopes, better cameras and new fluorescent labels, the demand for analyses of all the images that can be made is growing. This thesis is devoted to provide a framework of image processing and data analyses tools to answer some of these questions.

This thesis describes methods to process and analyze images of the cell nucleus. The distribution of the molecules in the nucleus is strongly correlated to its function (see chapter 1). The images that have been analyzed are acquired by fluorescence microscopy (see chapter 2). Because we have worked with 3D images, the images have been deconvolved (see chapter 3).

In chapter 3 we also show the effect of deconvolution on images acquired by a modified conventional microscope. This modification consists of an array of pinholes in the illumination path and a CCD camera where the image from pixels which coincide with the holes from the array is separated from the image from the other pixels. We show that using both of these images gives the advantage that the holes can be put together as close as five times the hole diameter. This produces the ability to acquire the images 16 times faster.

In chapter 4 we describe two methods, a TopHat transform and a Scale-Space method, which make it easier to segment images of telomeres. These two methods have been tested on their ability to enhance the contrast of two neighboring signals. The Scale-Space method performs, in general, better than the TopHat transform. This Scale-Space method is used to segment telomeres. A parameter, ρ_T , is defined to analyze how flat the spatial distribution of telomeres is. Using this parameter we show that telomeres in lymphocytes from healthy mice are distributed in a sphere-like volume during the G0/1 and S phase of the cell cycle. However, during the G2 phase (before chromosomes

condense) this distribution changes and the telomeres position in a disk-like spatial distribution.

In chapter 5 a method to determine the relative length of a telomere is described. With the help of outlier-statistics, an extraordinarily high intensity, which is an indication of aggregation, can be determined. Through image processing we show that the organization of telomeres and chromosomes is disrupted after activation of c-Myc. Telomeres aggregate after chromosomes overlap. This is followed by a so called 'breakage-fusion-bridge' cycles and associated chromosomal aberrations.

A different mechanism which changes the distribution of nuclear components is induction of caspase-8, which is a protein which plays a role in apoptosis (programmed cell death). In chapter 6 the Scale-Space method from chapter 4 is used to segment fluorescent signals related to telomeres, centromeres and PML-NBs. The shape of the nucleus is determined using the background signal (non-specific signal). The radial distribution of the localized components is determined and normalized with respect to the nuclear shape. This technique is used to show a redistribution of the centromeres to the periphery of the nucleus, as opposed to the distribution of the telomeres, which is preserved.

Conclusies en samenvatting

Kanker is een van de bekendste groepen ziektes die zijn oorzaak vindt in afwijkingen in de chromosomen. Hoe en waarom deze afwijkingen ontstaan is één van de meest belangrijke vragen in de moderne moleculaire biologie. In de afgelopen twintig jaar is het duidelijk geworden dat regulatie van de genen in de celkern gecorreleerd is met de structuur van componenten, zoals telomeren, centromeren en chromosomen zelf, in de celkern. Met nieuwe microscopen, betere camera's en nieuwe fluorescerende labels, is de vraag om alle beelden die gemaakt kunnen worden te kunnen analyseren gestegen. Dit proefschrift is toegespitst om een raamwerk te verschaffen om een gedeelte van de gestelde vragen te kunnen beantwoorden.

Dit proefschrift behandelt methoden om beelden van de celkern te verwerken en analyseren. De distributie van de moleculen in de celkern zijn nauw verbonden met de functie (zie hoofdstuk 1). De beelden die geanalyseerd worden zijn verkregen door middel van fluorescentiemicroscopie (zie hoofdstuk 2). Omdat gewerkt wordt met drie dimensionale beelden zijn deze ook gedeconvolveerd (zie hoofdstuk 3).

In hoofdstuk 3 laten we ook zien wat het effect is van deconvolutie op beelden gemaakt met een gemodificeerde conventionele microscoop. De modificatie bestaat uit een matrix van gaatjes in het belichtingspad en een CCD camera waarbij een onderscheid wordt gemaakt tussen een beeld opgebouwd uit de pixels die overeenkomen met de gaatjes en een beeld opgebouwd uit de andere pixels van de CCD. We laten zien dat het gebruik van beide beelden in de deconvolutie een voordeel oplevert, waarbij de gaatjes tot 5 keer hun grootte van elkaar verwijderd kunnen zijn. Dit zorgt voor een 16 keer snellere beeldacquisitie.

In hoofdstuk 4 beschrijven we twee methoden, een TopHat transformatie en een Scale-Space methode, om makkelijker beelden van telomeren te segmenteren. Deze twee methoden zijn getoetst op hun vermogen om het contrast van twee dicht bij elkaar liggende signalen te verhogen. De Scale-Space methode geeft over het algemeen betere resultaten dan de TopHat transformatie. Deze Scale-Space methode is gebruikt om de telomeren te segmenteren. Om de

ruimtelijke distributie van de telomeren te analyseren hebben we een parameter gedefinieerd die aangeeft hoe plat deze structuur is: ρ_T . Gebruik makende van deze parameter zien we dat in lymfocyten van gezonde muizen tijdens de G0/1 en S fasen van de cel cyclus de distributie van de telomeren in een bol structuur zitten. Echter tijdens de G2 fase (nog voor de chromosomen condenseren) verandert de distributie en vormen de telomeren een schijf.

In hoofdstuk 5 beschrijven we een methode om de relatieve lengte van een telomeer te bepalen. Door middel van 'outlier' statistiek kan dan bepaald worden of een signaal een buitengewoon hoge intensiteit, wat een indicatie is voor een samenklontering, heeft. Mede door middel van beeldverwerking laten we zien dat de organisatie van telomeren en chromosomen verstoord wordt door het activeren van c-Myc. Na overlap van bepaalde chromosomen plakken sommige telomeren samen. Dit wordt dan weer gevolgd door zogenaamde 'breakage-fusion-bridge' cyclussen en daarmee gepaarde chromosomale afwijken.

Een ander mechanisme waarin de distributie van componenten in de celkern veranderd is de inductie van caspase-8, een eiwit die een rol speelt in apoptose (gereguleerde celdood). In hoofdstuk 6 wordt de Scale-Space segmentatie methode uit hoofdstuk 4 gebruikt om fluorescente signalen gerelateerd aan telomeren, centromeren en PML-lichamen te lokaliseren. Aan de hand van het achtergrond signaal (het niet-specifieke signaal) wordt de vorm van de celkern bepaald. Van de gelokaliseerde componenten wordt een radiële distributie bepaald welk genormaliseerd is aan de hand van de vorm van de celkern. Met behulp van deze technieken wordt een verschuiving van de distributie van de centromeren naar de rand van de celkern getoond, waarbij de radiële distributie van de telomeren gehandhaafd blijft.

References

- E. Abbe. Beiträge zur Theorie des Mikroskops und der mikroskopischen Wahrnehmung. *Archiv für Mikroskopische Anatomie*, 9:413–468, 1873. [cited at p. 14]
- J. M. Adams, A. W. Harris, C. A. Pinkert, L. M. Corcoran, W. S. Alexander, S. Cory, R. D. Palmiter, and R. L. Brinster. The *c-myc* oncogene driven by immunoglobulin enhancers induces lymphoid malignancy in transgenic mice. *Nature*, 318(6046): 533–538, 1985. [cited at p. 71, 80]
- A. Akhtar and S. M. Gasser. The nuclear envelope and transcriptional control. *Nature Reviews Genetics*, 8(7):507–517, 2007. [cited at p. 6]
- J. Amrichová, E. Lukášová, S. Kozubek, and M. Kozubek. Nuclear and territorial topography of chromosome telomeres in human lymphocytes. *Experimental Cell Research*, 289(1):11–26, 2003. [cited at p. 95]
- B. G. Beatty, S. Mai, and J. A. Squire, editors. *FISH: A practical approach*. Oxford University Press, Oxford, 2002. [cited at p. 81]
- E. Betzig, G. H. Patterson, R. Sougrat, O. W. Lindwasser, S. Olenych, J. S. Bonifacino, M. W. Davidson, J. Lippincott-Schwartz, and H. F. Hess. Imaging intracellular fluorescent proteins at nanometer resolution. *Science*, 313(5793):1642–1645, 2006. [cited at p. 24, 25]
- H. Bin Sun, J. Shen, and H. Yokota. Size-dependent positioning of human chromosomes in interphase nuclei. *Biophysical Journal*, 79(1):184–190, 2000. [cited at p. 6]
- A. Bolzer, G. Kreth, I. Solovei, D. Koehler, K. Saracoglu, C. Fauth, S. Müller, R. Eils, C. Cremer, M. R. Speicher, and T. Cremer. Three-dimensional maps of all chromosomes in human male fibroblast nuclei and prometaphase rosettes. *PLOS Biology*, 3(5):826–842, 2005. [cited at p. 5]
- G. J. Brakenhoff. Imaging modes in confocal scanning light-microscopy (CSLM). *Journal of Microscopy-Oxford*, 117:233–242, 1979. [cited at p. 9]

- G. J. Brakenhoff, P. Blom, and P. Barends. Confocal scanning light-microscopy with high aperture immersion lenses. *Journal of Microscopy-Oxford*, 117:219–232, 1979. [cited at p. 9]
- J. M. Bridger, S. Boyle, I. R. Kill, and W. A. Bickmore. Re-modelling of nuclear architecture in quiescent and senescent human fibroblasts. *Current Biology*, 10(3):149–152, 2000. [cited at p. 84]
- J. L. V. Broers, F. C. S. Ramaekers, G. Bonne, R. Ben Yaou, and C. J. Hutchison. Nuclear lamins: laminopathies and their role in premature ageing. *Physiological Reviews*, 86(3):967–1008, 2006. [cited at p. 98]
- F. Carlotti, A. Zaldumbide, P. Martin, K. E. Boulukos, R. C. Hoeben, and P. Pognonec. Development of an inducible suicide gene system based on human caspase 8. *Cancer Gene Therapy*, 12(7):627–639, 2005. [cited at p. 95]
- D. N. Chadee, M. J. Hendzel, C. P. Tyllipski, C. D. Allis, D. P. Bazett-Jones, J. A. Wright, and J. R. Davie. Increased Ser-10 phosphorylation of histone H3 in mitogen-stimulated and oncogene-transformed mouse fibroblasts. *Journal of Biological Chemistry*, 274(35):24914–24920, 1999. [cited at p. 84]
- Y. C. Chiang, S. C. Teng, Y. N. Su, F. J. Hsieh, and K. J. Wu. c-Myc directly regulates the transcription of the NBS1 gene involved in DNA double-strand break repair. *Journal of Biological Chemistry*, 278(21):19286–19291, 2003. [cited at p. 71, 80]
- T. C. Y. Chuang, S. Moshir, Y. Garini, A. Y. C. Chuang, I. T. Young, B. Vermolen, R. van den Doel, V. Mougey, M. Perrin, M. Braun, P. D. Kerr, T. Fest, P. Boukamp, and S. Mai. The three-dimensional organization of telomeres in the nucleus of mammalian cells. *BMC Biology*, 2(1):12, 2004. [cited at p. 53, 54, 57, 72, 86, 87]
- J. A. Conchello. Superresolution and convergence properties of the expectation-maximization algorithm for maximum-likelihood deconvolution of incoherent images. *Journal of the Optical Society of America A*, 15(10):2609–2619, 1998. [cited at p. 28]
- T. Cremer and C. Cremer. Chromosome territories, nuclear architecture and gene regulation in mammalian cells. *Nature Reviews Genetics*, 2(4):292–301, 2001. [cited at p. 2, 3]
- T. Cremer, K. Küpper, S. Dietzel, and S. Fakan. Higher order chromatin architecture in the cell nucleus: on the way from structure to function. *Biology of the Cell*, 96(8):555–567, 2004. [cited at p. 2, 86]
- F. Crick. Central dogma of molecular biology. *Nature*, 227(5258):561–563, 1970. [cited at p. 1]
- C. M. D’Cruz, E. J. Gunther, R. B. Boxer, J. L. Hartman, L. Sintasath, S. E. Moody, J. D. Cox, S. I. Ha, G. K. Belka, A. Golant, R. D. Cardiff, and L. A. Chodosh. c-MYC induces mammary tumorigenesis by means of a preferred pathway involving spontaneous *Kras2* mutations. *Nature Medicine*, 7(2):235–239, 2001. [cited at p. 71]

-
- J. Dekker. Gene regulation in the third dimension. *Science*, 319(5871):1793–1794, 2008. [cited at p. 2]
- W. Denk, J. H. Strickler, and W. W. Webb. Two-photon laser scanning fluorescence microscopy. *Science*, 248(4951):73–76, 1990. [cited at p. 23]
- P. Duesberg, R. H. Li, A. Fabarius, and R. Hehlmann. The chromosomal basis of cancer. *Cellular Oncology*, 27(5-6):293–318, 2005. [cited at p. 4]
- A. Egner, C. Geisler, C. von Middendorff, H. Bock, D. Wenzel, R. Medda, M. Andresen, A. C. Stiel, S. Jakobs, C. Eggeling, A. Schonle, and S. W. Hell. Fluorescence nanoscopy in whole cells by asynchronous localization of photoswitching emitters. *Biophysical Journal*, 93(9):3285–3290, 2007. [cited at p. 25]
- D. W. Felsher and J. M. Bishop. Transient excess of MYC activity can elicit genomic instability and tumorigenesis. *Proceedings of the National Academy of Sciences of the United States of America*, 96(7):3940–3944, 1999a. [cited at p. 71]
- D. W. Felsher and J. M. Bishop. Reversible tumorigenesis by MYC in hematopoietic lineages. *Molecular Cell*, 4(2):199–207, 1999b. [cited at p. 71]
- M. Ferguson and D. C. Ward. Cell-cycle dependent chromosomal movement in premitotic human T-lymphocyte nuclei. *Chromosoma*, 101(9):557–565, 1992. [cited at p. 84]
- T. Fest, V. Mougey, V. Dalstein, M. Hagerty, D. Milette, S. Silva, and S. Mai. c-MYC overexpression in Ba/F3 cells simultaneously elicits genomic instability and apoptosis. *Oncogene*, 21(19):2981–2990, 2002. [cited at p. 80]
- F. Feuerbach, V. Galy, E. Trelles-Sticken, M. Fromont-Racine, A. Jacquier, E. Gilson, J. C. Olivo-Marin, H. Scherthan, and U. Nehrpass. Nuclear architecture and spatial positioning help establish transcriptional states of telomeres in yeast. *Nature Cell Biology*, 4(3):214–221, 2002. [cited at p. 6, 87]
- L. M. Figueiredo, L. H. Freitas-Junior, E. Bottius, J. C. Olivo-Marin, and A. Scherf. A central role for *Plasmodium falciparum* subtelomeric regions in spatial positioning and telomere length regulation. *Embo Journal*, 21(4):815–824, 2002. [cited at p. 87]
- R. Figueroa, H. Lindenmaier, M. Hergenbahn, K. V. Nielsen, and P. Boukamp. Telomere erosion varies during *in vitro* aging of normal human fibroblasts from young and adult donors. *Cancer Research*, 60(11):2770–2774, 2000. [cited at p. 54]
- A. H. Fischer, J. A. Bond, P. Taysavang, O. E. Battles, and D. Wynford-Thomas. Papillary thyroid carcinoma oncogene (RET/PTC) alters the nuclear envelope and chromatin structure. *American Journal of Pathology*, 153(5):1443–1450, 1998a. [cited at p. 84]
- A. H. Fischer, D. N. Chadee, J. A. Wright, T. S. Gansler, and J. R. Davie. Ras-associated nuclear structural change appears functionally significant and independent of the mitotic signaling pathway. *Journal of Cellular Biochemistry*, 70(1):130–140, 1998b. [cited at p. 84]

- T. S. Fisher and V. A. Zakian. Ku: A multifunctional protein involved in telomere maintenance. *DNA Repair*, 4(11):1215–1226, 2005. [cited at p. 6]
- T. S. Fisher, A. K. P. Taggart, and V. A. Zakian. Cell cycle-dependent regulation of yeast telomerase by Ku. *Nature Structural & Molecular Biology*, 11(12):1198–1205, 2004. [cited at p. 6]
- J. Fox. Robust regression, January 2002. Appendix to An R and S-PLUS Companion to Applied Regression. [cited at p. 76]
- N. P. Galatsanos and A. K. Katsaggelos. Methods for choosing the regularization parameter and estimating the noise variance in image restoration and their relation. *IEEE Transactions on Image Processing*, 1(3):322–336, 1992. [cited at p. 35]
- V. Galy, J. C. Olivo-Marin, H. Scherthan, V. Doye, N. Rascalou, and U. Nehrbaas. Nuclear pore complexes in the organization of silent telomeric chromatin. *Nature*, 403(6765):108–112, 2000. [cited at p. 6, 87]
- Y. Garini, B. J. Vermolen, and I. T. Young. From micro to nano: recent advances in high-resolution microscopy. *Current Opinion in Biotechnology*, 16(1):3–12, 2005. [cited at p. 23]
- D. Gerlich, J. Beaudouin, B. Kalbfuss, N. Daigle, R. Eils, and J. Ellenberg. Global chromosome positions are transmitted through mitosis in mammalian cells. *Cell*, 112(6):751–764, 2003. [cited at p. 5]
- S. F. Gibson and F. Lanni. Experimental test of an analytical model of aberration in an oil-immersion objective lens used in three-dimensional light-microscopy. *Journal of the Optical Society of America A*, 8(10):1601–1613, 1991. [cited at p. 14, 49, 74]
- G. H. Golub, M. Heath, and G. Wahba. Generalized cross-validation as a method for choosing a good ridge parameter. *Technometrics*, 21(2):215–223, 1979. [cited at p. 36]
- S. Grenman, A. Shapira, and T. E. Carey. *In vitro* response of cervical-cancer cell-lines CaSki, HeLa, and ME-180 to the antiestrogen tamoxifen. *Gynecologic Oncology*, 30(2):228–238, 1988a. [cited at p. 81]
- S. E. Grenman, J. A. Roberts, B. G. England, M. Grönroos, and T. E. Carey. *In vitro* growth-regulation of endometrial carcinoma-cells by tamoxifen and medroxyprogesterone acetate. *Gynecologic Oncology*, 30(2):239–250, 1988b. [cited at p. 81]
- A. M. Grigoryan, E. R. Dougherty, J. Kononen, L. Bubendorf, G. Hostetter, and O. Kallioniemi. Morphological spot counting from stacked images for automated analysis of gene copy numbers by fluorescence *in situ* hybridization. *Journal of Biomedical Optics*, 7(1):109–122, 2002. [cited at p. 87]
- Y. Gruenbaum, A. Margalit, R. D. Goldman, D. K. Shumaker, and K. L. Wilson. The nuclear lamina comes of age. *Nature Reviews Molecular Cell Biology*, 6(1):21–31, 2005. [cited at p. 86]

-
- F. R. Hampel, E. M. Ronchetti, P. J. Rousseeuw, and W. A. Stahel. *Robust Statistics: the approach based on influence functions*. Wiley Series in Probability and Statistics. John Wiley and Sons, 1986. [cited at p. 76, 77]
- W. Heisenberg. Über den anschaulichen Inhalt der quantentheoretischen Kinematik und Mechanik. *Zeitschrift für Physik A Hadrons and Nuclei*, 45(127):172–198, 1927. [cited at p. 21]
- S. Hell and E. H. K. Stelzer. Properties of a 4Pi confocal fluorescence microscope. *Journal of the Optical Society of America A*, 9(12):2159–2166, 1992. [cited at p. 23]
- S. W. Hell. Far-field optical nanoscopy. *Science*, 316(5828):1153–1158, 2007. [cited at p. 23]
- S. W. Hell and J. Wichmann. Breaking the diffraction resolution limit by stimulated-emission: stimulated-emission-depletion fluorescence microscopy. *Optics Letters*, 19(11):780–782, 1994. [cited at p. 24]
- S. T. Hess, T. P. K. Girirajan, and M. D. Mason. Ultra-high resolution imaging by fluorescence photoactivation localization microscopy. *Biophysical Journal*, 91:4258–4272, 2006. [cited at p. 24]
- K. Hironaka, V. M. Factor, D. F. Calvisi, E. A. Conner, and S. S. Thorgeirsson. Dysregulation of DNA repair pathways in a transforming growth factor α/c -myc transgenic mouse model of accelerated hepatocarcinogenesis. *Laboratory Investigation*, 83(5):643–654, 2003. [cited at p. 71]
- M. Hofmann, C. Eggeling, S. Jakobs, and S. W. Hell. Breaking the diffraction barrier in fluorescence microscopy at low light intensities by using reversibly photoswitchable proteins. *Proceedings of the National Academy of Sciences of the United States of America*, 102(49):17565–17569, 2005. [cited at p. 24]
- M. Hollander and D. Wolfe. *Nonparametric statistical methods*. Probability and Statistics. John Wiley & Sons, New York, 1973. [cited at p. 91]
- M. Jain, C. Arvanitis, K. Chu, W. Dewey, E. Leonhardt, M. Trinh, C. D. Sundberg, J. M. Bishop, and D. W. Felsher. Sustained loss of a neoplastic phenotype by brief inactivation of MYC. *Science*, 297(5578):102–104, 2002. [cited at p. 71]
- A. Jemal, T. Murray, E. Ward, A. Samuels, R. C. Tiwari, A. Ghafoor, E. J. Feuer, and M. J. Thun. Cancer statistics, 2005. *CA: A Cancer Journal for Clinicians*, 55(1):10–30, 2005. [cited at p. 4]
- A. Karlsson, D. Deb-Basu, A. Cherry, S. Turner, J. Ford, and D. W. Felsher. Defective double-strand DNA break repair and chromosomal translocations by MYC overexpression. *Proceedings of the National Academy of Sciences of the United States of America*, 100(17):9974–9979, 2003a. [cited at p. 71]

- A. Karlsson, S. Giuriato, F. Tang, J. Fung-Weier, G. Levan, and D. W. Felsher. Genomically complex lymphomas undergo sustained tumor regression upon *MYC* inactivation unless they acquire novel chromosomal translocations. *Blood*, 101(7): 2797–2803, 2003b. [cited at p. 71]
- G. v. Kempen. *Image restoration in fluorescence microscopy*. Ph.d. thesis, Delft University of Technologies, 1998. [cited at p. 36, 74]
- S. H. Kim, P. G. McQueen, M. K. Lichtman, E. M. Shevach, L. A. Parada, and T. Misteli. Spatial genome organization during T-cell differentiation. *Cytogenetic and Genome Research*, 105(2-4):292–301, 2004. [cited at p. 86]
- D. E. Knuth. *The art of computer programming: seminumerical algorithms*. Addison-Wesley, 1969. [cited at p. 37]
- S. T. Kosak and M. Groudine. Gene order and dynamic domains. *Science*, 306(5296): 644–647, 2004. [cited at p. 86, 95]
- G. Kreth, J. Finsterle, J. von Hase, M. Cremer, and C. Cremer. Radial arrangement of chromosome territories in human cell nuclei: A computer model approach based on gene density indicates a probabilistic global positioning code. *Biophysical Journal*, 86(5):2803–2812, 2004. [cited at p. 5]
- R. I. Kumaran, R. Thakar, and D. L. Spector. Chromatin dynamics and gene positioning. *Cell*, 132(6):929–934, 2008. [cited at p. 2]
- T. I. Kuschak, B. C. Kuschak, C. L. Taylor, J. A. Wright, F. Wiener, and S. Mai. c-Myc initiates illegitimate replication of the *ribonucleotide reductase R2* gene. *Oncogene*, 21(6):909–920, 2002. [cited at p. 71]
- P. M. Lansdorp, N. P. Verwoerd, F. M. vandeRijke, V. Dragowska, M. T. Little, R. W. Dirks, A. L. Raap, and H. J. Tanke. Heterogeneity in telomere length of human chromosomes. *Human Molecular Genetics*, 5(5):685–691, 1996. [cited at p. 73]
- T. D. Littlewood, D. C. Hancock, P. S. Danielian, M. G. Parker, and G. I. Even. A modified estrogen-receptor ligand-binding domain as an improved switch for the regulation of heterologous proteins. *Nucleic Acids Research*, 23(10):1686–1690, 1995. [cited at p. 80, 81]
- S. F. Louis, B. Gruhne, and S. Mai. *Towards an understanding of DNA replication in normal and cancer cells: facts and concepts*, chapter 1, pages 1–56. Progress in Oncogene Research. NovaScience Publishers, Inc. Hauppauge, New York, 2005a. [cited at p. 71]
- S. F. Louis, B. J. Vermolen, Y. Garini, I. T. Young, A. Guffei, Z. Lichtensztein, F. Kuttler, T. C. Y. Chuang, S. Moshir, V. Mougey, A. Y. C. Chuang, P. D. Kerr, T. Fest, P. Boukamp, and S. Mai. c-Myc induces chromosomal rearrangements through telomere and chromosome remodeling in the interphase nucleus. *Proceedings of the National Academy of Sciences of the United States of America*, 102(27): 9613–9618, 2005b. [cited at p. 71, 72, 80, 81, 83]

-
- M. E. Ludérus, M. Steensel, B. van Ginkel, L. Chong, O. C. M. Sibon, F. F. M. Cremers, and T. de Lange. Structure, subnuclear distribution, and nuclear matrix association of the mammalian telomeric complex. *Journal of Cell Biology*, 135(4): 867–881, 1996. [cited at p. 95]
- C. Luengo Hendriks, B. Rieger, M. van Ginkel, G. van Kempen, and L. van Vliet. DIPimage, a scientific image processing toolbox for MatLab, 1999. [cited at p. 31, 36, 37, 91]
- M. Mac Partlin, E. Homer, H. Robinson, C. J. McCormick, D. H. Crouch, S. T. Durant, E. C. Matheson, A. G. Hall, D. A. F. Gillespie, and R. Brown. Interactions of the DNA mismatch repair proteins MLH1 and MSH2 with c-MYC and MAX. *Oncogene*, 22(6):819–825, 2003. [cited at p. 71]
- S. Mai. Overexpression of *c-myc* precedes amplification of the gene encoding dihydrofolate reductase. *Gene*, 148(2):253–260, 1994. [cited at p. 71]
- S. Mai and Y. Garini. The significance of telomeric aggregates in the interphase nuclei of tumor cells. *Journal of Cellular Biochemistry*, 97(5):904–915, 2006. [cited at p. 4, 53]
- S. Mai and J. F. Mushinski. c-Myc-induced genomic instability. *Journal of Environmental Pathology, Toxicology and Oncology*, 22(3):179–199, 2003. [cited at p. 71]
- S. Mai, M. Fluri, D. Siwarski, and K. Huppi. Genomic instability in MycER-activated Rat1A-MycER cells. *Chromosome Research*, 4(5):365–371, 1996a. [cited at p. 71]
- S. Mai, J. Hanley-Hyde, and M. Fluri. c-Myc overexpression associated DHFR gene amplification in hamster, rat, mouse and human cell lines. *Oncogene*, 12(2):277–288, 1996b. [cited at p. 71]
- S. Mai, J. Hanley-Hyde, G. J. Rainey, T. I. Kuschak, J. T. Paul, T. D. Littlewood, H. Mischak, L. M. Stevens, D. W. Henderson, and J. F. Mushinski. Chromosomal and extrachromosomal instability of the *cyclin D2* gene is induced by *Myc* overexpression. *Neoplasia*, 1(3):241–252, 1999. [cited at p. 80]
- L. Mandel and E. Wolf. *Optical Coherence and Quantum Optics*. Cambridge University Press, 1995. [cited at p. 34]
- S. Mandlekar, V. Hebbar, K. Christov, and A. N. T. Kong. Pharmacodynamics of tamoxifen and its 4-hydroxy and *N*-desmethyl metabolites: Activation of caspases and induction of apoptosis in rat mammary tumors and in human breast cancer cell lines. *Cancer Research*, 60(23):6601–6606, 2000. [cited at p. 81]
- H. B. Mann and D. R. Whitney. On a test of whether one of two random variables is stochastically larger than the other. *Annals of Mathematical Statistics*, 18(1): 50–60, 1947. [cited at p. 91]
- D. Marinkovic, T. Marinkovic, B. Mahr, J. Hess, and T. Wirth. Reversible lymphomagenesis in conditionally c-MYC expressing mice. *International Journal of Cancer*, 110(3):336–342, 2004. [cited at p. 71]

- J. Markham and J. A. Conchello. Fast maximum-likelihood image-restoration algorithms for three-dimensional fluorescence microscopy. *Journal of the Optical Society of America A*, 18(5):1062–1071, 2001. [cited at p. 28]
- R. Mayer, A. Brero, J. von Hase, T. Schroeder, T. Cremer, and S. Dietzel. Common themes and cell type specific variations of higher order chromatin arrangements in the mouse. *BMC Cell Biology*, 6, 2005. [cited at p. 5]
- K. J. Meaburn and T. Misteli. Chromosome territories. *Nature*, 445(7126):379–381, 2007. [cited at p. 3]
- F. Meyer. Iterative image transformations for an automatic screening of cervical smears. *Journal of Histochemistry and Cytochemistry*, 27(1):128–135, 1979. [cited at p. 55, 57, 87]
- F. Meyer and S. Beucher. Morphological segmentation. *Journal of Visual Communication and Image Representation*, 1(1):21–46, 1990. [cited at p. 55]
- M. Minsky. Microscopy Apparatus. Patent, December 1961. United States Patent Office, patent number 3013467. [cited at p. 9]
- T. Misteli. Concepts in nuclear architecture. *BioEssays*, 27(5):477–487, 2005. [cited at p. 3, 98]
- T. Misteli. Beyond the sequence: cellular organization of genome function. *Cell*, 128(4):787–800, 2007. [cited at p. 2, 3]
- J. C. Mullikin. The vector distance transform in two and three dimensions. *CVGIP: Graphical Models and Image Processing*, 54(6):526–535, 1992. [cited at p. 99]
- R. G. Nagele, A. Q. Velasco, W. J. Anderson, D. J. McMahon, Z. Thomson, J. Fazekas, K. Wind, and H. Lee. Telomere associations in interphase nuclei: possible role in maintenance of interphase chromosome topology. *Journal of Cell Science*, 114(2):377–388, 2001. [cited at p. 6]
- C. E. Nesbit, J. M. Tersak, and E. V. Prochownik. *MYC* oncogenes and human neoplastic disease. *Oncogene*, 18(19):3004–3016, 1999. [cited at p. 7, 71]
- H. Netten, I. T. Young, L. J. vanVliet, H. J. Tanke, H. Vrolijk, and W. C. R. Sloos. FISH and chips: automation of fluorescent dot counting in interphase cell nuclei. *Cytometry*, 28(1):1–10, 1997. [cited at p. 5, 87]
- J. C. Olivo-Marin. Extraction of spots in biological images using multiscale products. *Pattern Recognition*, 35(9):1989–1996, 2002. [cited at p. 57, 58, 69, 87]
- C. Ortiz de Solórzano, E. García Rodríguez, A. Jones, D. Pinkel, J. W. Gray, D. Sudar, and S. J. Lockett. Segmentation of confocal microscope images of cell nuclei in thick tissue sections. *Journal of Microscopy*, 193:212–226, 1999. [cited at p. 94]
- L. A. Parada and T. Misteli. Chromosome positioning in the interphase nucleus. *Trends in Cell Biology*, 12(9):425–432, 2002. [cited at p. 2]

-
- L. A. Parada, P. G. McQueen, and T. Misteli. Tissue-specific spatial organization of genomes. *Genome Biology*, 5(7), 2004. [cited at p. 4, 86]
- B. Parvin, Q. Yang, J. Han, H. Chang, B. Rydberg, and M. H. Barcellos-Hoff. Iterative voting for inference of structural saliency and characterization of subcellular events. *IEEE Transactions on Image Processing*, 16(3):615–623, 2007. [cited at p. 94]
- S. Pelengaris, M. Khan, and G. I. Evan. Suppression of Myc-induced apoptosis in β cells exposes multiple oncogenic properties of Myc and triggers carcinogenic progression. *Cell*, 109(3):321–334, 2002. [cited at p. 71]
- H. Pickersgill, B. Kalverda, E. de Wit, W. Talhout, M. Fornerod, and B. van Steensel. Characterization of the drosophila melanogaster genome at the nuclear lamina. *Nature Genetics*, 38(9):1005–1014, 2006. [cited at p. 86]
- J. Ploem. The use of a vertical illuminator with interchangeable dichroic mirrors for fluorescence microscopy with incident light. *Zeitschrift für wissenschaftliche Mikroskopie*, 68:129–142, 1967. [cited at p. 9]
- M. Potter and K. B. Marcu. The c-myc story: Where we’ve been, where we seem to be going. In M. Potter and F. Melchers, editors, *C-Myc in B-Cell Neoplasia*, volume 224 of *Current Topics in Microbiology and Immunology*, pages 1–17, 1997. [cited at p. 71]
- M. Potter and F. Wiener. Plasmacytomagenesis in mice: model of neoplastic development dependent upon chromosomal translocations. *Carcinogenesis*, 13(10):1681–1697, 1992. [cited at p. 71]
- W. K. Pratt. *Digital Image Processing*. John Wiley & Sons, Inc., 1978. [cited at p. 27, 33]
- W. H. Press, S. A. Teukolsky, and W. T. Vetterling. *Numerical Recipes in C*. Cambridge University Press, second edition, 1992. [cited at p. 36]
- C. Rabl. Über zelltheilung. In C. Gegenbaur, editor, *Morphologisches Jahrbuch*, volume 10, pages 214–330, 1885. [cited at p. 2]
- V. Raz, F. Carlotti, B. J. Vermolen, E. van der Poel, W. C. R. Sloos, S. Knaän-Shanzer, A. A. F. de Vries, R. C. Hoeben, I. T. Young, H. J. Tanke, Y. Garini, and R. W. Dirks. Changes in lamina structure are followed by spatial reorganization of heterochromatic regions in caspase-8-activated human mesenchymal stem cells. *Journal of Cell Science*, 119(20):4247–4256, 2006. [cited at p. 84, 86, 90, 92, 94, 95, 97, 98]
- T. W. Ridler and S. Calvard. Picture thresholding using an iterative selection method. *IEEE Transactions on systems, man, and cybernetics*, SMC-8(8):630–632, 1978. [cited at p. 82, 88]

- L. D. Rockwood, T. A. Torrey, J. S. Kim, A. E. Coleman, A. L. Kovalchuk, S. Xiang, T. Ried, H. C. Morse III, and S. Janz. Genomic instability in mouse Burkitt lymphoma is dominated by illegitimate genetic recombinations, not point mutations. *Oncogene*, 21(47):7235–7240, 2002. [cited at p. 71]
- A. Rosenfeld and A. C. Kak. *Digital Picture Processing*, volume 2 of *Computer Science and Applied Mathematics*. Academic Press, Inc., New York, 1976. [cited at p. 82]
- G. T. Rudkin and B. D. Stollar. High-resolution detection of DNA-RNA hybrids *in situ* by indirect immunofluorescence. *Nature*, 265(5593):472–473, 1977. [cited at p. 11]
- M. J. Rust, M. Bates, and X. W. Zhuang. Sub-diffraction-limit imaging by stochastic optical reconstruction microscopy (STORM). *Nature Methods*, 3(10):793–795, 2006. [cited at p. 24]
- A. Sarti, C. O. de Solórzano, S. Lockett, and R. Malladi. A geometric model for 3-D confocal image analysis. *Ieee Transactions on Biomedical Engineering*, 47(12):1600–1609, 2000. [cited at p. 94]
- L. H. Schaefer, D. Schuster, and H. Herz. Generalized approach for accelerated maximum likelihood based image restoration applied to three-dimensional fluorescence microscopy. *Journal of Microscopy*, 204:99–107, 2001. [cited at p. 54]
- T. Sexton, H. Schober, P. Fraser, and S. M. Gasser. Gene regulation through nuclear organization. *Nature Structural & Molecular Biology*, 14(11):1049–1055, 2007. [cited at p. 6]
- C. M. Shachaf, A. M. Kopelman, C. Arvanitis, A. Karlsson, S. Beer, S. Mandl, M. H. Bachmann, A. D. Borowsky, B. Ruebner, R. D. Cardiff, Q. W. Yang, J. M. Bishop, C. H. Contag, and D. W. Felsher. MYC inactivation uncovers pluripotent differentiation and tumour dormancy in hepatocellular cancer. *Nature*, 431(7012):1112–1117, 2004. [cited at p. 71]
- N. C. Shaner, P. A. Steinbach, and R. Y. Tsien. A guide to choosing fluorescent proteins. *Nature Methods*, 2(12):905–909, 2005. [cited at p. 12]
- I. Solovei, L. Schermelleh, K. Düring, A. Engelhardt, S. Stein, C. Cremer, and T. Cremer. Differences in centromere positioning of cycling and postmitotic human cell types. *Chromosoma*, 112(8):410–423, 2004. [cited at p. 86]
- S. Stadler, V. Schnapp, R. Mayer, S. Stein, C. Cremer, C. Bonifer, T. Cremer, and S. Dietzel. The architecture of chicken chromosome territories changes during differentiation. *Bmc Cell Biology*, 5, 2004. [cited at p. 86]
- J. W. Strutt. Investigations in optics, with special reference to the spectroscope. *Philosophical Magazine*, 8:261–274, 403–411, 477–486, 1879. [cited at p. 14]
- J. W. Strutt. Investigations in optics, with special reference to the spectroscope. *Philosophical Magazine*, 9:40–55 (continued from Vol. 8, p. 486), 1880. [cited at p. 14]

-
- A. Taddei and S. M. Gasser. Repairing subtelomeric DSBs at the nuclear periphery. *Trends in Cell Biology*, 16(5):225–228, 2006. [cited at p. 6]
- H. Tanabe, S. Müller, M. Neusser, J. von Hase, E. Calcagno, M. Cremer, I. Solovei, C. Cremer, and T. Cremer. Evolutionary conservation of chromosome territory arrangements in cell nuclei from higher primates. *Proceedings of the National Academy of Sciences of the United States of America*, 99(7):4424–4429, 2002. [cited at p. 5]
- W. H. Tham and V. A. Zakian. Telomeric tethers. *Nature*, 403(6765):34–35, 2000. [cited at p. 6]
- W. H. Tham and V. A. Zakian. Transcriptional silencing at saccharomyces telomeres: implications for other organisms. *Oncogene*, 21(4):512–521, 2002. [cited at p. 6]
- P. Therizols, C. Fairhead, G. G. Cabal, A. Genovesio, J. C. Olivo-Marin, B. Dujon, and E. Fabre. Telomere tethering at the nuclear periphery is essential for efficient dna double strand break repair in subtelomeric region. *Journal of Cell Biology*, 172(6):951–951, 2006. [cited at p. 6, 87]
- D. Thomann, D. R. Rines, P. K. Sorger, and G. Danuser. Automatic fluorescent tag detection in 3D with super-resolution: application to the analysis of chromosome movement. *Journal of Microscopy*, 208:49–64, 2002. [cited at p. 5, 87]
- D. Thomann, J. Dorn, P. K. Sorger, and G. Danuser. Automatic fluorescent tag localization II: improvement in super-resolution by relative tracking. *Journal of Microscopy-Oxford*, 211:230–248, 2003. [cited at p. 87]
- A. N. Tikhonov and V. Y. Arsenin. *Solutions of Ill-posed problems*. John Wiley and Sons, New York, 1977. [cited at p. 35]
- O. Vafa, M. Wade, S. Kern, M. Beeche, T. K. Pandita, G. M. Hampton, and G. M. Wahl. c-Myc can induce DNA damage, increase reactive oxygen species, and mitigate p53 function: A mechanism for oncogene-induced genetic instability. *Molecular Cell*, 9(5):1031–1044, 2002. [cited at p. 71]
- B. J. Vermolen, Y. Garini, and I. T. Young. 3D restoration with multiple images acquired by a modified conventional microscope. *Microscopy Research and Technique*, 64(2):113–125, 2004. [cited at p. 30]
- B. J. Vermolen, Y. Garini, S. Mai, V. Mougey, T. Fest, T. C.-Y. Chuang, A. Y.-C. Chuang, L. Wark, and I. T. Young. Characterizing the three-dimensional organization of telomeres. *Cytometry Part A*, 67A(2):144–150, 2005a. [cited at p. 53, 57, 59, 87, 92]
- B. J. Vermolen, I. T. Young, A. Chuang, L. Wark, T. Chuang, S. Mai, and Y. Garini. Three-dimensional analysis tool for segmenting and measuring the structure of telomeres in mammalian nuclei. In D. V. Nicolau, J. Enderlein, R. C. Leif, D. L. Farkas, and R. Raghavachari, editors, *Imaging, Manipulation, and Analysis of*

- Biomolecules and Cells: Fundamentals and Applications III (Proc. SPIE Photonics West: Biomedical Optics (BiOS) San Jose, California, USA, Jan.22-27)*, volume 5699, pages 111–120. SPIE, 2005b. [cited at p. 53]
- B. J. Vermolen, Y. Garini, I. T. Young, R. W. Dirks, and V. Raz. Segmentation and analysis of the three-dimensional redistribution of nuclear components in human mesenchymal stem cells. *Cytometry Part A*, 73A(9):816–824, 2008. [cited at p. 53, 86]
- P. J. Verwee and T. M. Jovin. Efficient superresolution restoration algorithms using maximum *a posteriori* estimations with application to fluorescence microscopy. *Journal of the Optical Society of America A*, 14(8):1696–1706, 1997. [cited at p. 33, 34, 49]
- P. J. Verwee, Q. S. Hanley, P. W. Verbeek, L. J. Van Vliet, and T. M. Jovin. Theory of confocal fluorescence imaging in the programmable array microscope (PAM). *Journal of Microscopy*, 189:192–198, 1998. [cited at p. 30, 32, 35]
- P. J. Verwee, M. J. Gemkow, and T. M. Jovin. A comparison of image restoration approaches applied to three-dimensional confocal and wide-field fluorescence microscopy. *Journal of Microscopy*, 193:50–61, 1999. [cited at p. 54]
- B. J. Verwer, L. J. v. Vliet, and P. W. Verbeek. Binary and grey-value skeletons: metrics and algorithms. *International Journal of Pattern Recognition and Artificial Intelligence*, 7(5):1287–1308, 1993. [cited at p. 73]
- L. J. v. Vliet and P. W. Verbeek. Better geometric measurements based on photometric information. In *Instrumentation and Measurement Technology Conference, 1994. IMTC/94. Conference Proceedings. 10th Anniversary. Advanced Technologies in I & M., 1994 IEEE*, pages 1357–1360, 1994. Hamamatsu, Japan, May 10-12. [cited at p. 36]
- H. T. M. v. d. Voort and G. J. Brakenhoff. 3-D image-formation in high-aperture fluorescence confocal microscopy - a numerical-analysis. *Journal of Microscopy*, 158:43–54, 1990. [cited at p. 39]
- C. Vourc'h, D. Taruscio, A. L. Boyle, and D. C. Ward. Cell cycle-dependent distribution of telomeres, centromeres, and chromosome-specific subsatellite domains in the interphase nucleus of mouse lymphocytes. *Experimental Cell Research*, 205(1):142–151, 1993. [cited at p. 84]
- M. E. Wall, A. Rechtsteiner, and L. M. Rocha. Singular value decomposition and principal component analysis. In D. Berrar, W. Dubitzky, and M. Granzow, editors, *A Practical Approach to Microarray Data Analysis*, pages 91–109. Kluwer, Norwell, 2003. [cited at p. 64]
- J. Walter, L. Schermelleh, M. Cremer, S. Tashiro, and T. Cremer. Chromosome order in HeLa cells changes during mitosis and early G1, but is stably maintained during subsequent interphase stages. *Journal of Cell Biology*, 160(5):685–697, 2003. [cited at p. 84]

-
- C. Weierich, A. Brero, S. Stein, J. von Hase, C. Cremer, T. Cremer, and I. Solovei. Three-dimensional arrangements of centromeres and telomeres in nuclei of human and murine lymphocytes. *Chromosome Research*, 11(5):485–502, 2003. [cited at p. 95]
- A. E. Wiblin, W. Cui, A. J. Clark, and W. A. Bickmore. Distinctive nuclear organisation of centromeres and regions involved in pluripotency in human embryonic stem cells. *Journal of Cell Science*, 118(17):3861–3868, 2005. [cited at p. 86]
- F. Wiener, A. Coleman, B. A. Mock, and M. Potter. Nonrandom chromosomal change (trisomy-11) in murine plasmacytomas induced by an ABL-MYC retrovirus. *Cancer Research*, 55(5):1181–1188, 1995. [cited at p. 80]
- F. Wiener, T. I. Kuschak, S. Ohno, and S. Mai. Dereglated expression of c-Myc in a translocation-negative plasmacytoma on extrachromosomal elements that carry *IgH* and *myc* genes. *Proceedings of the National Academy of Sciences of the United States of America*, 96(24):13967–13972, 1999. [cited at p. 80]
- F. Wilcoxon. Individual comparisons by ranking methods. *Biometrics Bulletin*, 1(6):80–83, 1945. [cited at p. 91]
- T. Wilson and J. Tan. Three dimensional image reconstruction in conventional and confocal microscopy. *BioImaging*, 1(3):176–184, 1993. [cited at p. 15]
- I. T. Young, P. W. Verbeek, and B. H. Mayall. Characterization of chromatin distribution in cell-nuclei. *Cytometry*, 7(5):467–474, 1986. [cited at p. 5]
- I. T. Young, J. J. Gerbrands, and L. J. van Vliet. Fundamentals of image processing. In V. K. Madisetti and D. B. Williams, editors, *The digital signal processing handbook*, pages 51.1–51.81. CRC Press in cooperation with IEEE Press, Boca Raton, Florida, 1998. [cited at p. 37, 55, 82]
- B. Zhang, J. Zerubia, and J.-C. Olivo-Marin. Gaussian approximations of fluorescence microscope point-spread function models. *Applied Optics*, 46(10):1819–1829, 2007. [cited at p. 7, 49, 50, 51, 57]
- D. Zink and T. Cremer. Cell nucleus: Chromosome dynamics in nuclei of living cells. *Current Biology*, 8(9):R321–R324, 1998. [cited at p. 84]

List of publications

Journal publications

- [1] T. C. Y. Chuang, S. Moshir, Y. Garini, A. Y. C. Chuang, I. T. Young, **B. Vermolen**, R. van den Doel, V. Mougey, M. Perrin, M. Braun, P. D. Kerr, T. Fest, P. Boukamp, and S. Mai. The three-dimensional organization of telomeres in the nucleus of mammalian cells. *BMC Biology*, 2(1):12, 2004.
- [2] **B. J. Vermolen**, Y. Garini, and I. T. Young. 3D restoration with multiple images acquired by a modified conventional microscope. *Microscopy Research and Technique*, 64(2):113–125, 2004.
- [3] Y. Garini, **B. J. Vermolen**, and I. T. Young. From micro to nano: recent advances in high-resolution microscopy. *Current Opinion in Biotechnology*, 16(1):3–12, 2005.
- [4] S. F. Louis[†], **B. J. Vermolen**[†], Y. Garini, I. T. Young, A. Guffei, Z. Lichtensztejn, F. Kuttler, T. C. Y. Chuang, S. Moshir, V. Mougey, A. Y. C. Chuang, P. D. Kerr, T. Fest, P. Boukamp, and S. Mai. c-Myc induces chromosomal rearrangements through telomere and chromosome remodeling in the interphase nucleus. *Proceedings of the National Academy of Sciences of the United States of America*, 102(27):9613–9618, 2005. [†]: equal contribution.
- [5] **B. J. Vermolen**, Y. Garini, S. Mai, V. Mougey, T. Fest, T. C.-Y. Chuang, A. Y.-C. Chuang, L. Wark, and I. T. Young. Characterizing the three-dimensional organization of telomeres. *Cytometry Part A*, 67A(2):144–150, 2005.
- [6] V. Raz, F. Carlotti, **B. J. Vermolen**, E. van der Poel, W. C. R. Sloos, S. Knaän-Shanzer, A. A. F. de Vries, R. C. Hoeben, I. T. Young, H. J. Tanke, Y. Garini, and R. W. Dirks. Changes in lamina structure are

- followed by spatial reorganization of heterochromatic regions in caspase-8-activated human mesenchymal stem cells. *Journal of Cell Science*, 119 (20):4247–4256, 2006.
- [7] A. Caporali, L. Wark, **B. J. Vermolen**, Y. Garini, and S. Mai. Telomeric aggregates and end-to-end chromosomal fusions require myc box II. *Oncogene*, 26(10):1398–1406, 2007.
- [8] Rahul Sarkar, Amanda Guffei, **B. J. Vermolen**, Yuval Garini, and Sabine Mai. Alterations of centromere positions in nuclei of immortalized and malignant mouse lymphocytes. *Cytometry Part A*, 71A(6):386–392, 2007.
- [9] **B. J. Vermolen**, Y. Garini, I. T. Young, R. W. Dirks, and V. Raz. Segmentation and analysis of the three-dimensional redistribution of nuclear components in human mesenchymal stem cells. *Cytometry Part A*, 73A (9):816–824, 2008.
- [10] V. Raz, **B. J. Vermolen**, Y. Garini, J. J. M. Onderwater, M. A. Mommaas-Kienhuis, A. J. Koster, I. T. Young, H. Tanke, and R. W. Dirks. The nuclear lamina promotes telomere aggregation and centromere peripheral localization during senescence of human mesenchymal stem cells. *Journal of Cell Science*, 121:4018–4028, 2008.

Conference proceedings

- [1] **B. J. Vermolen**, I. T. Young, A. Chuang, L. Wark, T. Chuang, S. Mai, and Y. Garini. Three-dimensional analysis tool for segmenting and measuring the structure of telomeres in mammalian nuclei. In Dan V. Nicolau, Joerg Enderlein, Robert C. Leif, Daniel L. Farkas, and Ramesh Raghavachari, editors, *Imaging, Manipulation, and Analysis of Biomolecules and Cells: Fundamentals and Applications III*, volume 5699, pages 111–120. SPIE, 2005.
- [2] I. T. Young, **B. Vermolen**, G. Linqui Lung, S. Hendrichs, M. el Morabit, J. Spoelstra, E. Wilhelm, and M. Zaal. Absolute fluorescence calibration. In Daniel L. Farkas and Dan V. Nicolau Robert C. Leif, editors, *Imaging, Manipulation, and Analysis of Biomolecules and Cells: Fundamentals and Applications IV*, volume 6088. SPIE, 2006.
- [3] H. R. C. Dietrich, **B. J. Vermolen**, B. Rieger, I. T. Young, and Y. Garini. A new optical method for characterizing single molecule interactions based on dark field microscopy. In Jorg Enderlein and Zygmunt K. Gryczynski, editors, *Ultrasensitive and Single-Molecule Detection Technologies II*, volume 6444. SPIE, 2007.

- [4] I. T. Young, M. el Morabit, G. Liqui Lung, and **B. J. Vermolen**. Photonic calibration for fluorescence microscopy. In Daniel L. Farkas and Dan V. Nicolau Robert C. Leif, editors, *Imaging, Manipulation, and Analysis of Biomolecules, Cells, and Tissues VI*, volume 6859. SPIE, 2008.

Patents

- [1] S. Mai, Y. Garini, R. Sarkar, and **B. J. Vermolen**. Methods of detecting and monitoring cancer using 3D analysis of centromeres. WIPO Patent WO2008040116, 2008.
- [2] S. Mai, Y. Garini, W. Foulkes, S. Panigrahi, **B. Vermolen**, T. Chuang, A. Chuang, and G. Jones. Methods of diagnosis or detection using three-dimensional analysis. WIPO Patent WO2006017942, 2006. European Patent EP1799851, 2007.

Curriculum Vitae

Bart J. Vermolen was born in Rucphen, the Netherlands on June 26th 1977. In 1995 he obtained his grammar school diploma at the Mollerlyceum in Bergen op Zoom. The same year he started his education in Applied Physics at the Delft University of Technology. In 2003 he obtained the title of ‘ingenieur’ (MSc) with his thesis on ‘3D restoration of confocal images acquired by a modified conventional microscope’, supervised by Prof. dr. Ian T. Young in the Quantitative Imaging Group.

Continuing research in image processing and analysis on images of the cell nucleus he started pursuing a PhD on the topic of describing nuclear architecture in a quantitative manner in the same group. He was supervised by Prof. dr. Ian T. Young and Prof. dr. Yuval Garini and worked in close collaboration with Prof. dr. Sabine Mai (University of Manitoba, Canada) and dr. Vered Raz (Leiden University Medical Center). This work was financially supported by the Cyttron consortium.

During this time he has been involved in teaching courses as a lecturer and teaching assistant at the Delft University of Technology and has supervised 20 undergraduate students with their end-year projects of which seven with their BSc thesis. Since 2005 he has also lectured in courses on microscopy and image processing at the ‘CIHR Strategic Training Program: Quantitative Fluorescence Analysis of Cells, Tissues and Chromosomes’ in Winnipeg, Canada and at the ‘Pre-Congress Course on Imaging’ of the bi-annual International Society of Analytical Cytometry Congress.

Bart has continued his career as a postdoctoral fellow at the University of Twente in the Biophysical Engineering Group in November 2007, supervised by Prof. dr. Vinod Subramaniam and dr. ir. Hans S. Kanger. His main interest lies in the development of high resolution fluorescence imaging techniques to study protein-membrane interactions.

Acknowledgments

Indy was right. When you're a scientist, nothing should shock you. A shock will close your mind, make you lose your curiosity and the will of wanting to solve the puzzle. Although Indy was kind of a loner, he was never alone. Neither was I.

Ted, like any other professor, you had tons of other things to do. It was good to know that your most favorite thing to do is to have a good scientific discussion with one of your students. Then there was Yuval. What should I say? Yuval, you're THE MAN. Your ever-lasting optimism, your readiness to discuss anything, love for teaching, the dinners and trips all over world (even accidentally bumping into each other in a 1.7 million people city, coincidence?) have helped me realize that science can be plain, good old fun. Ted, Yuval, thanks!

Good collaborations are gold. Every time people complement me on the amount of work that I have done during my time as a PhD student, I have to correct them. Most of the 'real work' was done in the wetlabs, preparing slides, acquiring images, etcetera. Sabine and Vered: you, your students and analysts have helped and learned me so much. Thank you giving my thesis biological relevance.

A significant time of your life you spend with your office roommates, so they better be good. And they were. Koen, thank you for listening to my music all day. And thank you for raising all kinds of critical questions about statistics and then, after I tried for hours to figure out what the best method would be saying: "remember that statistics are just meant as an aid". Sanneke, thanks for bringing the vrijdagmiddagborrel back into the group. And for putting up with my music (of course until you installed *the switch*). Heidi, Margreet and Gea, thank you for the nice Microscopy Group meetings. Everything falls apart without good support. Thanks for the coffee (Wim), electronics (Guus), very loud IT (Ronald) and everything else (Mandy). The time spent, more than six years, at Quantitative Imaging (TGFKAPH) has been great because of all of its members, thank you all.

What would a man be without his family and friends. My parents (all of

them), thanks for the love and food and upbringing up till my college years. My friends (you know who you are), thanks for the love and food and upbringing since my college years.

With these words I end my thesis and an important chapter of my life. With all endings come new beginnings, the most exciting one is about to start and I am happy and lucky to start this new life with you, Yvette.

Aglet: plastic cover at the end of cotton, protecting the shoelace from destruction.

Telomere: repetitive sequence at the end of DNA, protecting the chromosome from destruction.